MICROFABRICATED ELECTROMAGNETIC ACTUATORS FOR CONFOCAL MEASUREMENTS AND IMAGING

by

Hadi Mansoor

B.A.Sc., The University of British Columbia, 2008

A THESIS SUBMITTED IN PARTIAL FULFILLMENT OF
THE REQUIREMENTS FOR THE DEGREE OF

DOCTOR OF PHILOSOPHY

in

THE FACULTY OF GRADUATE STUDIES

(Biomedical Engineering)

THE UNIVERSITY OF BRITISH COLUMBIA
(Vancouver)

April 2013

ABSTRACT

Various optical microscopy techniques have been developed for micrometer level imaging of biological tissue samples. Among those techniques, confocal imaging provides superior image contrast and high resolution with a modest system cost. Confocal microscopy allows vertical optical sectioning (imaging a section perpendicular to the surface of tissue) or horizontal optical sectioning (imaging a section parallel to the surface of tissue) and provides high-resolution tissue morphology that is analogous to conventional histopathology images. This has brought up a tremendous potential for guiding surgical biopsies and *in vivo* non-invasive diagnosis of diseases such as cancer. The challenge in moving microscopic imaging modalities into clinical applications is miniaturization into a form of hand-held devices or catheters for endoscopic applications.

In this thesis, micro-fabrication techniques such as Microelectromechanical Systems (MEMS) fabrication process and laser micromachining have been employed to develop magnetic actuators. The actuators are then used to move lenses and optical fibers in order to scan a laser beam across a sample. Lens and fiber actuators are integrated in catheter and hand-held devices for confocal thickness measurement and optical sectioning imaging of biological samples.

Thickness measurement is performed by scanning the focal point of a microlens across the thickness of thin films or layered biological tissues and collecting the intensity signal of the single scattering light reflected back from the samples as a function of lens position. A catheter was developed and thickness measurements of polymer layers and biological tissues

were demonstrated. The device has optical resolution of 32 μm with expanded uncertainty of measurement of 11.86 μm.

Lens and fiber optic actuators have been coupled to form two-dimensional imaging devices. Direct and real-time vertical and horizontal cross-sectional imaging of biological samples has been demonstrated. Vertical imaging is performed by transverse (X-axis) and axial (Z-axis) scanning of a focused laser beam using an optical fiber and a microlens actuator respectively. Horizontal imaging is done by a 2-axis fiber optic scanner. All the developed actuators are driven by electromagnetic forces and require low driving voltages. Confocal imaging of biological samples, with lateral resolution of 1.55 μm, has been demonstrated.

PREFACE

The research presented in this thesis was carried out in the University of British Columbia (UBC) MEMS Laboratory in the Department of Mechanical Engineering under the supervision of Dr. Mu Chiao. A portion of research was also conducted in the Imaging Unit of Integrative Oncology Department in the British Columbia Cancer Agency Research Center (BCCRC), under the supervision of Dr. Haishan Zeng.

Chapter 1 of this thesis is a brief review of various optical microscopy techniques and an introduction to MEMS fabrication technology. In this chapter, different MEMS scanners and actuation mechanisms used in optical scanning are presented.

Chapter 2 is based on the work published in the following journal articles:

- **Mansoor, H**., Zeng, H., and Chiao, M. (2011) "Real-time thickness measurement of biological tissues using a microfabricated magnetically-driven lens actuator" Biomedical Microdevices. 13: 641–649.

- **Mansoor, H**., Zeng, H., and Chiao, M. (2011) "A microfabricated optical scanner for rapid noncontact thickness measurement of transparent films" Sensors and Actuators A: Physical. 167: 91–96.

This work was also presented in the following workshops and conferences:

- **Mansoor, H.**, Zeng, H., and Chiao, M. (2010) "Magnetically driven scanning microlens for out-of-plane in vivo medical imaging" 217th ECS Meeting. Vancouver, Canada.

- **Mansoor, H.**, Zeng, H., and Chiao, M. (2010) "A confocal scanner for biological tissue thickness measurement" ICICS Biomedical Engineering Workshop, Vancouver, Canada.

- **Mansoor, H.**, Zeng, H., and Chiao, M. (2011) "A confocal fiber optic catheter for *in vivo* thickness measurement of biological tissues" IEEE 24th International Conference on MEMS, Cancun, Mexico. 999-1002.

These papers describe confocal thickness measurement of transparent and semi-transparent thin films and biological tissues. The author conducted literature review on existing MEMS scanning systems and lens actuators, and fabricated an electromagnetic lens actuator using electroplating technique. The lens actuator was coupled with an optical fiber and encapsulated in a 30 mm long and 4.75 mm outer diameter tube to form a catheter for endoscopic applications. The author performed experimental design, device characterization, experimental setup preparation, conducting experiments and data analysis. The manuscript was prepared under the supervisions of Dr. Mu Chiao and Dr. Haishan Zeng. Supervisors guided the author through all aspects of the work and provided editorial suggestions on the manuscripts.

Chapter 3 is a version of work published in the following journal:

- **Mansoor, H.**, Zeng, H., Chen, K., Yu, Y., Zhao, J., and Chiao, M. (2011) "Vertical optical sectioning using a magnetically driven confocal microscanner aimed for *in vivo* clinical imaging" Optics Express. 19(25): 25161-25172.

The same paper was also selected for publication in the Virtual Journal for Biomedical Optics, Vol. 7, Issue 2, February 2012. This work was presented in the Hilton Head 2012 Workshop on the science and technology of solid-state sensors, actuators, and microsystems and published in the conference proceedings:

- **Mansoor, H.**, Zeng, H., Chen, K., Yu, Y., Zhao, J., and Chiao, M. (2012) "Histology-equivalent vertical optical sectioning using a 2-axis magnetic confocal microscanner" Solid-State Sensors, Actuators, and Microsystems Workshop, Hilton Head Island, South Carolina, USA, 397- 400.

In this work we show mechanical and optical design and simulations of a 2-axis scanner capable of imaging a vertical cross-section of biological samples. The author conducted literature review, performed mechanical design and analysis, fabricated actuators, carried out optical simulation, assembly and alignment, and finally performed imaging experiments on samples. The manuscript was written under the direction of Dr. Mu Chiao and Dr. Haishan Zeng. Dr. J. Zhao, Mr. K. Chen and Mr. Y. Yu helped with preparation of imaging setup and developing image processing software.

Chapter 4 presents a novel fiber optic scanner that was used for confocal imaging of horizontal cross-sections of biological samples. This work is published in the following journal paper:

- **Mansoor, H.**, Zeng, H., Tai, I. T., Zhao, J., and Chiao, M. (2012) "A handheld electromagnetically actuated fiber optic raster scanner for reflectance confocal imaging of biological tissues" IEEE Transactions on Biomedical Engineering, In Press.

This work was also presented in the 26th IEEE International Conference on MEMS:

- **Mansoor, H.**, Zeng, H., Tai, I. T., Zhao, J., and Chiao, M. (2013) "A miniature fiber-optic raster scanner for 2D optical imaging of biological tissue" , 26th IEEE International Conference on MEMS, Taipei, Taiwan, 137 – 140.

In this chapter we present a novel fiber optic actuator driven by electromagnetic forces and capable of scanning samples in a raster pattern. The author conducted literature review, mechanical design, fabrication, assembly, system integration, optical simulation, optical assembly and allignment, and imaging test on specimens. Dr. Mu Chiao and Dr. Haishan Zeng supervised the work and provided expert guidence and advice. Dr. J. Zhao helped with developing the imaging setup and Dr. I. T. Tai provided biological tissue samples for imaging experiments. An image artifact originating from mechanical motion of electromagnetic actuators was observed, investigated and corrected by methods that are described in Appendix B of this thesis.

Contributions of the work included in this thesis can be summarized as following:

1. Designed and developed a novel actuator for scanning a lens in the out-of-plane direction. The actuator is driven by magnetic field and can provide large scanning range with low driving voltages.

2. Developed fabrication process for the magnetic actuators including:

    - Nickel electroplating on silicon wafers and laser micromachining of ferromagnetic foils.

    - Using positive photoresist as a mold for electroplating process.

3. Demonstrated real-time thickness measurement of samples using a lens actuator and designed and fabricated a catheter for endoscopic applications.

4. Demonstrated confocal imaging of vertical cross-section of biological samples by designing and fabricating a 2-axis electromagnetic scanner using laser micromachining techniques.

5. Designed and developed a novel 2-axis fiber optic actuator capable of scanning samples in a raster pattern. Demonstrated functionality of device by imaging horizontal sections of biological samples.

6. Investigated potential causes of imaging artifacts in electromagnetically driven optical scanners and implemented real-time correction methods.

TABLE OF CONTENTS

LIST OF TABLES

LIST OF FIGURES

LIST OF SYMBOLS, ABBREVIATIONS AND UNITS

#	number
%	percent
μ_0	permeability of free space
μm	micrometer
º	degree
º C	degree Celsius
ζ	damping ratio
λ	wavelength
λ_e	wavelength of excitation light
π	pi (3.1415926)
ω	frequency of actuation
ω_i	frequency of current
ω_n	natural frequency
$\Re$	magnetic reluctance
ϕ	magnetic flux
A	cross sectional area of an electromagnet core
a	length of cantilever beam
a.u.	arbitrary unit
AC	alternating current
Al	aluminum
Au	gold
AVC	angular vertical comb
AWG	American wire gauge

B	magnetic flux density
BOE	buffered oxide etch
c	damping coefficient
CAD	computer-aided design
CM	confocal microscopy
cm	centimeter
Cr	chromium
CVD	chemical vapor deposition
d	displacement of lens between intensity peaks
DAQ	data acquisition
DC	direct current
DRIE	deep reactive ion etching
E	Young's modulus
EFL	effective focal length
$F(z)$	restoring force of one folded beam
FCM	fluorescence-mode confocal microscopy
FFT	fast Fourier transform
FEA	finite element analysis
F_{mag}	magnetic force
F_{mmf}	magnetomotive force
FOV	field of view
F_s	restoring force of the nickel flexure
fs	femtosecond
FWHM	full width at half maximum
g	gram

g_z	gap between the coil and nickel flexure
H	magnetic field strength
H&E	hematoxylin and eosin
Hg	mercury
HMDS	hexamethyldisilazane
Hz	Hertz
i	current in a coil
I	moment of inertia
IC	integrated circuits
IOP	intraocular pressure
IR	infra red
k	mechanical stiffness
kHz	kilo Hertz
KOH	potassium hydroxide
l	liter
l_b	length of folded beam in flexure
LDV	laser doppler vibrometer
l_f	length of optical fiber
m	mass
mA	milliampere
MEMS	microelectromechanical systems
MFD	mode field diameter
mJ	millijoule
mm	millimeter
MOEMS	micro-optoelectromechanical systems

MPM	multi-photon microscopy
mT	millitesla
MTF	modulation transfer functions
mV	millivolt
mW	milliwatt
n	refractive index of a medium
N	number of turns of wire in a coil
n_0	refractive index of air
NA	numerical aperture
ND	neutral density
n_f	refractive index of film
Ni	nickel
NIR	near-infrared
nm	nanometer
OCT	optical coherence tomography
OTF	optical transfer function
PBS	polarizing beamsplitter
PH	diameter of pinhole
PM	polarization maintaining
PMT	photomultiplier tube
PR	photoresist
PZT	piezoelectric
Q	quality factor
R_{axial}	axial resolution
RCM	reflectance-mode confocal microscopy

RIE	reactive ion etching
$R_{lateral}$	lateral resolution
rms	root mean square
RPM	revolution per minute
S	sagittal
s	second
SD	standard deviation
SHG	second harmonic generation
Si	silicon
SiO_2	silicon dioxide
SMF	single mode fiber
SNR	signal-to-noise ratio
T	tangential
t_f	thickness of film
TPEF	two-photon excitation fluorescence
UV	ultraviolet
W	Watt
$W(z)$	profile of focused laser beam
w_0	laser beam waist radius
W_{mag}	net work in an electromagnetic system
wt	weight
z	relative axial position
z_R	Rayleigh range

ACKNOWLEDGEMENTS

This dissertation would not have been possible without help, support and guidance of my research advisor Dr. Mu Chiao. I thank him for giving me the honor of working in his group, and for his patience, enthusiasm, attention to details and encouragement. Besides my advisor, I am indebted to my co-supervisor, Dr. Haishan Zeng for his invaluable support, great advice and immense knowledge. I could not have imagined having better advisors for my study.

I also would like to thank my dissertation committee members, Dr. Shuo Tang, Dr. Ryozo Nagamune, Dr. Kenichi Takahata and Dr. Anna Celler for their time and valuable comments. I thank Dr. Boris Stoeber, Dr. Xiaodong Lu and Dr. Srikantha Phani from department of mechanical engineering, Dr. Keng Chou from department of chemistry at UBC and Dr. Jianhua Zhao from Imaging Unit at BC Cancer Agency for their guidance and great discussions.

I offer my gratitude to my fellow lab mates in MEMS lab and friends at UBC specially Reza Rashidi, Nazly Pirmoradi, Farzad Khademolhosseini, Jacob Yeh, Kevin Ou, Kequin Chen, Payam Zachkani and my brother Iman Mansoor for sharing ideas and helpful discussions.

I can not find words to express my gratitude to my parents for sacrifices they made through immigration that made my study possible and to my brothers and sister for their support and encouragements. Finally, I am indebted to my beautiful wife, Shima, for her encouragement, patience, dedication and unwavering love in the past ten years. She stood by me and supported me in every way, which made this dissertation possible.

DEDICATION

To my parents,

for their continued love;

&

To my lovely wife, Shima,

for her unconditional support and

being there through the hard times.

CHAPTER 1

INTRODUCTION

Optical microscopy provides detailed morphological and microstructural information for visualization and quantitative measurement of specimens including biological samples. This information can be useful for early detection of cancer lesions and delineating their margins before biopsy and surgery. Moving optical microscopy modalities into clinical applications is challenging because miniaturized laser beam scanning devices have to be designed and integrated in hand-held probes or endoscopic catheters for real-time imaging of samples. Microelectromechanical Systems (MEMS) technology is used to fabricate various micro-scanning systems for optical imaging modalities. MEMS-enabled optical medical devices can be small and have functionalities unattainable with conventional medical systems. In this chapter we review common optical microscopy techniques used in biomedical applications followed by an introduction on MEMS fabrication technologies. Then we review various actuation mechanisms and available MEMS actuators developed for optical imaging applications.

1.1 Optical Microscopy

Various optical microscopy techniques have been developed for non-destructive imaging of biological tissues. These techniques include Optical Coherence Tomography (OCT) [1, 2], Multi-photon Microscopy (MPM) [3, 4], Reflectance-mode Confocal Microscopy (RCM) [5, 6], and Fluorescence-mode Confocal Microscopy (FCM) [7, 8]. Microscopic images obtained by these techniques provide high resolution morphological information approaching that offered by histology images of fixed tissue sections. Figure 1.1 compares imaging resolution and penetration depths of three optical imaging modalities.

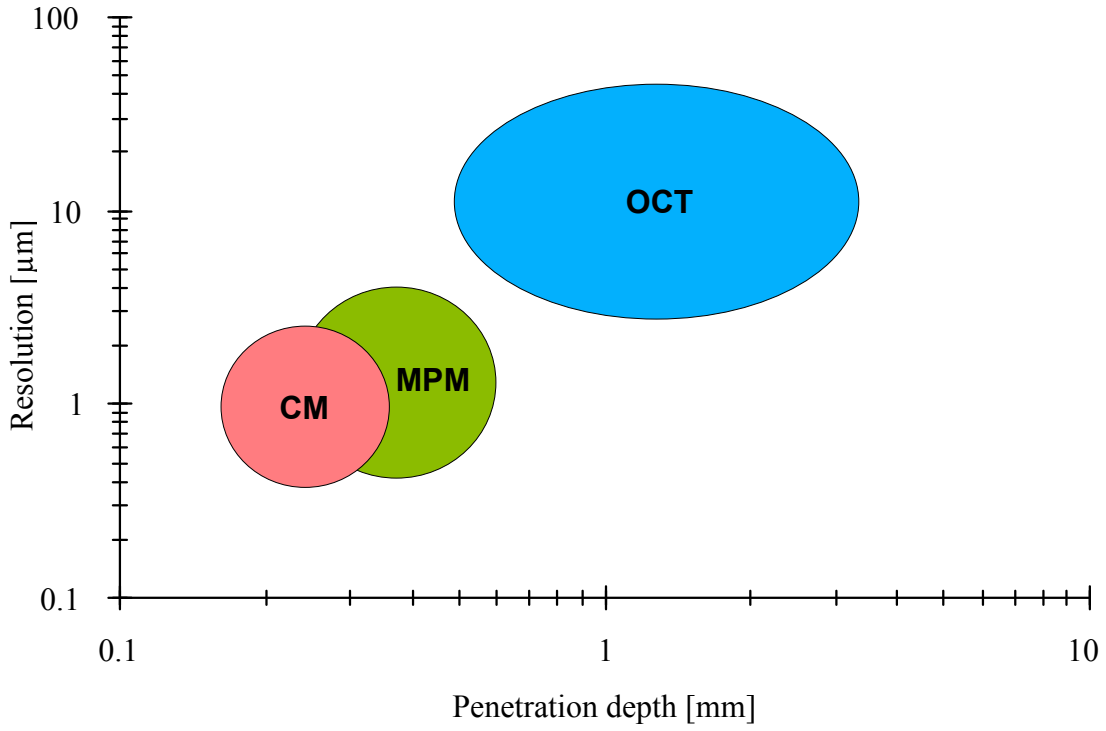

Figure 1.1 Comparison of resolution and imaging depth of various optical microscopy techniques. OCT: optical coherence tomography; MPM: multi-photon microscopy; CM: confocal microscopy.

1.1.1 Optical Coherence Tomography (OCT)

OCT provides high resolution cross-sectional imaging of microstructures in various materials including biological tissue. It relies on the interference of coherent light waves. Axial measurement of backscattered or back-reflected light is performed by low coherence interferometry techniques. Lateral scanning of light beam is usually done using mirror/micromirror or optical fiber scanners. Among optical imaging techniques, OCT has relatively large imaging depth (~2 mm) and field of view (FOV), but generally, lower spatial resolution (about 10-15 μm) and not as good image contrast due to the speckle effect. OCT performs vertical sectional imaging by default and its miniaturization is the easiest to implement because only one dimension of mechanical scanning is required (transverse direction).

1.1.2 Multi-photon Microscopy (MPM)

MPM often employs two-photon excitation fluorescence (TPEF) and second harmonic generation (SHG) signals for image formation. In these methods, two or more low energy photons are absorbed by the sample to excite an electron from the ground energy level to a higher energy level. When the electron returns to the ground level, the extra energy is released as a photon which has higher energy and shorter associated wavelength than the exciting ones. In this method a beam of light is focused on the sample by a lens. Cross-sectional imaging is performed by scanning the light beam in a horizontal plane (parallel to the surface of tissue), using two-dimensional mirrors/micromirrors or optical fiber scanners. MPM has penetration depth of up to 1 mm, but can provide higher image resolution (~1 μm) compared to that of OCT. One drawback of MPM systems is requirements for demanding

optics and high cost mode-locked laser sources capable of providing high peak power and short femtosecond (fs) pulses.

1.1.3 Confocal Microscopy (CM)

CM provides superior image contrast and high resolution tissue and cellular morphology images that are close to that of histology. The concept of CM is based on the rejection of out-of-focus light using a pinhole that enables optical sectioning of samples and enhances imaging resolution and contrast. Confocal microscopy is performed in RCM or FCM. FCM images offer high signal-to-noise ratio (SNR); however, in many cases, RCM is more favorable over FCM since it uses native tissue signals and does not require high quantum yield exogenous fluorescence contrast agents which bring additional drug administration procedures and complications. In addition, in RCM imaging (near-infrared (NIR) laser illumination) deeper light penetration is achievable compared to FCM (visible wavelength laser excitation), that would enable imaging of deeper layers within the tissue. The resolution of a confocal system is close to that of MPM. The major drawback in confocal microscopy is its limited imaging depth (~ 0.2 mm); however, this imaging depth is good enough for the detection of many diseases such as early epithelial cancers. Figure 1.2 shows a typical configuration of a confocal microscope.

It consists of a light source, a beam splitter, an objective lens, a detector and two pinholes. The entrance pinhole is located on the optical axis and limits the field of laser illumination. An image of this pinhole is projected on the sample by the objective lens. The exit pinhole is placed in the conjugate focal plane of the objective lens and rejects the out-of-focus light in the image plane. The size of pinhole governs the resolution of the system. Smaller pinhole

improves the resolution but lowers the amount of light received by the detector which results in higher requirements on detection electronics. This configuration helps to reject light scattered from parts other than the focal point of the lens. This will greatly help to increase resolution, improve SNR, and reduce image blur due to light scattering.

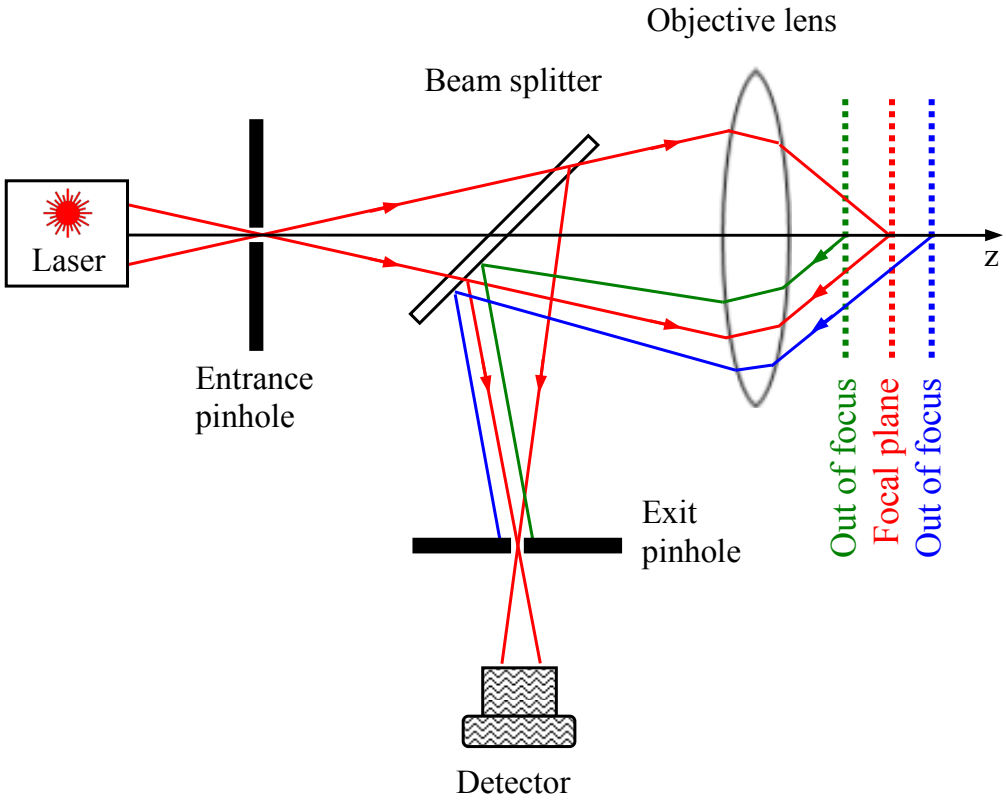

Figure 1.2 Basic principle of confocal microscopy.

1.2 Microelectromechanical Systems (MEMS)

MEMS is a technology that incorporates miniature mechanical components and integrated circuits (IC) to build sensors, actuators and microsystems [9]. Mass production and cost reduction are possible with MEMS technology compared to traditional sensor/actuator manufacturing technologies. Many MEMS sensors and actuators in micrometer scale have

found applications in automotive industry [10], biotechnology [11] and wireless communications [12].

MOEMS or Micro-Optoelectromechanical Systems are MEMS devices that incorporate optical components such as mirrors [13] and lenses [14]. Applications of MOEMS devices include telecommunication [15], medical imaging [16], and consumer products [17]. The smallest feature size of a MEMS and MOEMS device usually ranges from a few microns up to a few millimeters.

Conventionally, fabrication of MEMS devices is performed using silicon (Si) thin-film technologies similar to IC technology that builds semiconductor circuitry. Batch fabrication of MEMS devices is realized by fabricating several or hundreds of micro devices with similar or different designs on a common Si wafer in a single fabrication process. This is the same way that IC devices are built and will greatly help in reducing production cost. Because of the small size, MEMS devices cannot be fabricated using conventional machining equipment such as cutting, drilling or forming. Instead, thin-film deposition, photolithography and chemical etching are the techniques to fabricate MEMS devices.

Deposition is a process of placing thin layers of metals, dielectric materials, semiconductors or other substances such as photo-sensitive materials (photoresist (PR)) on a substrate. This can be done by physical methods using evaporator, sputtering machine, substrate spinner, or by chemical methods using chemical vapor deposition (CVD) machines. After deposition, thin films are patterned by a process called photolithography. It is a process that is used to transfer the MEMS structure design from a photo mask to a PR. To make the photo mask, desired pattern is first generated using computer-aided design (CAD) software. The design is

then used to pattern a chromium film deposited on a glass plate by a laser or an electron beam writing system. Next, a layer of PR is spin-coated on the substrate and baked. The thickness of this layer can be controlled by spinning speed and PR viscosity. The photo mask is then placed on the PR and the PR is selectively exposed to ultraviolet (UV) light. The UV exposure changes the chemical properties of the PR. The substrate is then moved into a next position and UV exposure is carried out again. The process is repeated until all the substrate area is exposed. An illustration of a photolithography process is shown in Figure 1.3. After the UV exposure process, the substrate is placed in a developer solution that etches away either the exposed or unexposed regions of the PR, depending on the type of PR used in the process.

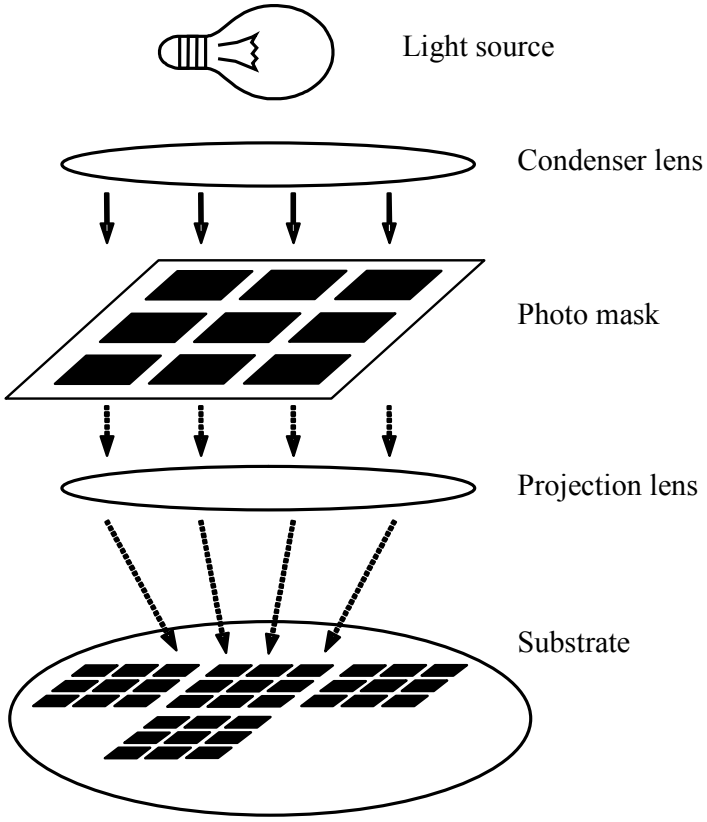

Figure 1.3 Illustration of a photolithography process.

Etching is a process that is frequently used in MEMS fabrication to selectively remove materials that are not protected by PR or any other physical layers above. The materials that can be etched are either the deposited thin films or the substrate itself. Wet etching is performed in a chemical bath. Most wet chemical etchings result in an isotropic etching profile. Wet etching requires simple equipment setup, but precise control on the etching rate is difficult. Dry etching is performed in vacuum chambers using chemical in gaseous form. Available dry etching methods include Reactive Ion Etching (RIE), Deep Reactive Ion Etching (DRIE), and Plasma Etching. Figure 1.4 illustrates basic steps in MEMS fabrication. Further reading of MEMS fabrication processes can be found in textbooks [18].

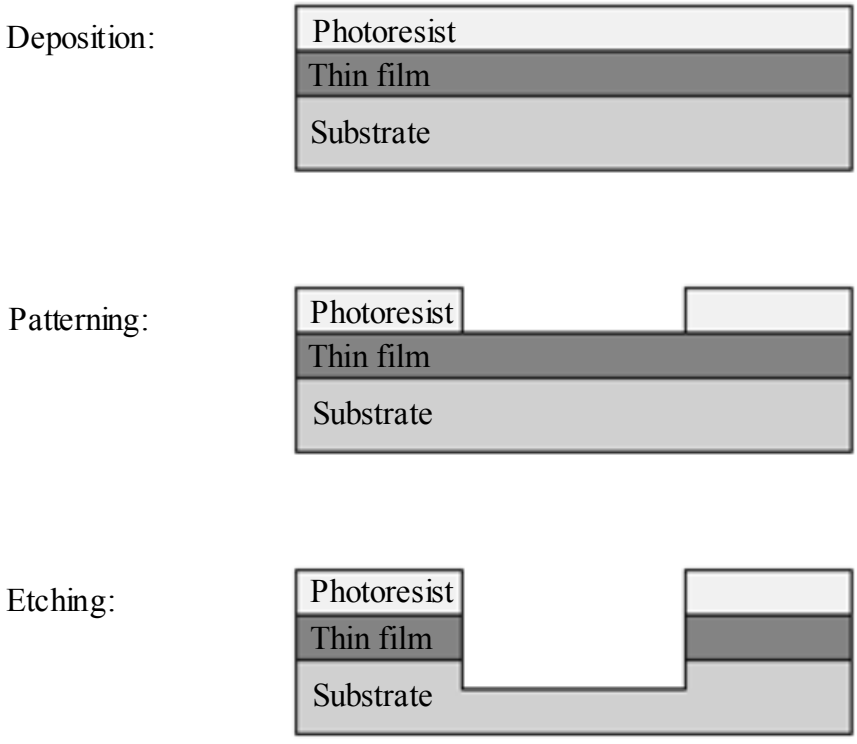

Figure 1.4 Basic MEMS fabrication process flow.

1.2.1 Surface Micromachining

The previous section described methods of depositing layers, photo-patterning and selective etching. However, a unique combination of those techniques is required to realize micro mechanical structures on a substrate. The substrate acts as a mechanical support for the microstructures and can be made of silicon, glass or plastic. The micro mechanical structures are the thin films that are deposited and patterned on the surface of the substrate, hence the terminology "surface micromachining". To fabricate free moving mechanical structures, "sacrificial layers" are needed. Figure 1.5 illustrates an example of the surface micromachining steps required to fabricate a cantilever beam on a Si substrate.

As shown in Figure 1.5 (b), a layer of "sacrificial" film is first deposited and the first photolithography step and etching are performed to form a hole in the film. The second film is deposited that covers the hole and bounds with the substrate to form an "anchor". The second photolithography and etching steps are carried to form a shape of a cantilever beam in the second layer film (Figure 1.5 (c)). Lastly, the sacrificial film is chemically etched, while leaving the cantilever beam intact through etching selectivity (Figure 1.5 (d)). The combinations of material selection, processing chemicals and temperature in surface micromachining require extensive development. Further reading can be found in "Surface micromachining for microelectromechanical systems" [9].

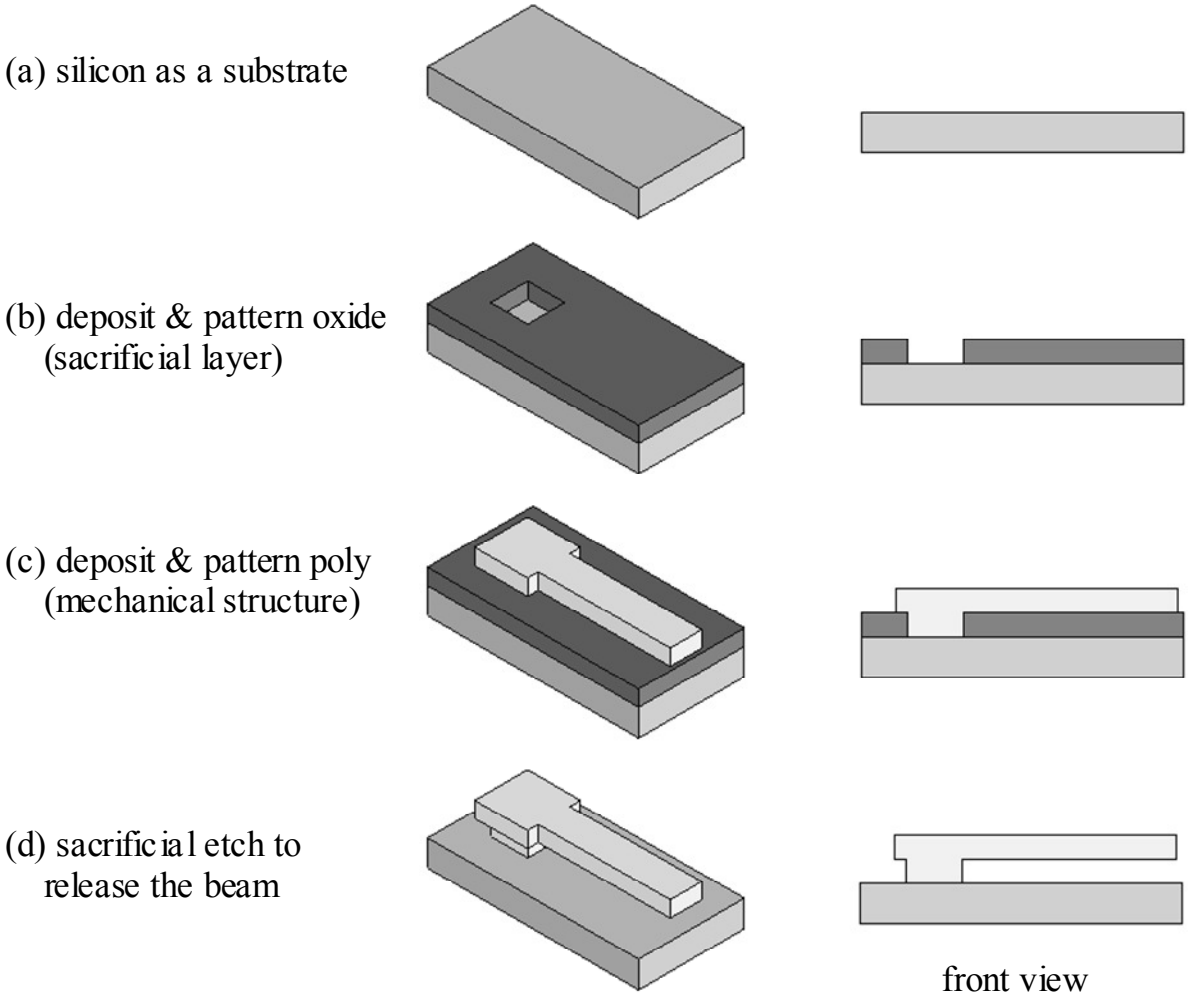

Figure 1.5 Fabrication of cantilever beam on a Si substrate.

1.2.2 Bulk Micromachining

In contrast to surface micromachining, "bulk micromachining" directly defines the structures by selective etching of single crystalline Si substrates. Depending on the chemicals and techniques used, etching can be wet or dry and can have anisotropic or isotropic profiles. To realize the selective etching, usually a layer of silicon dioxide (SiO_2) is thermally deposited and patterned on a Si substrate. Then the substrate is exposed to chemicals to etch away the parts of the Si that are not protected by SiO_2. Figure 1.6 shows an example etching of SiO_2 and Si substrate to form a cantilever beam.

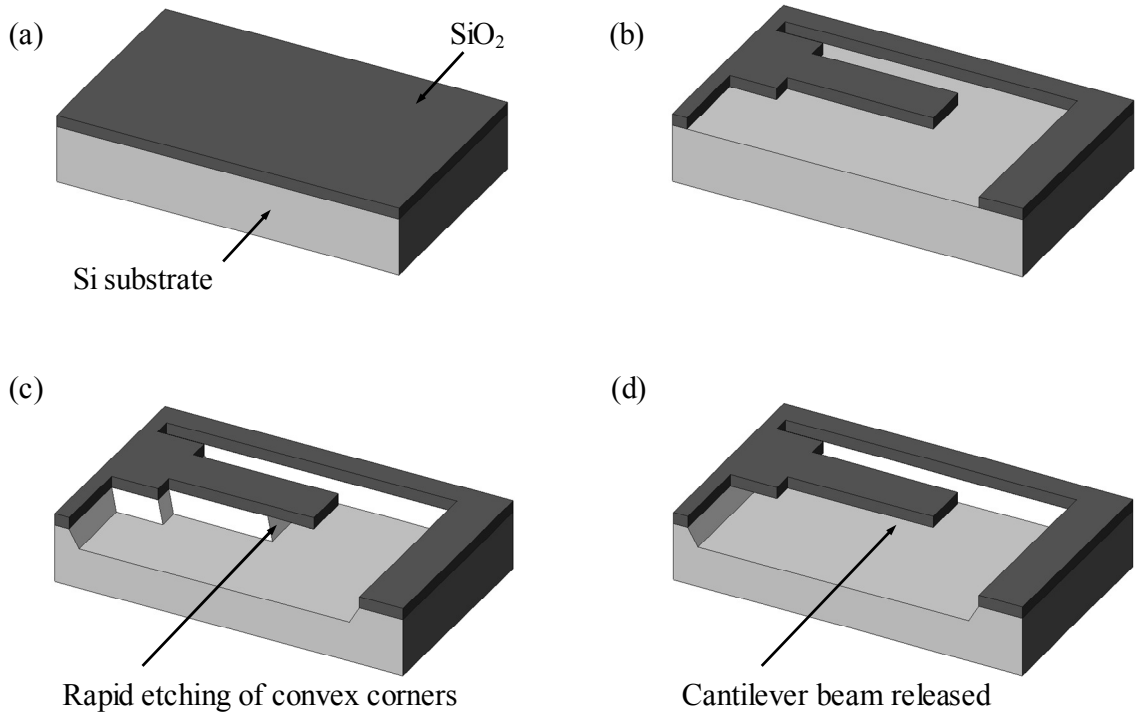

Figure 1.6 Si wafer etching steps showing (a) SiO_2 deposition and (b) patterning followed by (c) silicon substrate etching until (d) cantilever beam released.

1.2.3 Laser Micromachining

Developed more recent than both surface and bulk micromachining technologies, laser micromachining has been used to fabricate microdevices [19, 20]. This technique is more flexible in material selection, processing chemicals and temperatures than other micromachining technologies. Furthermore, laser micromachining may be arguably more environmentally friendly since no chemicals are required during the process. Laser with proper optics can be used to cut or drill through thin films. Wavelength, energy and pulse width of laser can be properly selected to provide selective machining of a variety of materials, including metals [21], polymers [22] and ceramics [23, 24]. In this way a layer of a material can be machined without damaging the layers underneath. In general, "laser writing" is required to fabricate devices using laser. This can make the process much slower than batch fabrication type micromachining techniques, such as surface micromachining. This is because the laser removes materials only at a small spot that it is focused at each time. For cutting a line or a shape, usually a CAD file is imported to the laser machining equipment. A motorized stage follows the CAD drawing to achieve the desired shape of cut. Figure 1.7 is photograph of a commercial laser machining system (QuikLaze 50ST2, New Wave Research, USA). Depending on the materials to be cut, the laser wavelength can be selected to be IR, green or UV. Figure 1.8 shows a sample cut on a thin film gold using green laser.

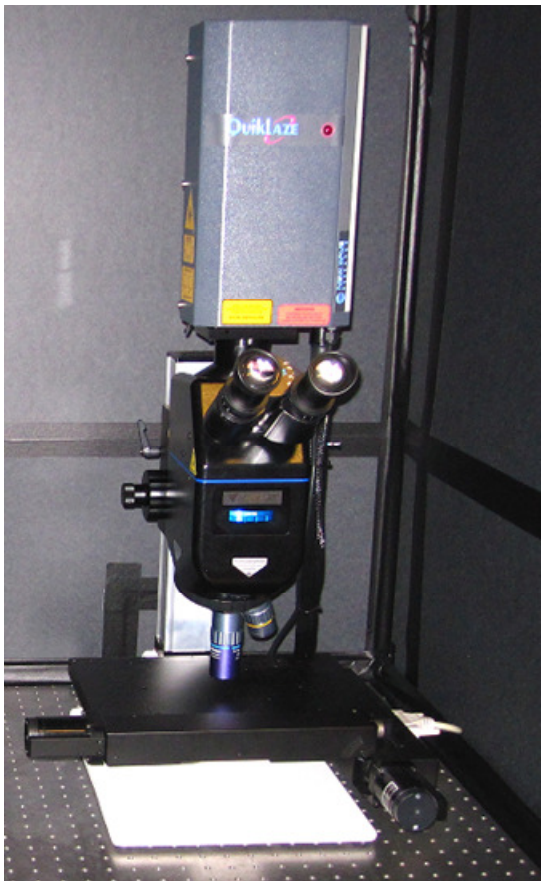

Figure 1.7 Laser micromachining setup - QuikLaze 50ST2.

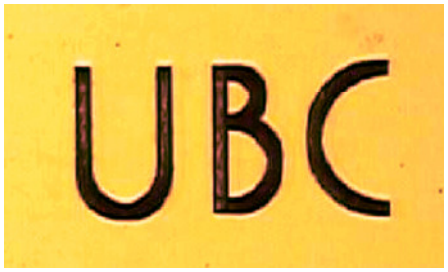

Figure 1.8 Green laser used to cut letters UBC in a 200 nm gold evaporated on a Si substrate. The width of cut is 40 µm.

1.3 MEMS for Optical Microscopy

There are three types of laser beam scanners for optical microscopy; mirror scanners, lens scanners and optical fiber scanners. The actuation mechanism of these scanners can be presented in four main categories. This includes electrostatic, electromagnetic, electrothermal and piezoelectric actuators.

1.3.1 Electrostatic Actuators

Electrostatic actuators are based on the force applied to charge particles by electric field. One common type of this actuation method is based on two parallel electrodes. In this method one electrode is fixed and the second one is capable of actuation in electric field. Petersen in 1980 [25], developed an electrostatic scanner by aligning and stacking two micromachined substrates. The upper substrate is made of single-crystalline Si that is machined to form a center piece that acts as a mirror and two torsional bars to suspend the mirror. The center piece is coated with a layer of aluminum to enhance the reflection. The actual mirror surface area is around 2×2 mm^2. The bottom substrate that can be Si or glass is etched to form a gap between the mirror and two electrodes that are placed at the bottom of the etched area. The deflection of the mirror is achieved by applying 300-400 volts between the electrodes and the mirror. This scanner has a resonance frequency of 15 kHz and is capable of scanning about $\pm1°$.

Another type of electrostatic actuators is based on comb-shape electrodes. Conant et al. demonstrated a scanning micromirror [26] that is actuated by staggered torsional comb actuators. In their design, the lower comb teeth are stationary and fabricated by DRIE of Si wafer. The upper comb teeth are fabricated by etching another Si wafer that is bonded to the

first wafer with a thin layer of thermally grown oxide in between. The top wafer also defines the mirror and torsion hinges. Scanning is realized when a voltage is applied between the upper and the lower comb electrodes, exerting a torque on the mirror and causing it to tilt. This mirror has diameter of 550 μm and is capable of scanning ±6.25° at resonance frequency of 34 kHz.

One disadvantage of staggered comb drives is the requirement for critical alignment of the stationary and moving comb teeth during the manufacturing process. To overcome this issue, angular vertical comb (AVC) actuators are fabricated from a single substrate. Patterson et al., developed a scanning micromirror based on AVC actuators [27]. In this approach, the moving comb fingers are attached to the torsion beams that suspend the mirror using PR hinges. When a voltage is applied between the movable and stationary fingers, the movable fingers rotate about the torsion beams, hence rotating the mirror. This type of actuators can provide larger scanning range compared to standard vertical comb drive actuators. The overall size of the scanning micromirror is 1×1 mm^2. The scanning angle of this micromirror is ±18° with driving voltage of 21 volts at resonance frequency of 1.4 kHz.

Using microlenses instead of micromirror has alignment advantage. Kwon et al. [28] used comb-drive actuators to scan microlenses in X and Y directions. They demonstrated the focus scanning of 75 μm with alternating (AC) voltage of 10 volts and direct (DC) bias of 20 volts.

1.3.2 Electromagnetic Actuators

In electromagnetic actuators, a magnetic field is used to move an object. The magnetic field can be from a permanent magnet or an electromagnetic coil. For example, if a current carrying wire is placed in an external magnetic field generated by a permanent magnet or an

electromagnet, the wire experiences a force (Lorentz Force) that is the result of interaction between the external magnetic field and the field generated by the current in the wire. Another case of magnetic actuation is when a ferromagnetic material is placed in an external magnetic field. Due to the misalignment of magnetic moments of domains that magnetizes the ferromagnetic material, magnetic force is exerted on the ferromagnetic material. This type of actuation has been used in development of endoscopic catheters for various microscopy techniques.

In 1994, Asada et al. [29] reported a 2-axis micromirror scanner driven by magnetic field. The scanner is micromachined from a Si substrate. The mirror is connected to a moving frame which itself is connected to a fixed frame using torsion beams. A pair of planer coils fabricated around the mirror and the moving frame and two permanent magnets are placed on both sides of the scanner. Actuation is realized by electromagnetic torque that is produced by the permanent magnets and controlling the electrical current in the planer coils. The scanner has overall dimensions of 7×7 mm^2 and is capable of scanning $\pm3°$ and $\pm1°$ about X and Y axes at resonance frequencies of 380 and 1450 Hz respectively.

Mitsui et al. [16] developed another 2-axis magnetically driven micromirror scanner that is suitable for OCT imaging. They used similar idea as Asada, but different configuration of magnet and coils to achieve a larger scanning range. In their device, a Si substrate was etched to form a mirror that is connected to a movable plate by a pair of torsion beams. Similarly, the movable plate is also connected to a fixed frame by the second pair of torsion beams. Two planar coils are fabricated adjacent to the mirror and connected in parallel for X-axis rotation. Four other planar coils for Y-axis rotation are fabricated and connected in parallel on the movable frame. The coils placed on opposite sides of the mirror and the movable plate

spiral in opposite directions. A permanent magnet is also placed under the device. Actuation about X and Y axes is realized by the electromagnetic torques that are produced when controlled electrical current is supplied to the coils. The scanner has the overall size of 7.4×9.8 mm^2 and is capable of ±8° scanning while driven in the static or low frequency (~10 Hz) mode, with a current of ±4.6 mA and ±10.3 mA in the X and Y axes, respectively.

Kim et al. [30] developed a catheter for high speed OCT imaging. It incorporates a magnetically actuated micromirror that is capable of 2-axis scanning. The actuation is realized by gluing a permanent magnet underneath the mirror and applying an external magnetic field using two coils. With a low driving voltage of up to 3 volts, the micromirror scans ± 20° and is capable of operating either statically in both axes or at the resonant frequency (>= 350Hz) for the fast axis. The catheter has diameter of 2.8 mm and rigid length of 12 mm.

Siu et al. [31] developed a transmissive microlens scanner. In this scanner a microlens is placed on a nickel platform that is suspended on a moving frame by four V-shaped springs. The moving frame is also suspended on a fixed frame using three serpentine springs. The microlens is actuated in the out-of-plane (Z-axis) direction using an electrostatic force that is generated by applying an AC voltage of 56 volts with a DC bias of 28 volts between the moving and fixed frames. The transverse (X-axis) actuation is realized by applying a 34.5 mT AC magnetic field to the nickel platform. Out-of-plane and transverse scanning ranges are 120 and 163 μm at resonance frequencies of 286 and 480 Hz respectively.

Min et al. [32] in 2009 demonstrated one dimensional optical fiber scanning by attaching a ferromagnetic iron-bead to the fiber and actuating by a magnetic force generated by a

solenoid. For the selected length of optical fiber (50 mm) the resonant frequency was 30 Hz with actuation range of 4 mm when 120 mA current was supplied to the solenoid. In 2011, using a similar approach they demonstrated two dimensional elliptical spiral scanning pattern of an optical fiber. This was achieved by placing the iron-bead off the axis of the solenoid [33].

1.3.3 Electrothermal Actuators

The principle of thermal actuators is based on the linear expansion of materials at elevated temperature. This phenomenon is used in MEMS thermal actuators to fabricate small size actuation mechanisms. The advantage of electrothermal actuation is mainly in large displacement compared to other types of actuation; however, scanning speed is limited by thermal dissipation rate of the actuator when cooled down from typically a few hundred degrees Celsius (°C). Most demonstrated electrothermal actuators have a scanning speed less than kHz. For out-of-plane actuation, bimorph beams consisting of two layers with different coefficients of thermal expansion can be used.

Pan et al. [34] developed a scanning micromirror connected to a frame by a bimorph actuator. The MEMS mirror is 1×1 mm^2 and is fabricated by DRIE etching of a Si substrate. The bimorph thermal actuator is composed of a stack of aluminum (Al) and SiO_2 thin films. A layer of polysilicon thermal resistor is embedded in the bimorph mesh and acts as a heat source from joule heating effects. Because of internal residual stress and difference in the thermal expansion of the layers in the hinge, the mirror curls to angle of about 17° after fabrication. The bimorph actuator can handle voltages up to 33 volts and the mirror has resonance frequency of 165 Hz and is capable of tilting ±8°.

Jain et al. [35] used similar approach to develop a 2-axis thermally actuated micromirror. This mirror is connected to a movable frame that itself is connected to a fixed frame using bimorph cantilever beams. This mirror has dimension of 1×1 mm^2 and can tilt 40° with the applied voltage of 15 volts. The frame can tilt 25° at 17 volts. The resonant frequencies of the mirror and frame actuator structures are 445 and 259 Hz, respectively.

Xie et al. [36] developed a thermal micromirror scanner for OCT applications. The micromirror is suspended using a series of bimorph cantilever beams. The actuation is realized by heating the bimorph beams by directly passing electrical current through them. The diameter of the head is 5.8 mm and the size of the mirror is 1×1 mm^2. This mirror is capable of scanning ±25° with driving voltage of less than 10 volts.

1.3.4 Piezoelectric Actuators

Piezoelectric effect causes crystalline materials such as quartz and ZnO to expand when charges are applied. The effect is reversible, meaning that a deformation in a piezoelectric material will generate electric charges. The advantage of piezoelectric actuator is high speed of operation; however, the displacement is relatively small compared to other types of actuation mechanism. Goto et al. demonstrated a resonator mirror fabricated by MEMS technology [37]. A piezoelectric actuator (PZT) is attached to the resonator that is fabricated from a Si substrate and is capable of scanning an optical beam in two directions. For 10 μm PZT actuation, the mirror scans 10° in one direction and 20° in the other direction. The resonance frequencies of the resonator are 121 and 288 Hz in both directions, respectively.

Another PZT actuator was developed by Tsaur et al. [38]. In this design, a micromirror with dimension of 500×500 μm^2 is hinged to four PZT cantilever beams. The overall size of the

device is 5×5 mm^2. Scanning angle of 6° at resonance frequency of 1975 Hz was demonstrated.

Fiber optic scanners have also been developed using piezo actuation techniques. Myaing et al. [39] have shown spiral scanning pattern of an optical fiber using a tubular PZT actuator. For an 8.2 mm long actuator, they achieved scanning diameters of 120-220 μm at frequency range of 1323-1330 Hz. The maximum driving voltage of the PZT actuator was 75 V.

1.4 Concluding Remarks

Among optical imaging techniques, confocal imaging can potentially provide highest resolution with modest cost. Confocal imaging that is based on native tissue properties, RCM, is preferred over fluorescence imaging (FCM) that requires exogenous contrast agents. Between actuation techniques used in MEMS scanners; electromagnetic actuation offers repeatable large scanning ranges with low driving voltages, which is preferred in clinical applications because of safety considerations. In this thesis, we utilize MEMS technology to developed electromagnetically driven lens and fiber optic scanners for reflectance confocal imaging of biological samples.

CHAPTER 2

A MICRO-FABRICATED OPTICAL SCANNER FOR REAL-TIME NON-CONTACT THICKNESS MEASUREMENTS[1]

2.1 Introduction

Various techniques are available for non-destructive thickness measurement of thin films and coatings. This includes ultrasonic [40], x-ray radiation [41] and optical methods via

[1] A version of this chapter has been published in journal papers and presented in conferences:

- **Mansoor, H**., Zeng, H., and Chiao, M. (2011) "Real-time thickness measurement of biological tissues using a microfabricated magnetically-driven lens actuator" Biomedical Microdevices. 13: 641–649.
- **Mansoor, H**., Zeng, H., and Chiao, M. (2011) "A microfabricated optical scanner for rapid noncontact thickness measurement of transparent films" Sensors and Actuators A: Physical. 167: 91–96.
- **Mansoor, H.**, Zeng, H., and Chiao, M. (2011) "A confocal fiber optic catheter for in vivo thickness measurement of biological tissues" IEEE 24th International Conference on MEMS, Cancun, Mexico. 999-1002.
- **Mansoor, H.**, Zeng, H., and Chiao, M. (2010) "Magnetically driven scanning microlens for out-of-plane in vivo medical imaging" 217th ECS Meeting. Vancouver, Canada.

reflection, transmission and interference measurement of light [42-44]. These techniques can be used to measure thickness of polymer films, optical coatings and PR layers in MEMS fabrication process. The choice of measurement technique depends on the material and the desired measurement resolution. Thickness measurements of biological tissues are also useful for studying pathological processes and diseases. For instance, the thickening of epithelium in the vocal folds is an indicator of early laryngeal cancer [45]. Another example is the measurement of the central corneal thickness that can be related to the intraocular pressure (IOP) to determine onset of glaucoma [46]. Thickness measurement of biological tissues has been demonstrated by radiography [47] and ultrasound [48]. More recently optical methods such as OCT [49, 50] and CM [51-55] have been developed for thickness measurements. In general, optical measurement techniques provide higher resolution and accuracy.

To perform rapid confocal measurements, MEMS technology can be employed. Using this technology, out-of-plane actuations of a microlens by mechanisms such as electrostatic [31, 56] and electrothermal [57] actuation have been demonstrated. In general, electrostatic actuators have disadvantage of non-linearity [58] and thermal actuators are limited by thermal fatigue due to continuous thermal cycling [59]. On the other hand, electromagnetic actuators typically require low driving voltage, have high repeatability and provide large scanning range. In this chapter we present development and evaluation of a magnetically driven confocal micro-scanner for rapid non-contact thickness measurement of transparent and semi-transparent films, as an alternative method to the current state-of-the-art equipment. In addition, we demonstrate development of an optical fiber catheter for thickness measurement of biological tissue for endoscopic applications.

2.2 Design and Principle of Operation

2.2.1 Scanner Optical Configuration

A typical optical configuration for confocal measurement is shown in Figure 2.1(a). The pinhole is of fixed size and position and it is realized using an optical fiber in our setup (Figure 2.1(b)). Both the illumination beam and the reflecting light from the sample will pass through the fiber but in opposite directions. The incident light will pass through the fiber to a collimating lens illuminating the objective lens. The light beam is then focused and after interacting with the sample, the elastically scattered light is collected and relayed back to the fiber for confocal imaging. Thus, the same fiber serves as both the illumination and the detection pinholes to achieve confocality. Using this optical configuration, the thickness of samples can be measured by actuating the objective lens in the Z-axis direction (Figure 2.1(b)) and monitoring the intensity of reflected light as a function of lens position.

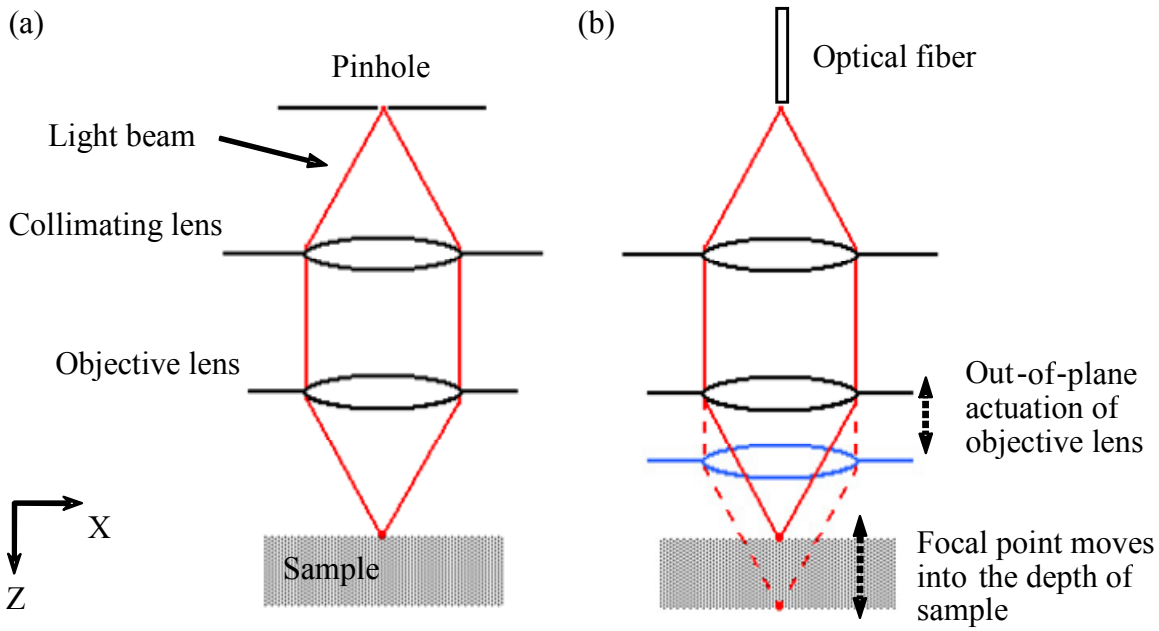

Figure 2.1 Optical configuration of confocal scanner for thickness measurement.

2.2.1.1 Thickness Measurement

When the objective lens is actuated in the Z-direction, the focal point of the lens scans a line perpendicular to the surface of the sample and passes through both upper and lower surfaces. The reflected light intensity is greater when the focal point is on the surface or at the layer boundaries with different refractive indices. Two intensity peaks will be detected each time the focal point scans across the thickness of sample (Figure 2.2(a)). The displacement of the lens between intensity peaks can be represented by:

$$d = A\sin(\omega t) \tag{2.1}$$

where A is the amplitude of lens actuation, ω is the frequency of actuation and t is time. Lens displacement between intensity peaks is known as the optical thickness of the sample [60].

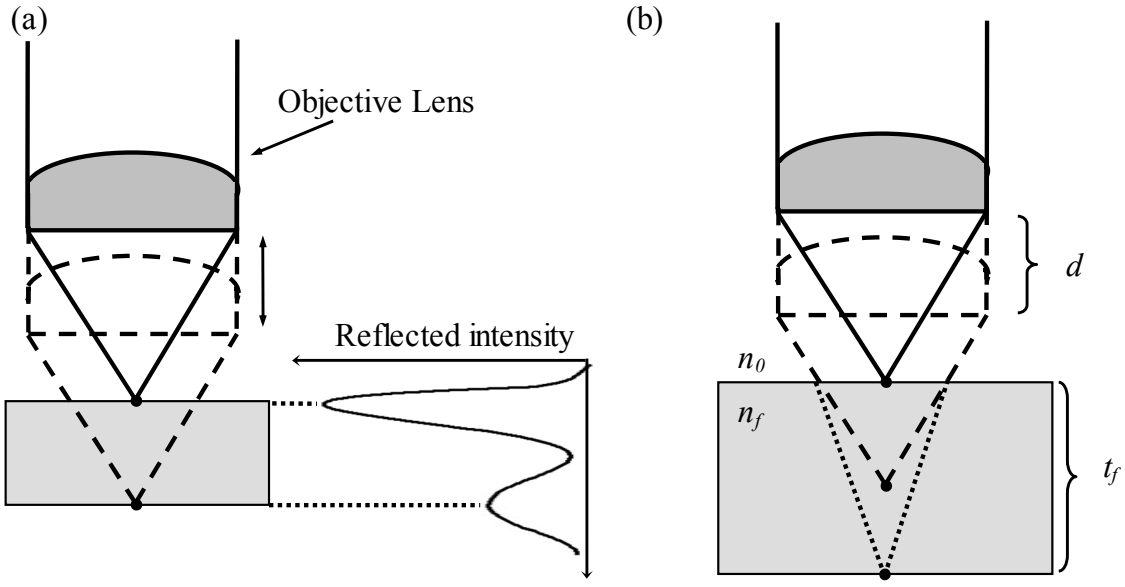

Figure 2.2 (a) Illustration of the working principle of confocal thickness measurement and a typical intensity signal. (b) The refractive index mismatch causes difference between mechanical (t_f) and optical (d) thickness of the sample.

This value is different than the mechanical (or physical) thickness because of the mismatch between the refractive indices of the sample and the surrounding medium (Figure 2.2(b)). The mechanical thickness of a sample such as a film is calculated using Eq. (2.2):

$$t_f = \frac{n_f}{n_0} d \tag{2.2}$$

In this equation, t_f is the film thickness, n_f and n_0 are the refractive indices of the film and air respectively and d is the lens displacement between intensity peaks.

2.2.1.2 Resolution

The performance of the confocal scanner in axial direction can be represented by thickness of optical section and calculated using [61]:

$$R_{axial} = \sqrt{\left(\frac{0.88 \times \lambda_e}{n - \sqrt{n^2 - NA^2}}\right)^2 + \left(\frac{\sqrt{2} \times n \times PH}{NA}\right)^2} \tag{2.3}$$

In this equation λ_e is the wavelength of excitation light, n is the refractive index of the medium, NA is the numerical aperture of the objective lens and PH is the pinhole or core diameter of the optical fiber. Using shorter wavelength light can improve the resolution of the scanner; however, for most fibers more photons are absorbed by the fiber at shorter wavelengths and less power is seen at the output. NA is another parameter that affects the resolution. Higher resolution can be achieved by using an objective lens with higher NA. The main parameter that governs the resolution of the confocal scanner is the pinhole size or core diameter of the optical fiber (PH). Smaller PH improves the resolution by rejecting the out-of-focus light; however, less light is received by the detector which results in higher

requirements on detection electronics. Larger *PH* lowers the resolution but requires a less sensitive detector.

The objective lens used in our confocal scanner is a Plano-convex lens with *NA* of 0.43. The fiber that was used is a single-mode optical fiber with core diameter of 8.2 μm. Theoretical axial resolution of the scanner is 28 μm. The axial resolution was also experimentally measured by axially scanning a flat mirror and logging the change in the reflected light intensity as the lens moved toward the mirror. The maximum intensity was when the mirror was at the focal plane of the lens. The experimental axial resolution is defined by the full width at half maximum (FWHM) of the signal peak which was measured to be 32 μm (Figure 2.3), very close to the above theoretical value of 28 μm.

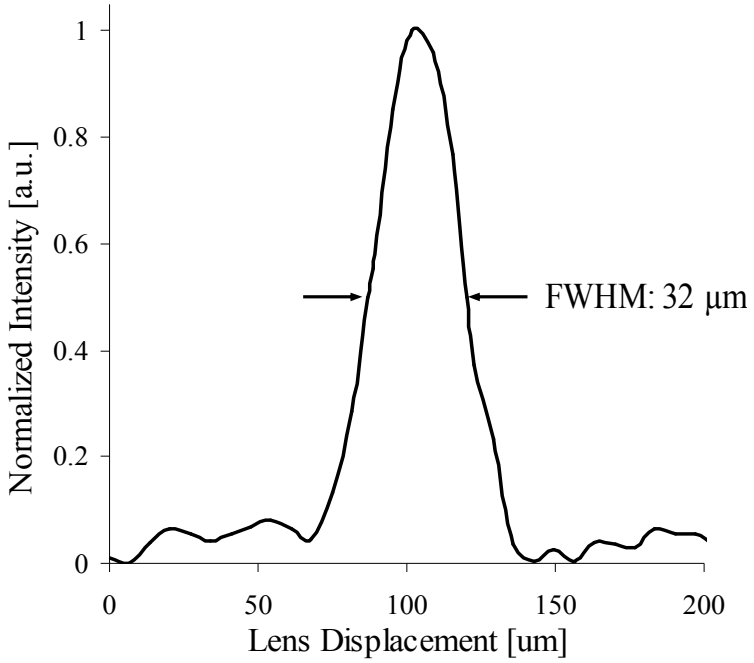

Figure 2.3 Reflected intensity as a function of lens displacement from axial scan of a flat mirror. The measured FWHM was 32 μm.

2.2.2 Lens Actuation

The lens is suspended on a micro-fabricated nickel flexure. The out-of-plane (Z-axis) actuation is realized by applying an AC magnetic field generated by an electromagnetic coil to the flexure. Figure 2.4(a) shows a conceptual illustration of this actuator.

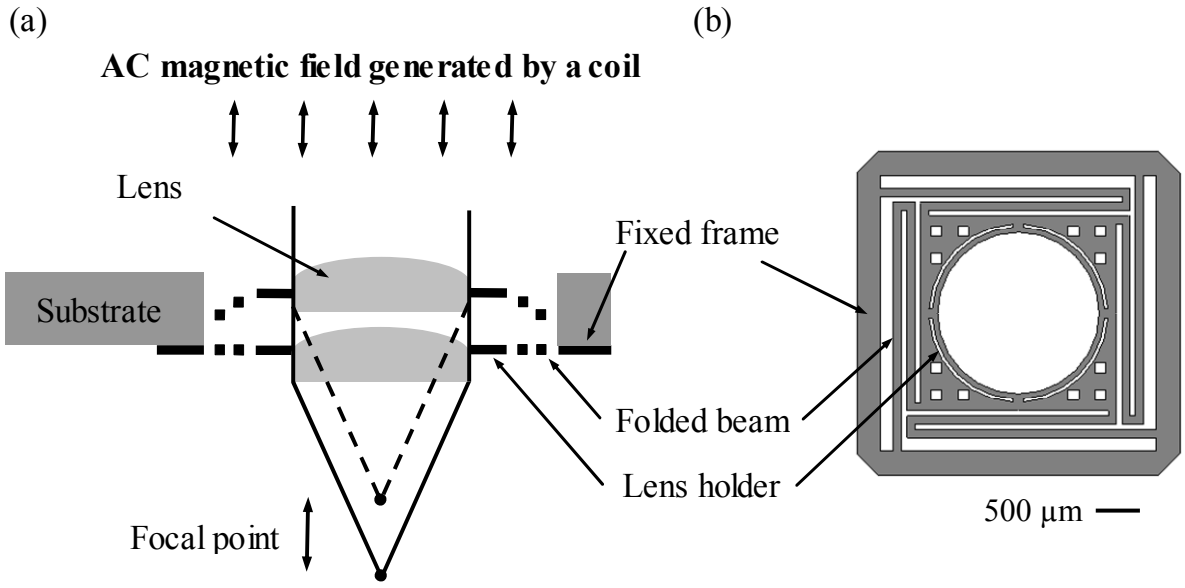

Figure 2.4 (a) Conceptual illustration of microlens scanner with a suspension system made of a magnetic material (nickel). Out-of-plane scanning is enabled by an external magnetic field. (b) Layout of out-of-plane scanning flexure. The diameter of the lens is 1.5 mm, the width of folded beams is 75 µm and the overall size of the scanner is 3 mm ×3 mm.

The magnetic force applied to the nickel flexure can be approximated by the virtual work method [62]. The net work in the electromagnetic system is approximated by the expression:

$$W_{mag} = \frac{\phi F_{mmf}}{2} \tag{2.4}$$

In Eq. (2.4), ϕ is magnetic flux and F_{mmf} is magnetomotive force that is defined as the product of $N.i$, where N is the number of turns and i is the current flow in the coil. Magnetic flux and magnetomotive force are related by the expression:

$$\phi = \frac{F_{mmf}}{\Re} = \frac{Ni}{\Re} \tag{2.5}$$

where $\Re$ is the reluctance encountered by the flux in its path that is approximately:

$$\Re = \frac{g_z}{\mu_0 A} \tag{2.6}$$

In Eq. (2.6), g_z is the gap between the coil and nickel flexure μ_0 is permeability of free space and A is cross-sectional area of the electromagnet core. Replacing equations (2.5) and (2.6) in Eq. (2.4) will give:

$$W_{mag} = \frac{\mu_0 A N^2 i^2}{2 g_z} \tag{2.7}$$

The magnetic force acting on the nickel flexure is finally approximated by the following expression:

$$F_{mag} = -\frac{dW_{mag}}{dg_z} = -\frac{\mu_0 A N^2 i^2}{2 {g_z}^2} \tag{2.8}$$

The squared current term (i^2) in Eq. (2.8) shows that the magnetic force (F_{mag}) is always in the same direction, independent of the direction of the current in the coil. This means that when a sinusoidal current with zero DC bias is applied to the coil, the nickel flexure's actuation frequency is twice the applied current frequency. This so called double-frequency

effect is expected since the displacement of the nickel flexure is always toward the coil regardless of the direction of applied current [63].

The lens actuator consists of four folded beams attached to a fixed frame at one end and a lens holder at the center. Figure 2.4(b) shows the design layout of the nickel flexure. The stiffness of the flexure can be modeled as four folded beams in parallel. The stiffness of each folded beam can also be approximated by assuming each suspension consists of two fixed-guided beams of length $l_b/2$ in series and zero rotation at the joint [64].

$$k_{total} = 4 \times k_{beam} = \frac{192EI}{l_b^{\,3}} \tag{2.9}$$

In Eq. (2.9) E is the Young's modulus of nickel, I is the moment of inertia of beam and l_b is total length of each folded beam. The restoring force of the nickel flexure as a function of deflection can be approximated as:

$$F_s = 4F(z) = \frac{192EI}{l_b^{\,3}} d_z \tag{2.10}$$

where $F(z)$ is the restoring force of one beam and d_z is the displacement of the flexure. Eq. (2.10) is derived by assuming s-shaped deformation of the flexure as shown in Figure 2.5.

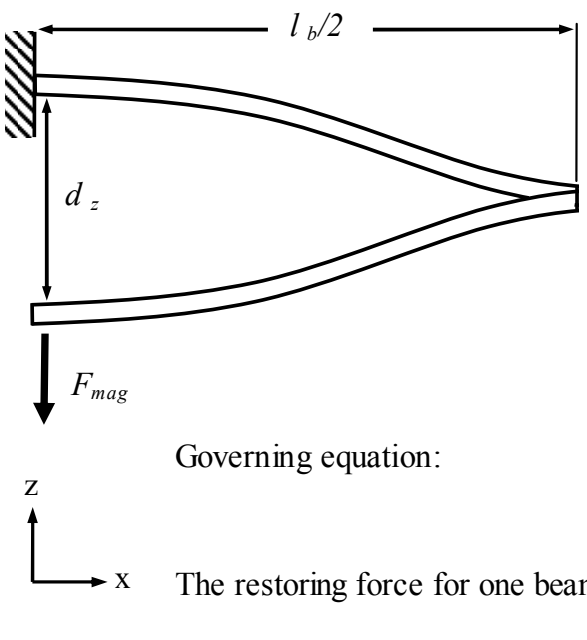

Boundary conditions:

$$z(0) = 0$$

$$\left.\frac{\partial z}{\partial x}\right|_{x=l_b/2} = 0$$

$$\left.\frac{\partial z}{\partial x}\right|_{x=0} = 0$$

Governing equation:

$$\frac{\partial^3 z}{\partial^3 x} = -\frac{F}{EI}$$

The restoring force for one beam:

$$F(z) = \frac{48EI}{l_b^{\,3}} d_z$$

Figure 2.5 Illustration of the flexure deformation and derivation of the restoring force for the electromagnetic microlens actuator.

When a sinusoidal current with frequency of ω_i is applied to the coil, a harmonic electromagnetic force with frequency of $2\omega_i$ is produced by the coil. The vibration mode frequencies can be predicted using the equation of motion of the system [65]. Assuming damped vibration under harmonic magnetic force, the equation of motion for the system becomes:

$$m\ddot{z} + c\dot{z} + kz = F(t) \tag{2.11}$$

where m is mass, c is damping constant and k is stiffness of the system. The amplitude of the displacement, d_z, of the nickel flexure at various excitation frequencies can be expressed as [66]:

$$d_z = \frac{F_{mag}}{k} \frac{1}{\left\{\left[1-\left(\frac{\omega}{\omega_n}\right)^2\right]^2 + \left[2\zeta\frac{\omega}{\omega_n}\right]^2\right\}^{\frac{1}{2}}} \tag{2.12}$$

where ω is the frequency of actuation, ω_n is the natural frequency of the structure and ζ is the damping ratio of the system. The nickel flexure actuates in the first mode of vibration that is the out-of-plane sliding mode.

Finite Element Analysis (FEA) was performed on the flexure design using COMSOL Multiphysics. Figure 2.6 is the FEA results of the nickel flexure deformation at resonant frequency. The predicted actuation range and resonant frequency of the flexure were 220 µm and 530 Hz respectively when a 14 mT AC magnetic field is applied.

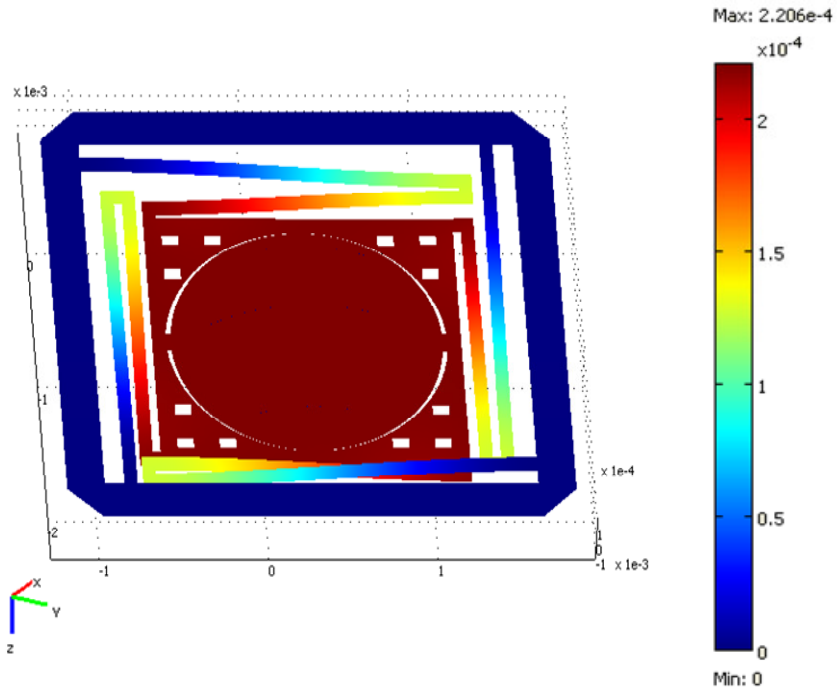

Figure 2.6 FEA simulation of nickel flexure after lens installation. The simulation result for resonant frequency and maximum vertical displacement are 530 Hz and 220 µm respectively.

2.3 Fabrication Process

2.3.1.1 Flexure Fabrication

Electroplating technique is used to fabricate the nickel flexure as shown in Figure 2.7.

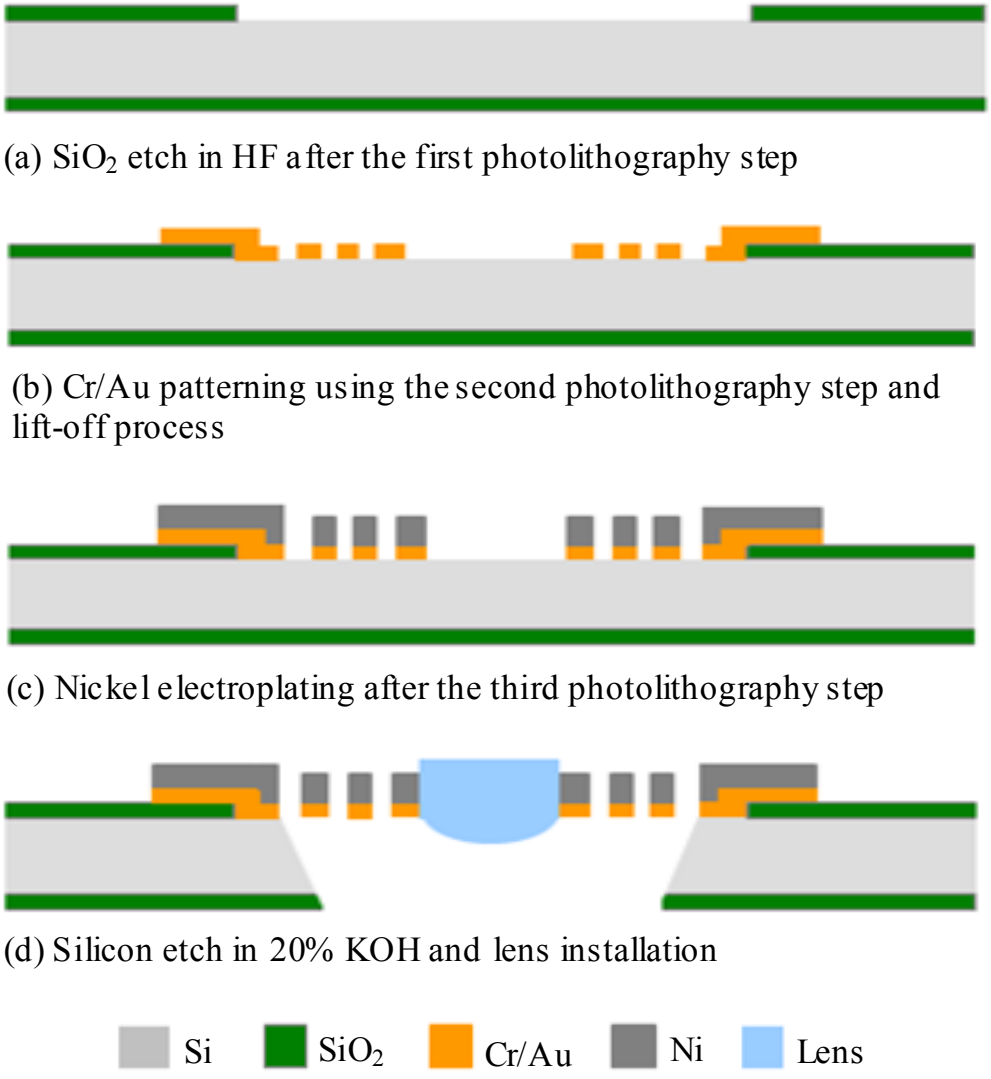

Figure 2.7 Schematic drawing of the MEMS nickel flexure fabrication steps.

First a 2 μm thick SiO_2 layer is thermally grown on both sides of a 300 μm thick Si wafer. After the first photolithography step, SiO_2 is etched in a 7:1 buffered oxide etch (BOE) solution (Figure 2.7(a)). An electrode area for electroplating is defined by the second

masking step followed by deposition of 50 nm chromium (Cr) and 150 nm gold (Au), and a lift-off process to remove excess/ unwanted Cr/Au (Figure 2.7(b)). A mold for electroplating nickel is fabricated on the Si substrate using a thick layer of SPR 220-7 PR. A 20 μm thick nickel layer is electroplated on the substrate and the PR mold is removed with acetone (Figure 2.7(c)). The Si beneath the nickel flexure is then etched in a 20 wt% KOH at 85 °C to suspend the nickel flexure. Finally, the lens is fixed into the lens holder using a UV-curable adhesive (Figure 2.7(d)) (see Appendix A for details on fabrication process).

Figure 2.8 shows photos of two lens actuators fabricated by electroplating technique described above.

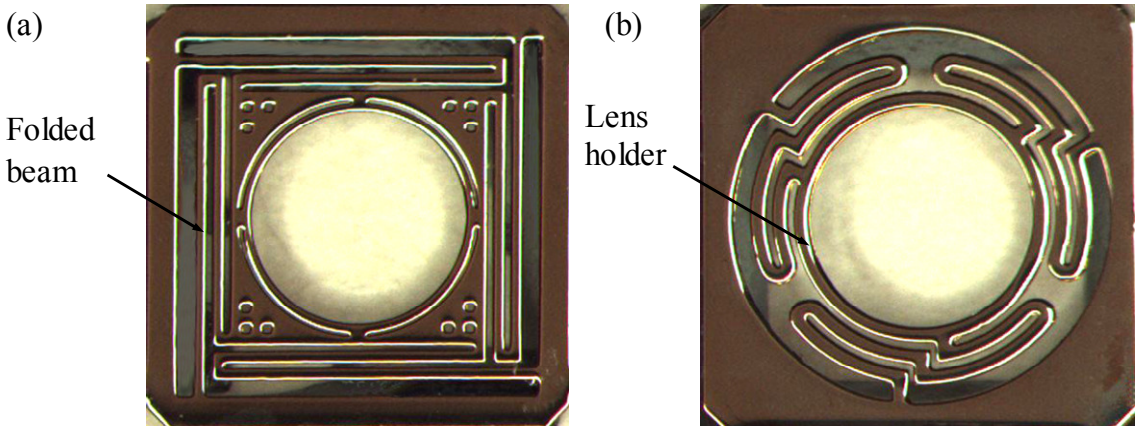

Figure 2.8 Photos of electroplated lens actuators before lens installation showing flexures with (a) four rectangular and (b) three circular folded beams. Lens holder has diameter of 1.5 mm.

2.3.1.2 Scanner Assembly and Characterization

The MEMS actuator is then placed on an electromagnetic coil that was wound using American wire gauge (AWG) #44 on a hollow cylindrical core. The coil has an outer diameter of 4 mm and is capable of producing a 14 mT magnetic field with an AC current of

60 mA_{rms}. Figure 2.9(a) shows the photo of the fabricated lens actuator attached to the coil. The out-of-plane displacement of the lens at various frequencies was measured using a Laser Doppler Vibrometer (LDV) (Figure 2.9(b)). The measured resonant frequency of the lens actuator was 544 Hz with a maximum displacement of 204 μm. This is very close to the simulation results of 530 Hz and 220 μm. The small difference between the measured values and simulation prediction is mainly due to the non-uniformity in the thickness of the electroplated nickel flexure during fabrication process (see appendix A for details).

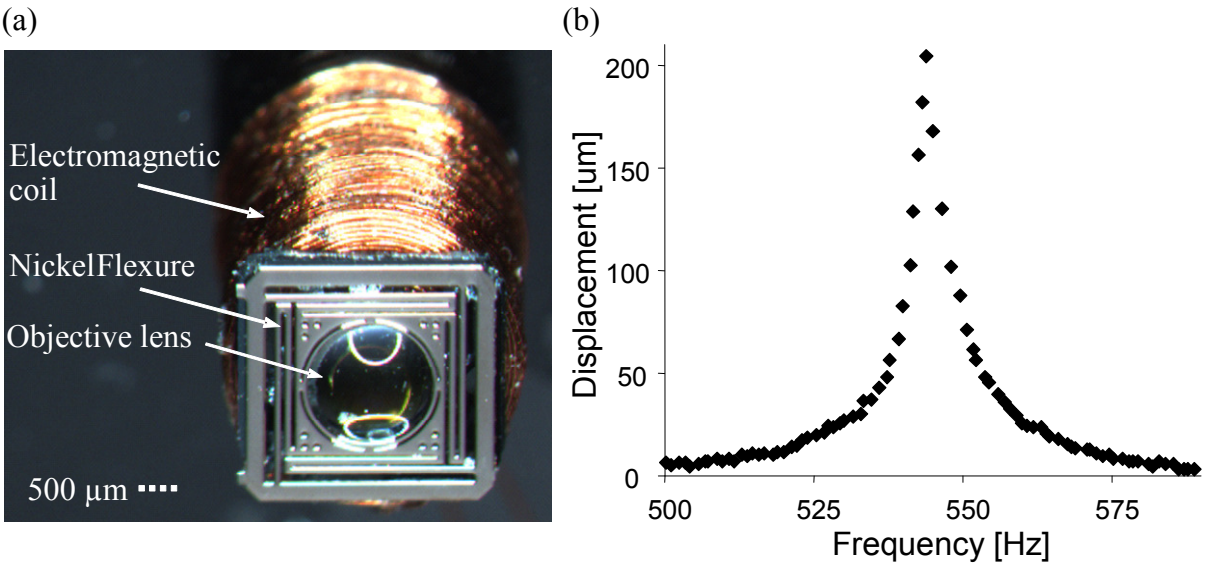

Figure 2.9 (a) Photo of the MEMS nickel flexure with a lens attached to an electromagnetic coil for out-of-plane scanning. (b) Frequency response of microlens scanner measured by a LDV.

A collimating lens was placed inside the core of the electromagnetic coil and the coil-lens assembly was positioned in front of an optical fiber to form the confocal catheter (Figure 2.10(a)). The catheter has a rigid length of 30 mm and an outer diameter of 4.75 mm. Figure 2.10(b) shows the positions of the optical components and the electromagnetic coil at the tip of the catheter.

(a)

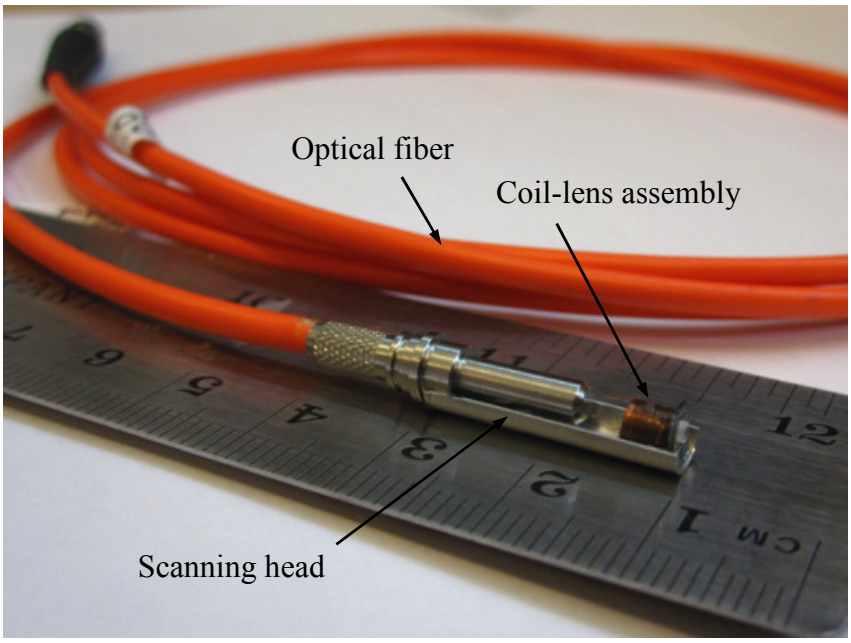

(b)

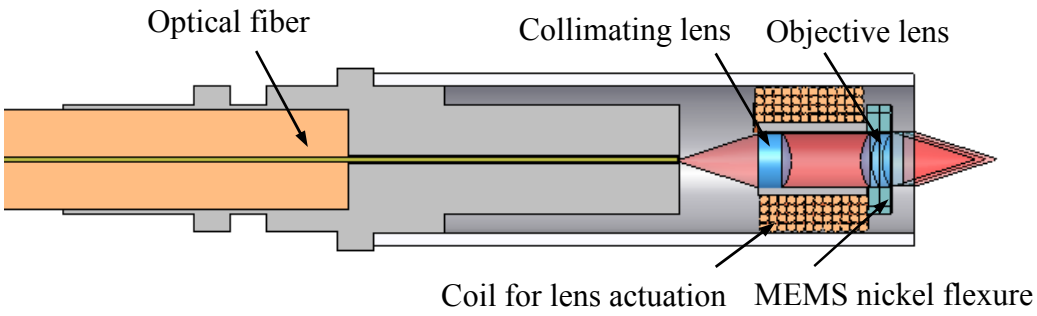

Figure 2.10 (a) Photo of the confocal catheter, (b) Cross-sectional drawing of the confocal scanner showing positions of the optical components, electromagnetic coil and lens actuator.

2.4 Experimental Setup and Results

2.4.1 Signal Acquisition

The schematic diagram of experimental setup for film thickness measurement is shown in Figure 2.11.

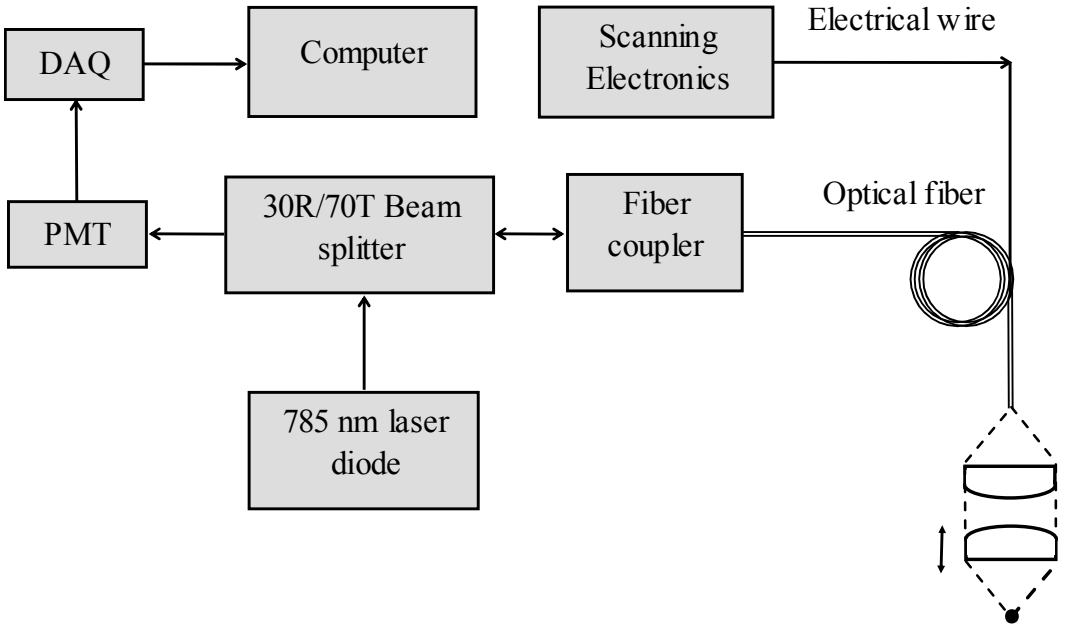

Figure 2.11 Schematic of experimental setup.

A 785 nm laser beam is directed toward a fiber coupler by a 30:70 (30% reflectance and 70% transmission) beam splitter. A single-mode optical fiber is used to transfer the laser beam to the scanner and relay back the reflecting light from the sample to a photomultiplier tube (PMT). PMT converts the intensity of the reflecting light to electrical signal. The output of the PMT is connected to a data acquisition (DAQ) card for intensity signal measurement which is displayed in real-time on a computer monitor. The MEMS device is controlled by scanning electronics including a function generator, an amplifier and an oscilloscope.

2.4.2 Experimental Results

To demonstrate functionality of the system, the scanner was used to measure thicknesses of layers of PR deposited on Si wafers and also biological tissues.

2.4.2.1 PR Thickness Measurements

The PR used for the experiment was SU-8 3050 negative PR (MicroChem Corp.). Five different thicknesses were spin-coated on 4 inch diameter Si wafers. Thicknesses of SU-8 layers were measured by Wyko optical profiling system (Veeco Instruments Inc.) [67] and recorded for comparison to our measurements. The samples were positioned in front of the objective lens of the MEMS scanner and the intensity signal of reflected light was collected using the PMT while the scanner was operating at its resonant frequency (544 Hz). Eq. (2.1) is used to plot the intensity signal against the lens displacement. The value used for the amplitude of vibration (A) in Eq. (2.1) was 102 μm which is equal to the half of the maximum peak-to-peak displacement of the lens. Figure 2.12 shows the intensity signal obtained from one of the thickness measurement trials while the objective lens was moving toward the sample. The first intensity peak corresponds to the reflection from the surface of the PR and the second peak is reflection from the surface of the wafer. From this plot, the lens displacement between intensity peaks is measured and the thickness of the SU-8 layer is calculated to be 94.5 μm based on Eq. (2.2). The value used for the index of refraction of the SU-8 was 1.56 [68]. The thickness of the sample measured by Wyko optical profiler was 88.6 μm. Similarly, the thicknesses of all other PR samples were measured by both the confocal scanner and Wyko optical profiler. For each sample, the measurement was repeated 6 times. Table 2.1 summarizes the mean thickness values and standard deviations of repeated

measurements by Wyko optical profiler and confocal scanner. The differences between the measured thicknesses using both methods and their standard deviations are also presented.

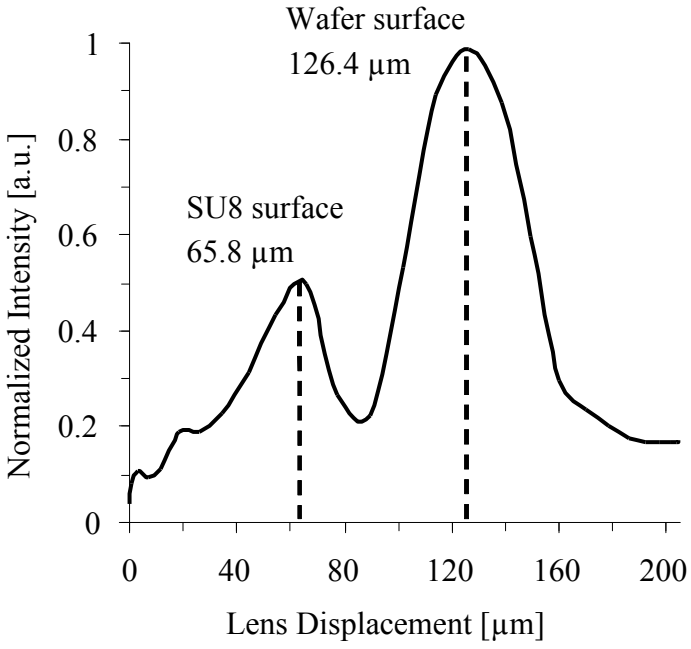

Figure 2.12 The intensity peak obtained from the scanner when the lens moved toward the sample.

	Wyko optical profiler		Confocal scanner		Wyko - confocal	
Sample #	Mean Thickness [μm]	Standard Deviation [μm]	Mean Thickness [μm]	Standard Deviation [μm]	Difference of mean thickness [μm]	Standard Deviation [μm]
1	47.05	0.06	43.57	6.72	3.48	6.77
2	68.79	0.04	76.17	5.10	-7.38	5.07
3	88.67	0.09	92.77	4.78	-4.10	4.84
4	127.43	0.23	125.06	6.60	2.37	6.69
5	178.70	1.16	179.57	6.05	-0.87	5.12

Table 2.1 SU-8 PR thickness measurement results from Wyko optical profiler and confocal scanner.

2.4.2.1.1 Statistical Analysis

The mean thickness measured using the confocal scanner was plotted against the mean thickness measured by Wyko optical profiler with error bars of two standard deviations (Figure 2.13). This plot shows good linearity of the scanner response in terms of thickness measurement and high correlation between the two measurement methods. This correlation shows the strength of the relation between methods of measurement; however, for proper comparison, the agreement between data must be investigated [69].

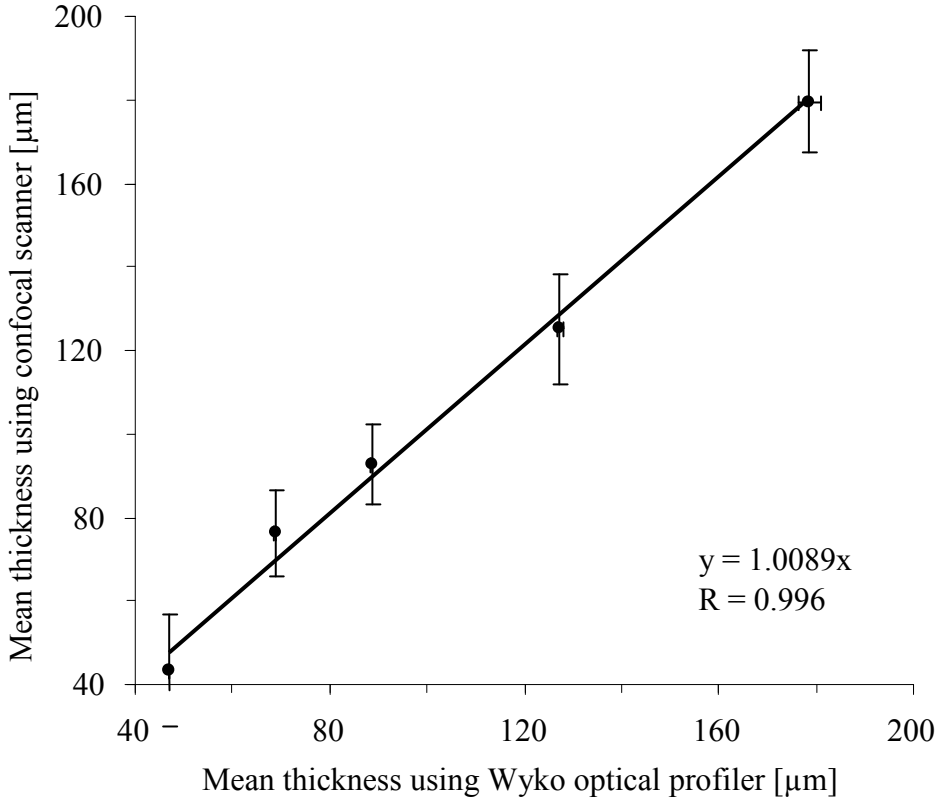

Figure 2.13 Plot of the mean SU-8 photoresist thickness measurement using confocal scanner and Wyko optical profiler.

Figure 2.14 is the Bland-Altman plot of the measurement data. This plot represents the difference between the measured thicknesses against mean thicknesses from both measurement methods. From the measurement data, the mean difference is -1.30 μm with mean standard deviation of 5.70 μm. Assuming a normal distribution, we would expect most of the differences in the measured thickness lie within the 95% confidence interval (two standard deviations). From this we can conclude that using the current confocal system, the measurement may be -12.7 μm below or 10.1 μm above that determined by the Wyko optical profiler. This is consistent with the resolution of our confocal scanner as determined in section 2.2.1.2.

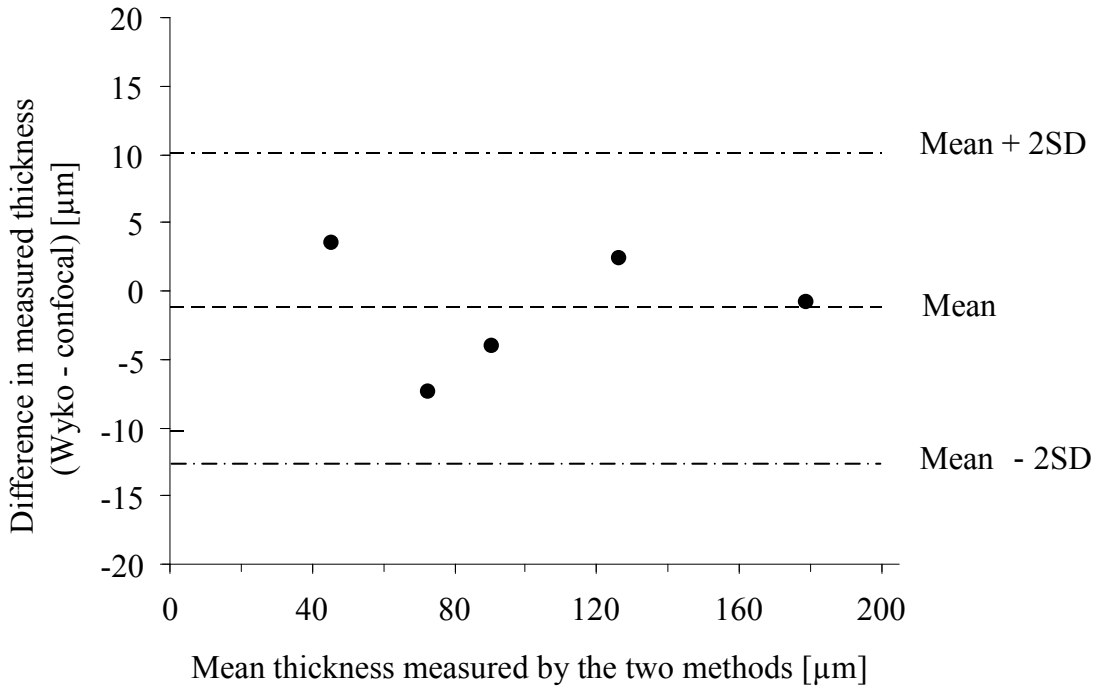

Figure 2.14 Bland-Altman plot of thickness measurement comparison between our confocal scanner and Wyko optical profiler. SD: standard deviation.

The uncertainty of measurement for the confocal scanner was approximated by combining the Type A uncertainties of the sample thickness measurement by confocal scanner and the lens displacement measurements by LDV. The expanded uncertainty of measurement (for 95% confidence interval) using the current confocal scanner was found to be 11.86 µm.

2.4.2.2 Biological Tissue Thickness Measurement

The confocal catheter was used to measure the corneal thickness of a 5-months-old female C3H/HeN mouse. After measurement, the eye was removed, fixed, and stained with hematoxylin and eosin (H&E) for histology examination. Sectional histological images of the cornea (Figure 2.15) were obtained and used to measure the corneal thickness for comparison with our catheter measurements. The average corneal thickness from histology images was measured to be 94.4 µm by ImageJ processing software [70].

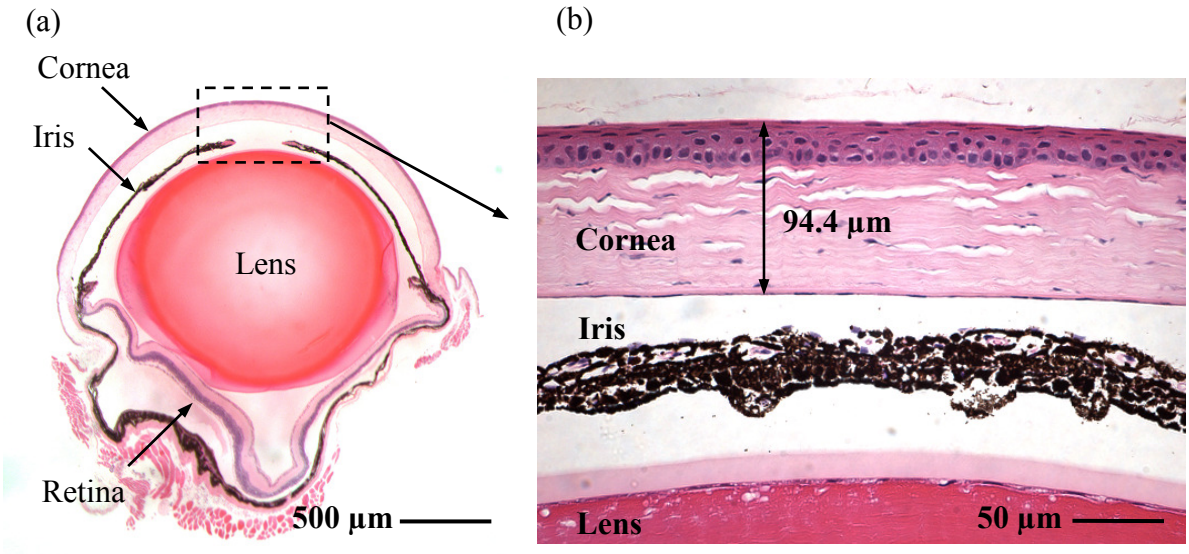

Figure 2.15 (a) H&E image of an eyeball from a 5-months-old female C3H/HeN mouse after standard histology processing, (b) magnified image of mouse corneal section. The mean corneal thickness measured from this histology image was 94.4 µm.

Figure 2.16(a) shows the intensity signal obtained from our MEMS confocal catheter measurement of the mouse eye. The optical signal intensity is plotted versus the objective lens displacement for a half-cycle lens actuation. The two intensity peaks correspond to the light reflection from the epithelium and endothelium layers of the cornea. The lens displacement between the two peaks on the curve is 69.2 µm. Using Eq. (2.2) and assuming the refractive index of the mouse cornea to be 1.4015 [71] the calculated thickness of the cornea is 97 µm. This is very close to the histology results of 94.4 µm.

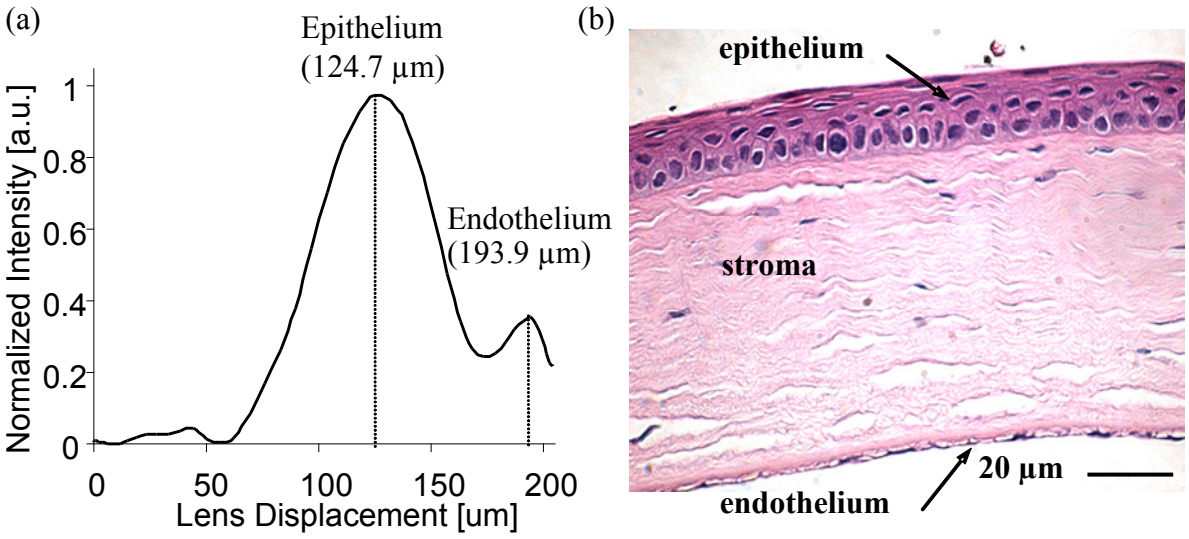

Figure 2.16 (a) Reflected intensity from the mouse cornea as a function of lens displacement. Intensity peaks in the graph correspond to the reflected light from the surface of epithelium and endothelium. The corneal thickness is calculated to be 97 µm assuming a refractive index of 1.4015, (b) zoomed view of the H&E image of the mouse cornea section shown in Figure 2.15.

Similar experiment was performed to measure the thickness of mouse skin. Figure 2.17(a) shows the intensity signal obtained from the skin measurement experiment. The two intensity peaks correspond to the light reflection from air-stratum corneum interface and the dermis-subcutaneous fat interface. The measured lens displacement between intensity peaks is

139.4 µm which corresponds to a tissue thickness of 195.2 µm using Eq. (2.2) and assuming a skin refractive index of 1.4 [72]. Figure 2.17(b) is the histology section of the mouse skin used in this experiment. The average skin thickness measured from histology section was 178.8 µm.

The thickness from the histology measurements are less than the values measured by the confocal catheter, for both cornea and skin tissues. The differences could be related to the variation in the refractive indices and the shrinkage of the tissue as a result of formaldehyde fixation in the histology processing [73].

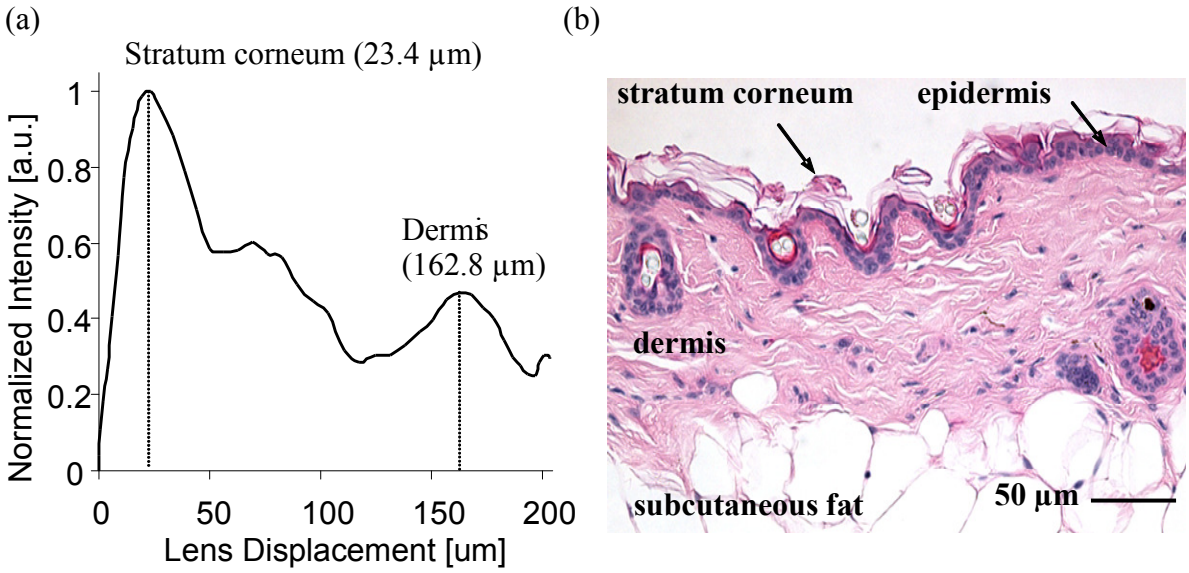

Figure 2.17 (a) Reflected intensity from mouse skin as a function of lens displacement. Intensity peaks in the graph correspond to the reflected light from the surface of the skin (stratum corneum) and the boundary between dermis and fat tissue. The skin thickness is calculated to be 195.2 µm assuming a refractive index of 1.4, (b) H&E image of mouse skin section.

2.5 Concluding Remarks

The design and fabrication of a magnetically driven lens actuator using MEMS technology was demonstrated in this chapter. The lens actuator was used for non-contact confocal thickness measurement of transparent and semi-transparent films, and biological tissue samples. Thickness measurement of five different SU-8 PR layers deposited on Si wafers and cornea and skin of a mouse were demonstrated. The device has a resolution of 32 μm with expanded uncertainty of measurement (for 95% confidence interval) of 11.86 μm. The lens actuator is used to develop two-dimensional laser scanners for confocal imaging of biological tissue that is presented in Chapter 3.

CHAPTER 3

VERTICAL OPTICAL SECTIONING USING A MAGNETICALLY DRIVEN CONFOCAL MICROSCANNER[2]

3.1 Introduction

In confocal microscopy, a beam of light is focused on a sample by an objective lens. Imaging is usually performed by scanning of the focused light in the X-Y plane (X-Y plane is parallel to the surface of the sample). Scanning of the light beam can be performed using micro-mirrors developed by MEMS technology [74-77] or by optical fibers [78-80]. This will result in horizontal optical sectioning that produces an image of a section that is parallel to the

[2] A version of this chapter has been published in a journal and presented in a conference:

- **Mansoor, H.**, Zeng, H., Chen, K., Yu, Y., Zhao, J., and Chiao, M. (2011) "Vertical optical sectioning using a magnetically driven confocal microscanner aimed for in vivo clinical imaging" Optics Express. 19(25): 25161-25172.
- **Mansoor, H.**, Chen, K., Yu, Y., Zhao, J., Zeng, H., and Chiao, M. (2012) "Histology-equivalent vertical optical sectioning using a 2-axis magnetic confocal microscanner" Solid-State Sensors, Actuators, and Microsystems Workshop, Hilton Head Island, South Carolina, USA, 397- 400.

surface of the sample. In conventional histopathology preparation procedures, samples are cut in transverse slices. Images obtained from this process show a vertical cross-section of the sample. Therefore, a confocal device capable of obtaining vertical cross-sectional images is very useful for clinical applications. One method of in-direct vertical sectional imaging is collecting and stacking horizontal section images obtained from various depths within the sample [81]. The disadvantage of this method is a long scanning time if high resolution imaging is desired. A better method of optical vertical sectioning is direct raster scanning of a focused laser beam in the X-Z plane (X-Z plane is perpendicular to the surface of sample). This will provide real-time images that are analogues to histopathology images which pathologist and clinicians are more familiar with.

Direct vertical confocal imaging in the X-Z plane has been previously demonstrated by various methods. This includes focusing a beam of light on a specimen and moving the sample in the X-Z plane using a piezo translation stage [82] or scanning a laser spot in transverse (X-axis) direction using a galvanometer mirror and translating the specimen using a piezo stage for axial (Z-axis) scan [83]. In another work, transverse and axial scans were performed by a galvanometer mirror and a commercial piezo-actuated macroscopic objective lens respectively [84]. The whole assembly is large in size and is intended for laboratory desktop microscopy applications. Those implementations are not suitable for *in vivo* clinical patient measurements, especially for internal organ imaging through an endoscope. For *in vivo* clinical applications, the sample (our epithelial tissues as part of our body) cannot be moved for the purpose of imaging. The scanners have to be miniaturized to the size of millimeters or several millimeters and also be safe to the patient, thus present significant engineering challenges. Utilizing MEMS technology is the way of choice to overcome these

challenges. Recently, a group has proposed direct vertical imaging by mounting a micromirror developed by MEMS technology on a stage and actuating the stage in the axial direction using piezoelectric unimorph beams [85].

In this chapter we present another way of direct vertical sectional imaging by scanning a laser beam in transverse direction using an optical fiber and in axial direction through actuating an objective lens with the aim of real-time *in vivo* imaging. In this work, we have coupled a magnetic lens actuator with a transverse fiber optic actuator to form a 2-axis confocal scanner for direct vertical cross-sectional imaging of samples. In addition, laser micromachining technique is utilized to fabricate the magnetic actuators. In this scanner, fiber and lens actuators are mechanically decoupled, eliminating translational errors and any interference or coupling effects between the actuation systems. Optical and mechanical design and characterization of a 2-axis confocal scanner for vertical optical sectioning are presented. Preliminary two-dimensional confocal imaging of samples is also demonstrated.

3.2 Design and Principle of Operation

3.2.1 Instrumentation

Figure 3.1 (a) shows the optical configuration of a 2-axis confocal scanner. A beam of light is illuminated from a single mode optical fiber (SMF) and is collimated by a collimating lens. The light is then focused on a sample by an objective lens. In order to scan a vertical cross-section of the sample, both transverse and axial scanning of the focused beam is required. The frequency ratio and desired number of pixels in the image defines the scanning rate of device. In our system fast-axis scanning is performed by actuating the objective lens in axial direction and slow-axis scanning is done by moving the optical fiber in transverse direction.

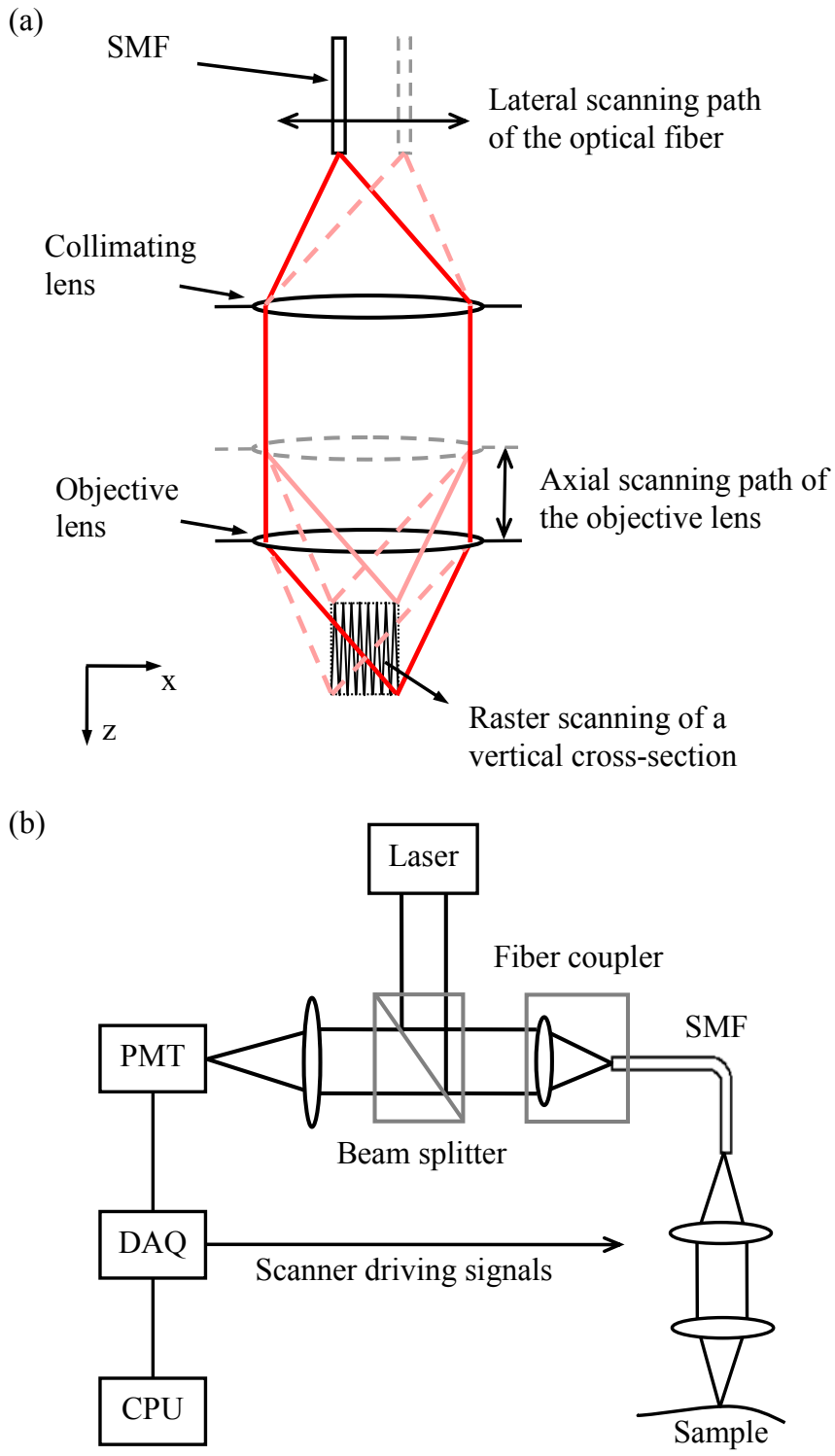

Figure 3.1 (a) Optical configuration of the 2-axis confocal scanner. The optical fiber and objective lens are capable of scanning in transverse (X-axis) and axial (Z-axis) directions respectively. (b) Schematic diagram of the experimental setup.

A schematic diagram of 2-axis confocal system is provided in Figure 3.1 (b). A beam of light with wavelength of 785 nm is emitted from a laser source (SDL XC30). The beam is directed to a single mode fiber coupler (Newport Corp.) using a 30R/70T beam splitter. After scanning the sample, the reflected light is relayed to a PMT through the same optical fiber. A DAQ card is used to collect the intensity signal from the PMT and to generate the driving signals for the scanner. The intensity signal is converted to a two-dimensional image using a computer.

3.2.2 Magnetic Actuators

3.2.2.1 Fiber Actuator

To prevent the fiber from scanning in unwanted directions due to misalignment with the applied magnetic field or external vibrations, the stiffness of the fiber actuator in X-axis is designed to be much smaller than that in Y-axis. This is achieved by mounting an optical fiber on a 25 mm × 2 mm cantilever beam that was fabricated by laser micromachining of a 25.4 μm thick nickel foil. A groove was created at the center and along the length of the beam to hold the optical fiber. One side of the cantilever beam was mounted to a v-groove fiber holder and an electromagnetic coil was place at the other side of the beam. When an alternating magnetic field is generated by the coil, the nickel beam is pulled toward the coil and released resulting in forced transverse actuation of the optical fiber. The length of the optical fiber is 30 mm and the tip of the fiber can actuate 450 μm in X direction. The cantilever beam undergoes simple forced actuation and can be modeled as a beam with one end fixed and the other end free (Figure 3.2). The deflection at the tip of the fiber can be approximated by [86]:

$$d_x = \frac{F_{mag} l_c^{\,2}}{6EI}(l_c - 3l_f) \tag{3.1}$$

where F_{mag} is the electromagnetic force exerted on the beam, l_f is the length of the fiber, l_c is the length of the cantilever beam, I is the moment of inertia and E is the Young's modulus of the beam.

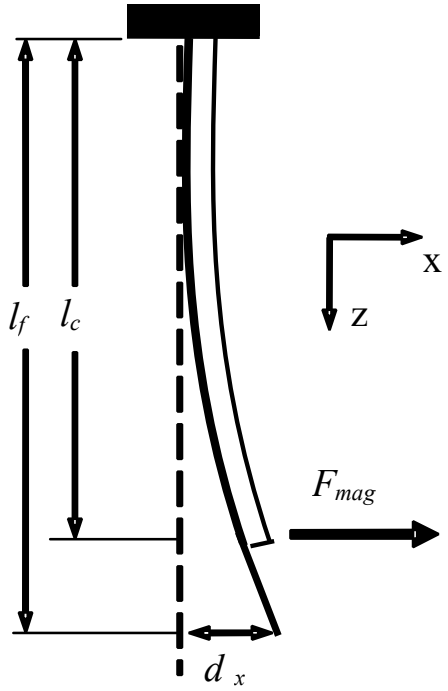

Figure 3.2 (a) Deflection diagram of cantilever/fiber actuator for transverse scanning. (b) Deflection diagram of one of the four folded beams for axial scanning of a lens.

3.2.2.2 Lens Actuator

Lens actuator utilizes a similar design that we described in the previous chapter; however, this time instead of electroplating nickel on a Si substrate, we used a nickel foil and laser micromachining technique to fabricate the nickel flexure. The flexure consists of four folded

beams that suspend the objective lens in an electromagnetic field. The width and total length of each folded beam are 0.125 mm and 8.7 mm respectively. The flexure thickness is 56 µm. The objective lens is mounted in the lens holder using UV-curable adhesive. When the nickel flexure is placed in an alternating magnetic field, the lens actuates in Z-direction.

3.3 System Description and Characterizations

3.3.1 Actuators Fabrication and Assembly

A Commercial laser machining system (New Wave Research QuikLaze system) was used to fabricate the nickel flexure and cantilever beam. The selected laser wavelength was green (532 nm) with energy of 3 mJ. The cutting speed was 15 µm/s and the laser pulsed at 50 Hz.

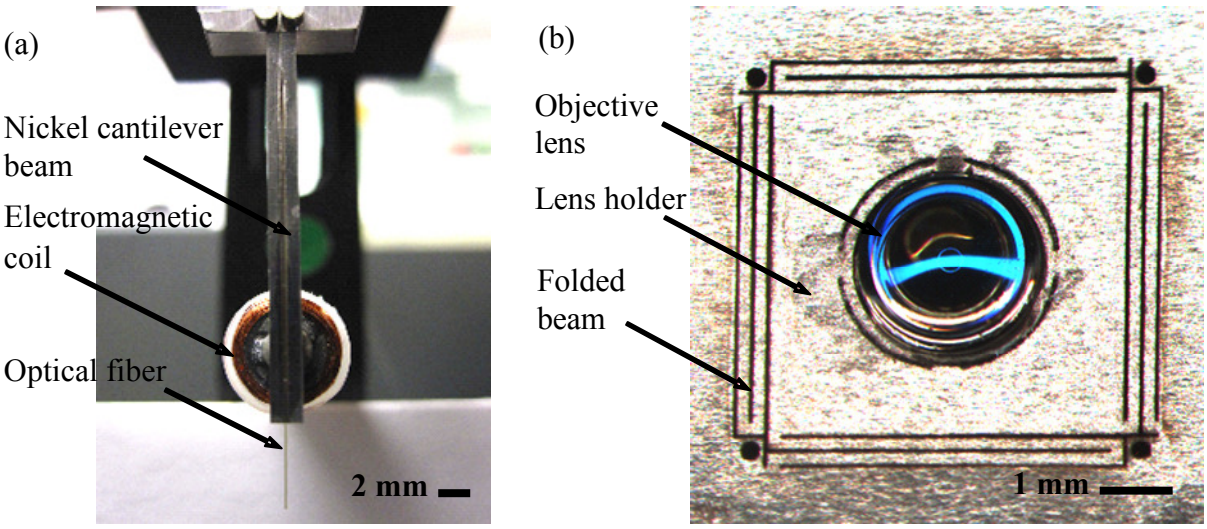

Figure 3.3 Photo of (a) Fiber optic actuator, and (b) Lens actuator, fabricated by laser micromachining of nickel foils.

The nickel foil used to fabricate cantilever beam for fiber actuation was 25.4 µm thick and the one used for lens actuator had thickness of 56 µm. Figure 3.3 shows a cantilever beam for fiber actuation and a flexure for lens actuation fabricated on nickel foils using a green laser.

Using laser can make the fabrication process much slower than electroplating techniques because the laser removes materials only at a small spot that it is focused at each time. However, the fabricated flexure can be more uniform in thickness which can result in more accurate theoretical prediction of actuation response of the lens. Figure 3.4 shows the cross-section view of the 2-axis scanner demonstrating the positions of the optical fiber, collimating and objective lenses and electromagnetic coils.

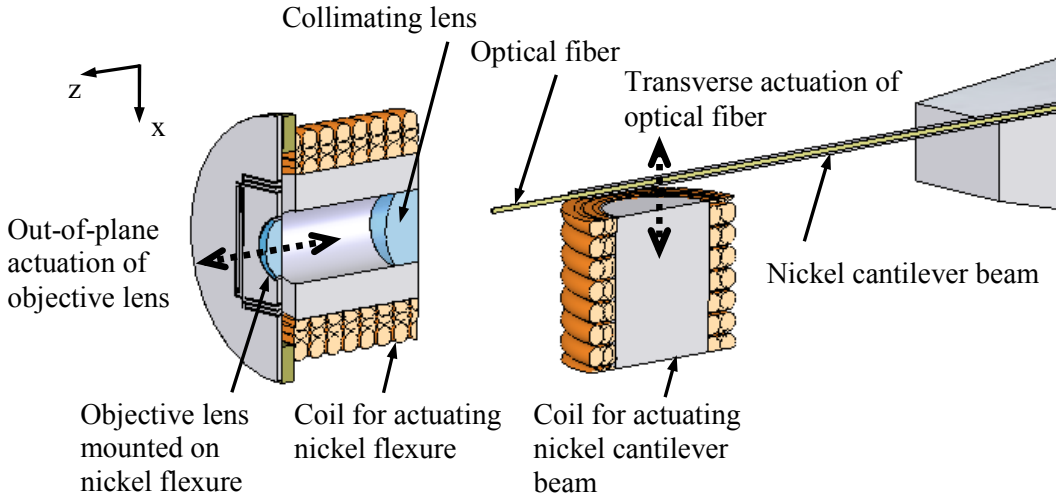

Figure 3.4 Cross-sectional drawing of 2-axis confocal scanner.

A larger objective lens can have better optical quality which enhances the resolution of image; however, the increased mass of larger lens reduces the resonant frequency of the lens actuator which lowers the imaging frame rate. In the current system, the resonant frequency of lens actuator is 378 Hz and the cantilever beam for fiber actuation is moving at 2 Hz. Fiber scanning frequency defines the imaging frame rate of 2 frames per second. Both lens and fiber actuators exhibit a sinusoidal response with peak-to-peak amplitudes of 190 μm and 450 μm respectively.

3.3.2 Mechanical Characterization

The frequency response of the nickel flexure before and after lens installation was predicted by performing FEA using COMSOL Multiphysics. This value was also calculated based on Eq. (2.9) and Eq. (2.12), and measured using an LDV. The FEA-predicted and calculated first mode resonant frequencies of the flexure were 564 Hz and 558 Hz before lens installation; and 401 Hz and 393 Hz after lens installation, respectively. The measured resonant frequencies of the lens actuator before and after lens installation were 549 Hz and 378 Hz respectively.

Figure 3.5 shows that the FEA analysis, calculation and LDV measurement agree well especially before lens installation. The measured resonant frequency after lens installation is lower than prediction. This is mainly due to the mass of the UV adhesive that was used to mount the lens to the flexure which was ignored in our calculations. Notably, the actuator's frequency bandwidth has increased after lens installation. This indicates lower quality factor, Q, and higher damping ratio, ζ, in the system compared to that before lens installation. Quality factor is defined by the equation $Q = \sqrt{kM} / c$, where k is the stiffness of the actuator, M is mass of the system and c is damping coefficient. Larger mass of the scanner after lens installation tends to increase the quality factor; however, increase in the damping coefficient dominates due to the fact that the scanner is installed on an electromagnetic coil which restricts air movement and causes increase in viscous damping after lens installation. Lower quality factor indicates higher rate of energy loss, which can be minimized by creating opening for air flow in the lens holder portion of the nickel flexure. The measured quality factors of the scanner before and after lens installation are 97 and 23 respectively. After the

lens installation, the maximum displacement of the flexure at the resonant frequency of 378 Hz was 190 µm.

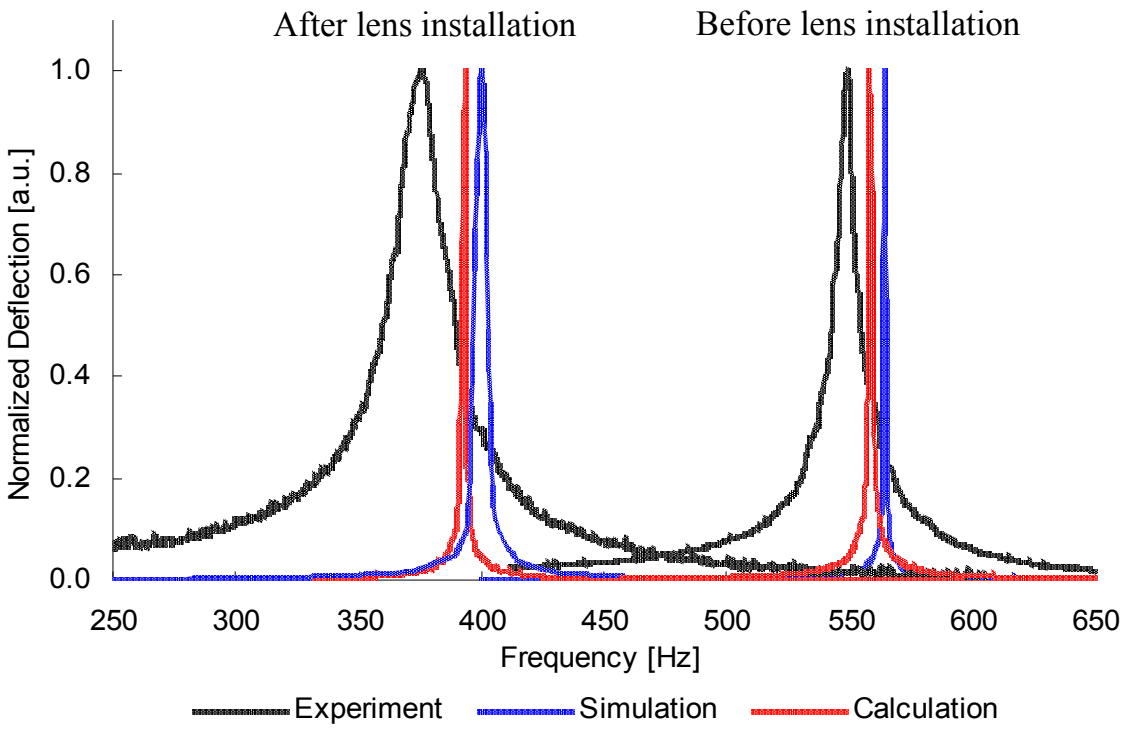

Figure 3.5 Measured, predicted and calculated resonant frequencies of the nickel flexure.

3.3.3 Optical Characterization

To evaluate the optical performance of the system, lateral and axial responses are determined by performing calculations, optical simulations, and experimental measurements. On-axis lateral resolution of the system was calculated by treating the fiber as a single point object and following analytical method described in [87]. This method emphasizes the sensitivity of system's lateral resolution to the size of detection pinhole, but neglects the size of illumination source. The estimated lateral resolution of the system based on this model is 0.92 µm. The theoretical on-axis axial response of the scanner was also determined by

applying analytical method described by Gu et al [88]. Fiber is considered as a detection pinhole and variation of detected intensity is plotted as a function of axial position as a perfect reflector is translated through focus. The FWHM of the intensity plot is the axial resolution which for our system is equal to 7.60 µm.

The optical performance of the system was predicted by Zemax optical simulation software (Radiant Zemax, LLC). Figure 3.6 illustrates a layout of the optical configuration. The SMF has a *NA* of 0.17 and mode field diameter (MFD) of 4 µm. The collimating and objective lenses are aspheric lenses with diameters of 3 mm and 2.4 mm, focal lengths of 4.5 mm and 1.45 mm, and numerical apertures of 0.30 and 0.55, respectively. Due to under-filling of the objective lens, the effective *NA* is 0.35. With the current lens selection, the system has a magnification of approximately 0.31 in transverse (X-axis) direction. As a result, when SMF is actuated ±225 µm, image size in the transverse direction is about 145 µm.

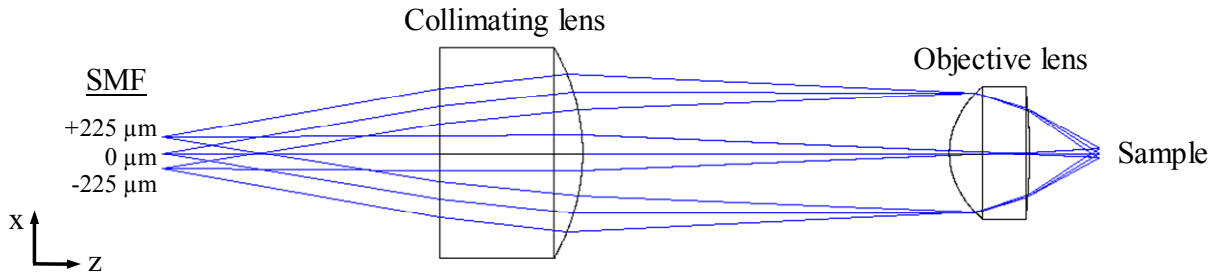

Figure 3.6 Two-dimensional layout of confocal scanner optical configuration.

Lateral resolution can be predicted from full field spot diagrams. Figure 3.7 represents beam spot sizes at the focal point of the objective lens corresponding to three fiber locations (0 µm and ±225 µm). Field points in each spot diagram (represented by red, blue and green colors) correspond to the center of fiber core ± 2 µm. Full field spot diagrams show that on-axis spot diameter is 1.2 µm while the spot size becomes larger (5.7 µm) at the edges of the FOV. In

addition the diagrams show that the propagated rays do not remain within the Airy disk (black circle shown on diagrams) when the fiber is at the edges of FOV. This means that the objective is not capable of providing diffraction-limited performance at these regions.

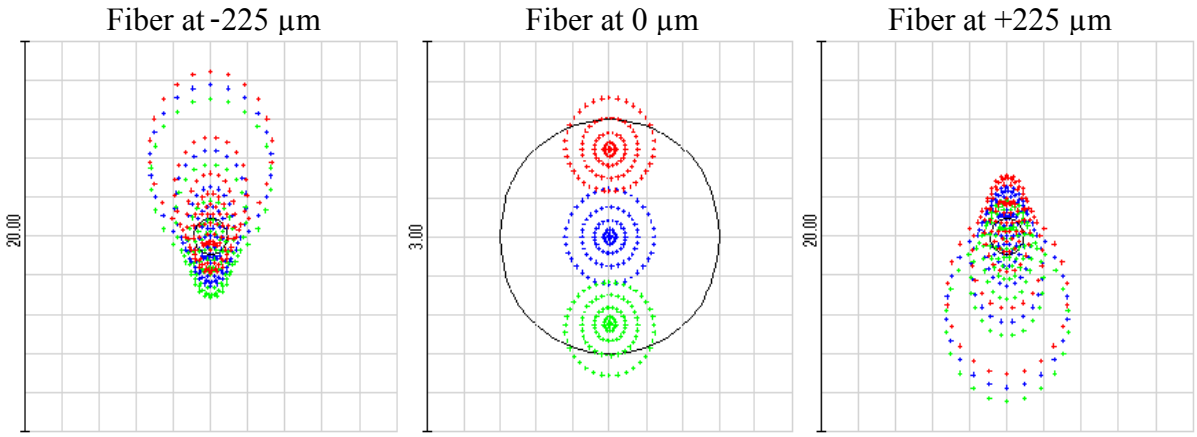

Full Field Spot Diagram

Airy Radius [µm]	0.9076		
Fiber position [µm]	+ 225	0	- 225
RMS Radius [µm]	2.847	0.600	2.847
GEO radius [µm]	8.482	1.071	8.482

Figure 3.7 Full field spot diagram of the confocal scanner demonstrating the lateral resolution.

This can also be seen in the modulation transfer functions (MTF) curves compared with the diffraction-limited curve (Figure 3.8). The plot indicates that the performance of the system is lower than the ideal case at the edges of scanning range which is mainly due to the geometrical arrangements and imperfections of the lenses.

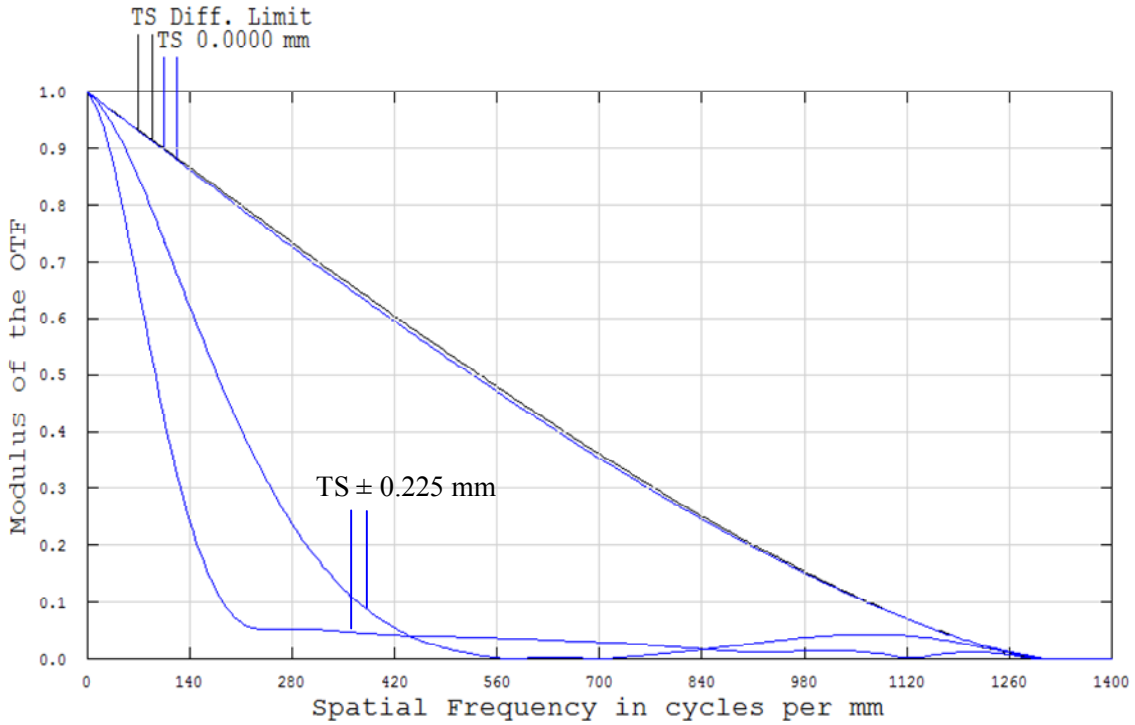

Figure 3.8 Plot of MTF for three fiber positions. OTF: optical transfer function, T: Tangential, S: Sagittal.

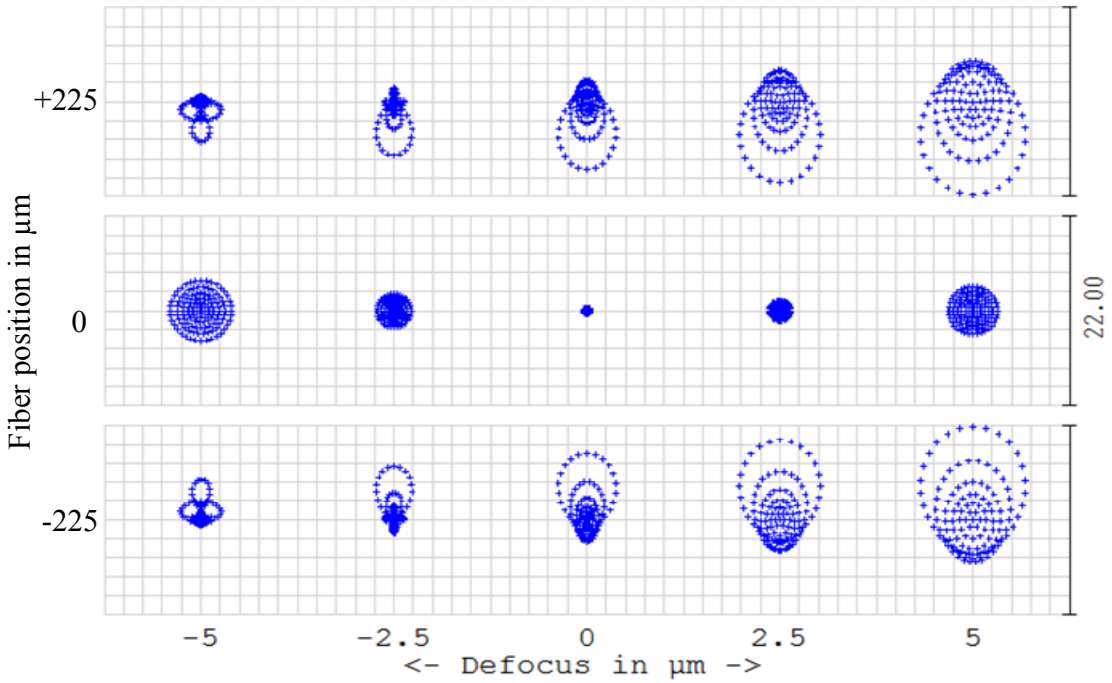

Figure 3.9 Through focus spot diagram of 2-axis confocal scanner at three fiber positions.

The axial response of the scanner can be assessed from the through focus spot diagrams by ray trace analysis at three fiber positions. Figure 3.9 shows the spot diagrams at various focal plane shifts, indicating how the spot size diameter changes at various distances from the focal point. From Gaussian beam propagation analysis, the depth of focus is defined as twice the Rayleigh range of the beam and is equal to 3.26 µm in our system.

On-axis lateral and axial resolutions were also measured by experiment. The lateral resolution is defined as 0.78 times the 10–90% (1/e^2 resolution measurement) of the intensity signal from laterally scanning edge of a surgical blade by actuating the optical fiber while holding the objective lens stationary. Axial resolution can be approximated by measuring FWHM of the intensity signal when a flat mirror is axially scanned [89] by the lens while the fiber was fixed at 0 µm displacement position. The experimental lateral and axial resolutions were 3.87 µm and 10.68 µm respectively (Figure 3.10).

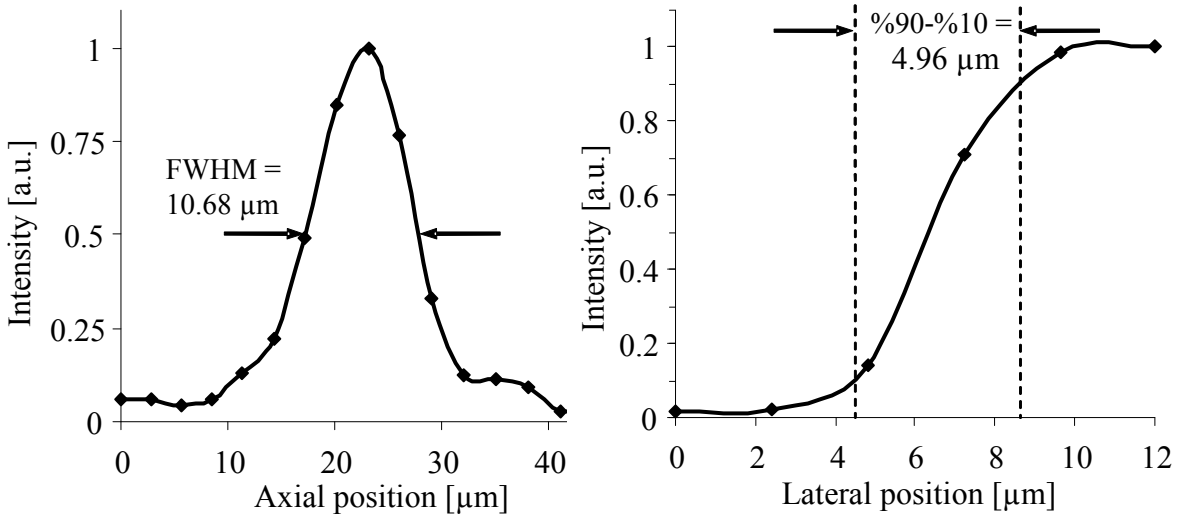

Figure 3.10 Experimental measurement of (a) Axial and (b) Lateral resolutions of 2-axis confocal scanner.

Predicted values for lateral and axial resolutions are smaller than experimental results. We believe this is mainly due to the imperfect alignment of optical components and measurement samples. Both lateral and axial resolution measurements were performed by holding a blade-edge and a flat mirror stationary while actuating the optical fiber and objective lens respectively. In lateral resolution measurement, the distance between blade-edge and optical axis can significantly affect the measurement since off-axis spot size is larger than on-axis spot diameter. In addition, axial resolution measurement is sensitive to the axial and lateral misalignment of the optical fiber [90, 91] during the system assembly.

3.4 Imaging Results

Confocal scanner was used to obtain vertical cross-sectional images of samples. The lens was actuated 190 μm at 376 Hz while sampling 200 intensity data points over one actuation cycle and fiber was moved at 2 Hz, providing a 145 μm scan in transverse direction, while collecting 189 data points in each cycle. The intensity data was used to graph vertical section view of samples. Figure 3.11(a) shows a confocal image obtained from a SU-8 PR (MicroChem Corp.) channel fabricated on a Si substrate. The width and height of the channel are 90 μm and 65 μm respectively. Figure 3.11(b) is the optical profile image of this channel obtained by Wyko optical profiler (Veeco Instruments Inc.) for comparison. In the confocal image, the vertical walls of SU-8 channel are not visible. This may be due to the large incident angle of illumination beam with respect to the surface of the walls and total reflection which prevents the light from going back to the optical fiber for confocal imaging. However, this image shows that the scanner is capable of detecting surfaces and edges of the samples cross-section for defining shape and dimensions of the channel.

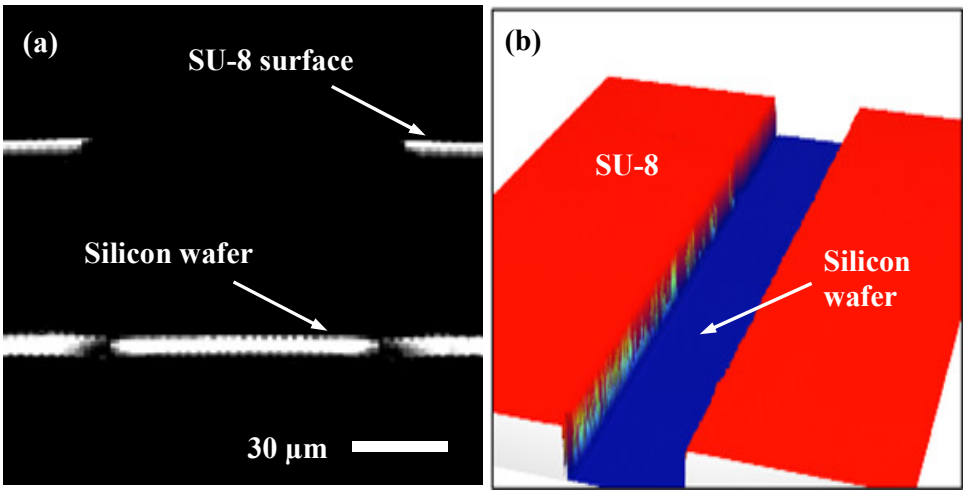

Figure 3.11 (a) Confocal image of SU-8 channel cross-section. (b) Optical profile of the channel measured by an optical profiler.

Figure 3.12(a) shows a microscopic transverse cross-sectional image of a yellow onion stained with Alcian blue. Depending on the size of onion, the cross-sectional shape and dimensions of epidermal cells are different. The typical cross-sectional size of the epidermal cells of the sample onion used in our experiment was about 40 µm by 40 µm. The epidermal peel was removed from the onion for conducting confocal imaging experiments. Fig. 12(b, c, and d) show three confocal vertical optical section images of the onion peel. The images clearly show the upper and lower surfaces of the peel layer. The images also provide information regarding the position of the walls and size of the cells.

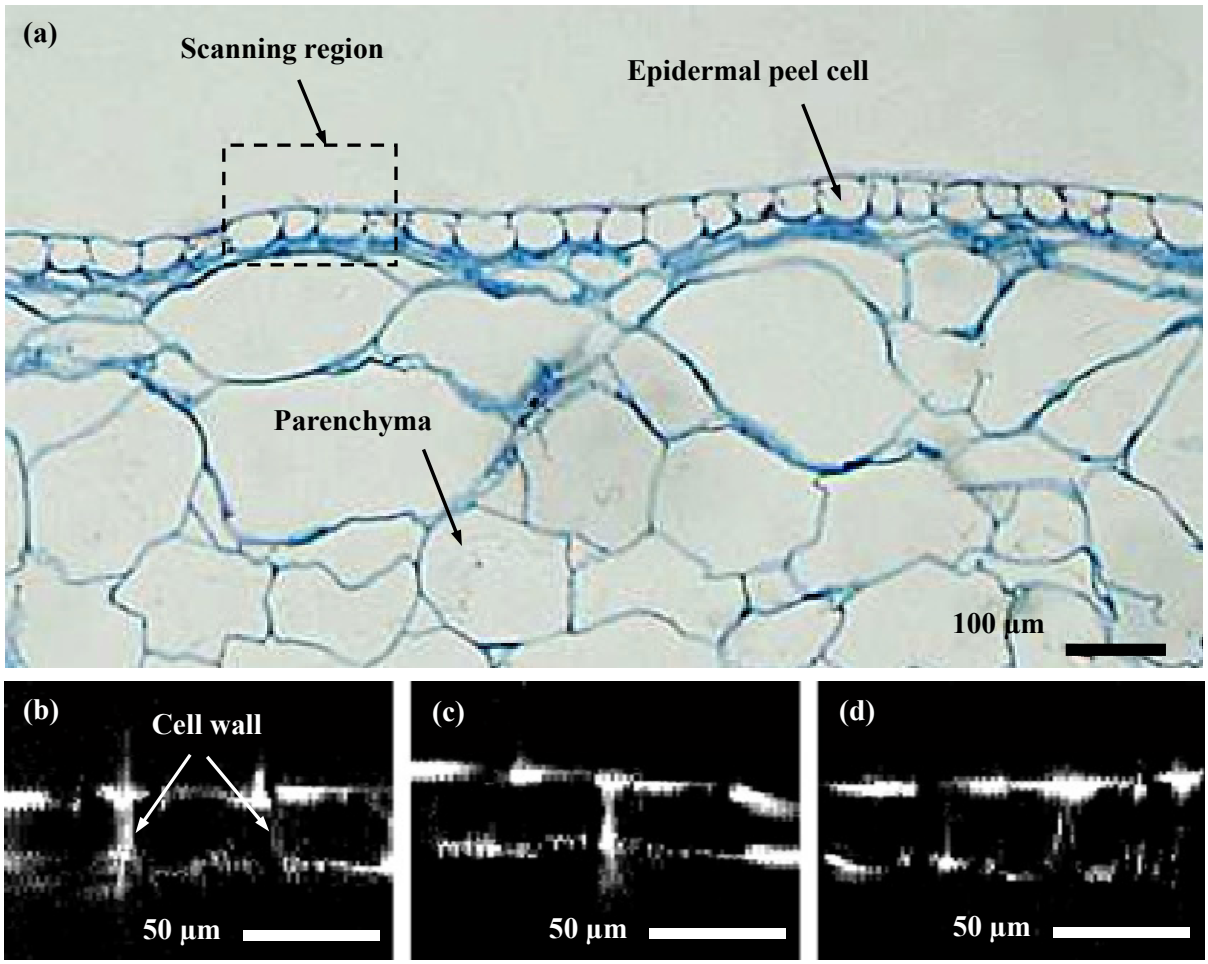

Figure 3.12 (a) Microscopic image of an onion transverse section stained with Alcian blue. (b, c, and d) Confocal vertical optical section images of onion epidermis.

3.5 Concluding Remarks

The confocal scanner developed in this chapter provides the advantage of direct vertical optical sectioning of samples. This possesses great potential for clinical applications for performing vertical sectioning optical biopsies that mimic conventional histopathology examinations. FOV of the scanner is 145 µm in transverse and 190 µm in axial directions. The lateral and axial resolutions are 3.87 µm and 10.68 µm respectively. The current system demonstrates the functionality of the optical configuration and scanning mechanisms;

however, the system has to be optically and mechanically optimized to expand FOV and enhance the image quality and resolution.

CHAPTER 4

A HANDHELD FIBER OPTIC RASTER SCANNER FOR HORIZONTAL OPTICAL SECTIONING OF BIOLOGICAL TISSUES[3]

4.1 Introduction

Fiber-based confocal scanners utilize a fiber bundle or a single fiber for light transmission. In recent years, various proximal and distal scanning mechanisms and imaging embodiments have been developed [92]. A proximal scanning fiber bundle-based endomicroscope has been commercialized by Mauna Kea Technologies (Paris, France) [93]. Another commercially

---

[3] A version of this chapter has been published in a journal and presented in a conference:

- **Mansoor, H.**, Zeng, H., Tai, I. T., Zhao, J., and Chiao, M. (2012) "A Handheld Electromagnetically Actuated Fiber Optic Raster Scanner for reflectance Confocal Imaging of Biological tissues" IEEE Transactions on Biomedical Engineering, In Press.

- **Mansoor, H.**, Zeng, H., Tai, I. T., Zhao, J., and Chiao, M. (2013) "A miniature fiber-optic raster scanner for 2D optical imaging of biological tissue" 26th IEEE International Conference on MEMS, Taipei, Taiwan, 137 – 140.

available flexible endoscope is based on distal scanning of a single fiber (Pentax Corporation, Tokyo, Japan) [94].

The essential component in an imaging system is a mechanism for scanning a laser beam relative to a sample. Scanning of a sample is typically achieved by moving stages [95, 96] or by scanning the laser beam using mirrors [74, 97-102], lenses [28, 103, 104] or optical fibers [33, 39, 105-117]. Moving stage is a simple way of confocal imaging across a sample; however, this method is limited by scanning speed and also not suitable for *in vivo* tissue imaging. Mirror scanners including galvo mirror and micromirror scanners can be fast and achieve large scanning range, but may be challenging in miniaturization and alignment since optical axis is folded after reflecting off mirror surface. Transmissive scanners using moving lenses have alignment advantages for systems implementation, but scanning speed can be limited by the mass of the lens. On the other hand, ease of optical alignment along with fast scanning speed and large actuation range make optical fiber scanners suitable for miniaturization for clinical applications.

Several research groups have demonstrated fiber optic scanners utilizing piezoelectric and electromagnetic actuation mechanisms. Various two-dimensional scanning patterns including Lissajous, spiral and raster have been demonstrated. Lissajous patterns are created by actuating an optical fiber in two axes (X and Y) at its resonant frequencies while controlling the amplitude and phase of scan in each direction. When amplitude of driving signals is triangularly modulated, a spiral scanning pattern can be generated. For raster scan, optical fiber is actuated at its resonant frequency in one axis while moved at a lower non-resonant frequency in the other axis. In general, miniaturization of Lissajous and spiral fiber scanners is easier since resonant actuation requires smaller driving voltage and excitation force. In

raster scanners, the off-resonance slow actuation of fiber requires a large driving force which is particularly difficult to generate using miniature electromagnetic actuators. All described scanning patterns have been previously demonstrated using piezoelectric actuation mechanism. Electromagnetic actuation has also been used to generate spiral scanning patterns. Recently, a group has proposed raster scanning of an optical fiber using electromagnetic fields [118].

In this chapter we present a fully-packaged hand-held laser beam raster scanner for two-dimensional reflectance-mode confocal microscopy of biological tissues. Magnetically driven fiber optic actuators are incorporated in the scanning head to move an optical fiber in a raster scanning pattern. Raster scanning pattern has been selected because of its uniformity and simple image reconstruction. Unique design of electromagnetic actuators in our system enables achieving large fiber deflections for both fast and slow scanning axis (≥500 μm) while requiring low driving currents (≤200 mA).

4.2 Materials and Methods

4.2.1 Instrumentation

A schematic of the optical system is shown in Figure 4.1. A 785 nm laser diode (Starbright 785XM, Torsana Laser Technologies) with linearly (vertically) polarized output power of 500 mW was used as a light source. Laser beam power was controlled using a variable metallic neutral density (ND) filter. The laser beam was directed to a single-mode fiber coupler by a polarizing beamsplitter (PBS) and coupled to a polarization maintaining (PM) optical fiber (Fibercore HB750) with the mode field diameter (MFD) of 4 μm,, for delivery to the confocal scanner. At the distal end of the PM fiber, light has the same polarization

state as the incoming beam. The light beam is then collimated by a lens and circularly polarized by a zero-order quarter wave plate. This may be done by orienting the fast (or slow) axis of the wave plate at 45º to the linearly polarized incident light.

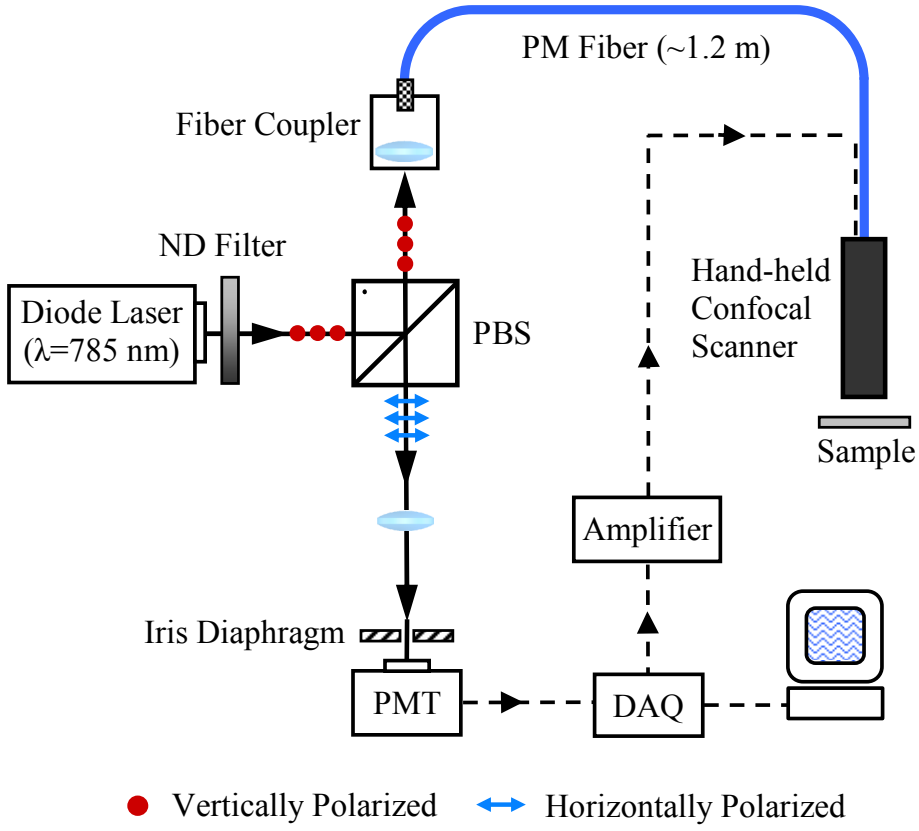

Figure 4.1 Schematic diagram of imaging system.

After focusing into the sample by an objective lens, the light is scattered. Single scattered photons from the sample retain their polarization state. After passing through the quarter wave plate, these photons are linearly (horizontally) polarized and have rotated 90º with respect to the incident light before coupling back into the PM fiber. Multiple scattered photons from the sample behave as un-polarized or partially polarized light. Figure 4.2 shows the optical configuration at the scanning head of our confocal scanner.

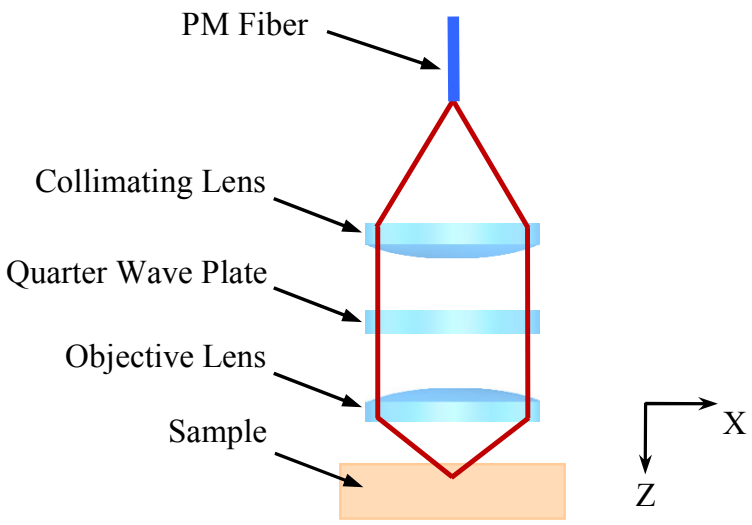

Figure 4.2 Optical configuration of confocal scanning system.

The horizontally polarized light coming back from the PM fiber, originated from single scattering photons in the sample, can pass through the PBS toward a photomultiplier tube (PMT). The PBS blocks the vertical polarization components of multiple scattered photons from the tissue and also the unwanted light reflections from the surfaces of optical components. Using light polarization effects can greatly improve imaging quality and contrast [119]. An iris diaphragm is used to block the PMT from detecting the ambient light. The intensity signal from the PMT is collected by a DAQ card for image reconstruction. The DAQ card is also used to generate driving signals to drive the scanner and control frame rate and scanning range of the imaging system. Both collimating (Geltech 352220) and objective (Geltech 352230) lenses are aspheric lenses with effective focal lengths (EFL) of 11 mm and 4.51 mm respectively. Diameter of the light beam depends on the *NA* of the optical fiber and collimating lens; and may not be large enough to fully cover clear aperture of objective lens. As a result, the effective *NA* of the system may be less than the full *NA* of objective lens. In our system effective *NA* is 0.29 with a magnification of 0.41 in the transverse direction. This

means that the scanning range of the focal spot is 0.41 times the actuation range of the PM fiber in X and Y directions.

4.2.2 Scanner Design

Schematic of fiber optic raster scanner is shown in Figure 4.3 (a). It consists of a PM fiber; two cantilever beams (B1 and B2) and two electromagnetic coils (C1 and C2).

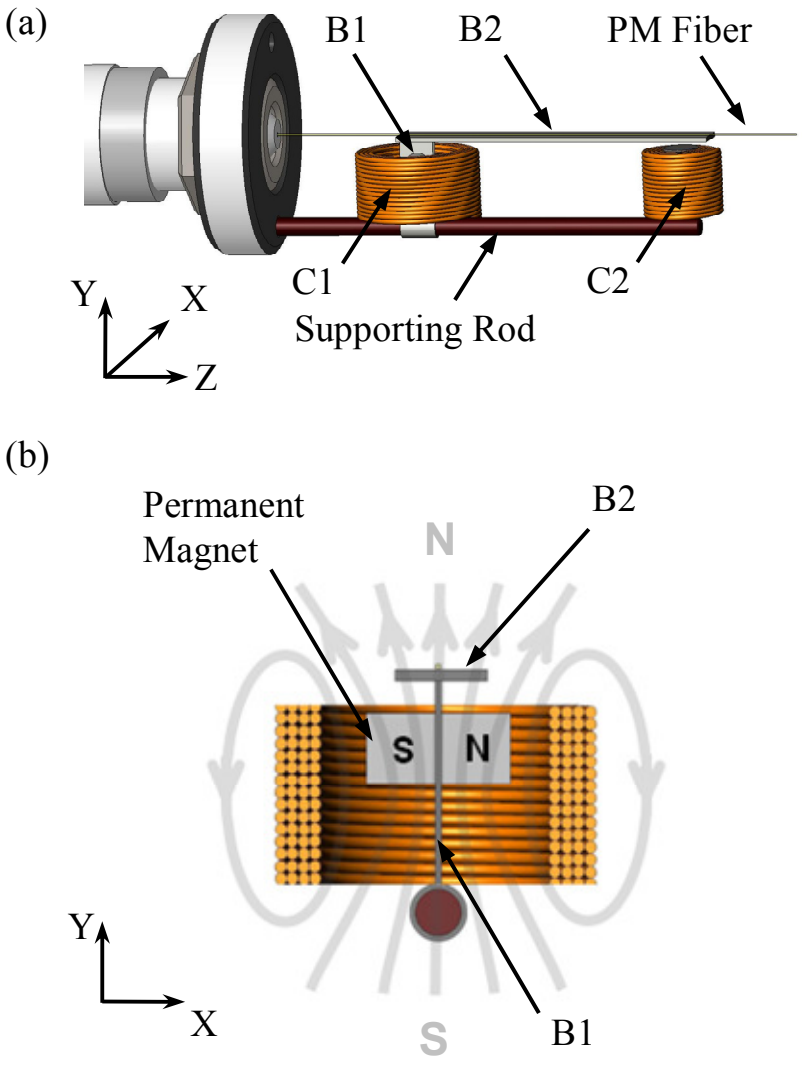

Figure 4.3 (a) Schematic of the two-axis fiber optic scanning system and (b) schematics of electromagnetic actuation mechanism for X-axis scanning.

Both beams are fabricated by laser micromachining of nickel foils using a commercial laser machining system (New Wave Research QuikLaze system). B1 is soldered to a supporting rod and is compliant in bending in X direction. Using UV curable adhesive (Norland Optical Adhesive 63), PM fiber is mounted onto B2 that is perpendicularly soldered to B1 and is flexible in Y direction. Beam B1 is 2 mm wide and 4.5 mm long and has thickness of 0.05 mm. Two neodymium permanent magnets are placed on both sides of B1 and a hollow-core coil (C1) is placed around it (Figure 4.3(b)). Beam B2 is 2.4 mm wide, 12 mm long and 0.11 mm thick. Coil C2 is positioned under the free end of B2. B1 and B2 have first mode resonant frequencies at 11 Hz and 648 Hz respectively.

One scanning mode is realized by moving PM fiber in the Y direction by bending B2 about the X-axis. For this, an AC current is applied to C2 to generate a magnetic field. Magnetic domains of the ferromagnetic nickel are then aligned with the applied field and nickel is magnetized. As a result, beam B2 is attracted toward the magnetic field and therefore the PM fiber starts to move in the Y direction.

The second scanning mode is produced by translating the PM fiber and B2 in the X direction when B1 is bent about the Z-axis. This is achieved by applying a current to C1 that creates opposite magnetic poles on top and at bottom of the coil (Figure 4.3(b)). The magnetic poles attract permanent magnets and create a moment that causes B1 to bend in the X direction. Since B1 and B2 have much higher bending and twisting stiffness in all directions other than the intended ones (i.e. X-axis for B1 and Y-axis for B2), very little imaging artifacts due to cross-axis motion of the PM fiber in the two scanning mode is expected.

The 2-axis fiber actuator along with lenses and wave plate were assembled in standard half-inch lens tubes (17.8 mm outer diameter). A schematic diagram of the handheld imaging system is shown in Figure 4.4(a). Figure 4.4(b) shows a photograph of fabricated fiber scanner before inserting into lens tubes. Lenses and wave plate are positioned and secured in place by retaining rings. An adjustable lens tube is used to align PM fiber with collimating lens. The length of the scanning head is 57 mm. Figure 4.4(c) is a photograph of the hand-held confocal system after final assembly.

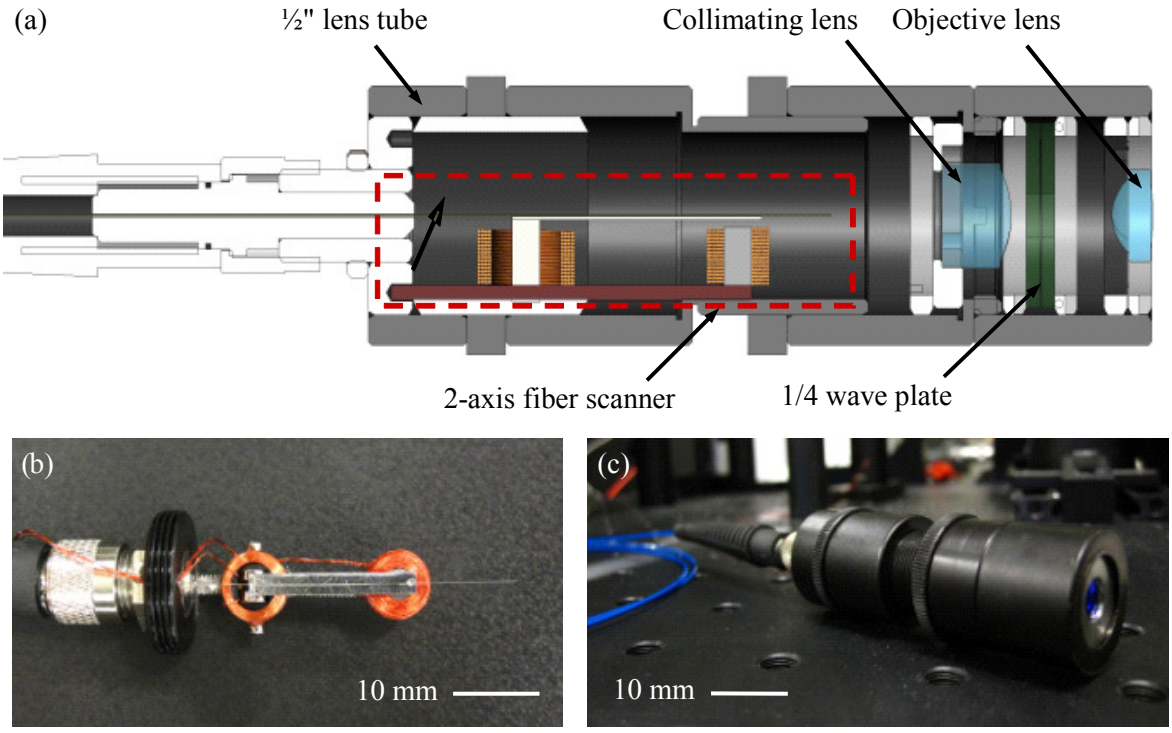

Figure 4.4 (a) Cross-sectional drawing of handheld confocal imaging system and photographs of (b) 2-axis fiber raster scanner and (c) fully assembled system in lens tube.

4.3 Optical Performance

4.3.1 Simulation

MTF of a confocal system represents the expected contrast and resolution at a given spatial frequency [120]. Figure 4.5(a) and Figure 4.5(b) show on-axis and 120 μm off the optical axis MTFs of our confocal system along with MTF curve for a perfect diffraction limited lens generated by Zemax optical simulation software (Radiant Zemax, LLC). Each plot includes curves for three field points. One field point is on the optical axis (0 μm) and the other two are set to ± 2 μm to simulate the MFD of the optical fiber. The vertical axis represents the image contrast and the horizontal axis is the spatial frequency in cycles per mm (or line pair per mm (lp/mm)). Spatial resolution of the system is defined from the spatial frequency where contrast is 10% of its maximum value. At 10% contrast, the on-axis and off-axis spatial frequencies are about 815 and 770 lp/mm. This corresponds to on-axis and off-axis resolutions of 0.61 μm and 0.65 μm.

Performance of the system in the axial direction can be assessed by the depth of focus that is two times the Rayleigh range. Figure 4.6 shows plot of beam profile when focused by the objective lens, according to Eq. (4.1) [121]:

$$w(z) = w_0 \sqrt{1 + \left(\frac{z}{z_R} \right)^2} \tag{4.1}$$

where w_0 is the beam waist radius, z is relative axial position and z_R is the Rayleigh range that can be calculated from the beam waist and wavelength (λ) of the laser beam:

$$z_R = \frac{\pi w_0^{\,2}}{\lambda} \tag{4.2}$$

In our system the beam waist is 0.78 µm and Rayleigh range is 2.46 µm. This will give depth of focus of 4.92 µm.

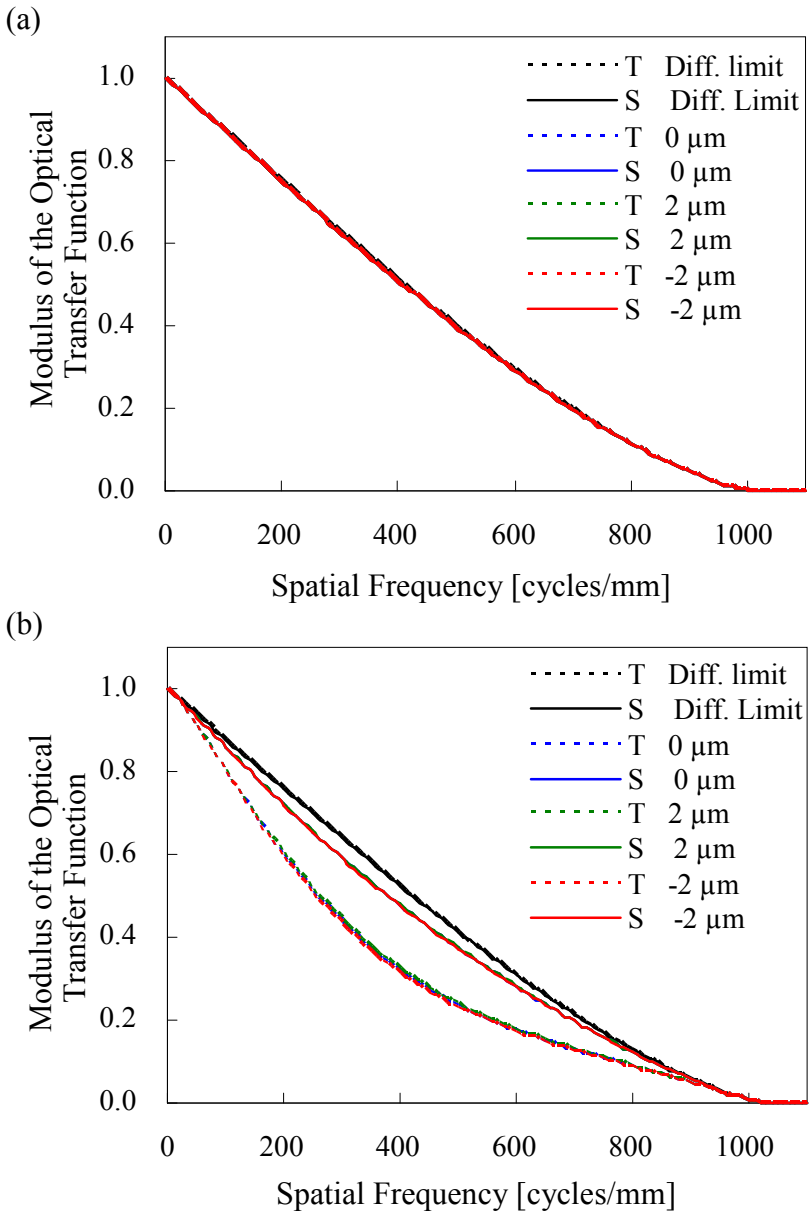

Figure 4.5 Plot of MTF for (a) center and (b) 120 µm off the optical axis. T: Tangential, S: Sagittal.

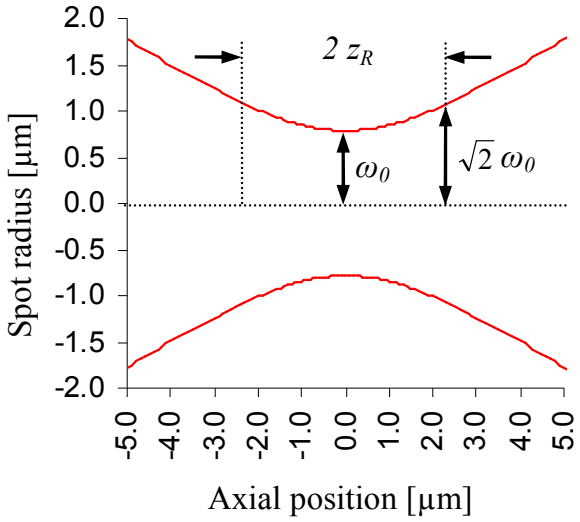

Figure 4.6 Plot of laser beam profile at the focal point of the objective lens.

4.3.2 Imaging Resolution

Lateral resolution for a Gaussian spot may be defined as its full width at half maximum (FWHM) intensity signal. Experimentally, lateral resolution can be measured by translating a sharp edge across a beam while recording the beam intensity at various lateral positions of the sharp edge. FWHM lateral resolution can be calculated according to [122]:

$$R_{lateral} = 0.94(X_{10-90}) \tag{4.3}$$

where $X_{10\text{-}90}$ is the lateral movement of the sharp edge between the points at which the intensity is 10% and 90% of its maximum value. The lateral resolution of our device was characterized by scanning a high precision Ronchi ruling glass target with 50 lp/mm. Figure 4.7(a) shows a photo of Ronchi ruling target, with line width of 10 µm. Figure 4.7(b) shows the intensity profile obtained by scanning across the lines of target. Figure 4.7(c) is zoomed-in view of the intensity signals for scanning across the FOV.

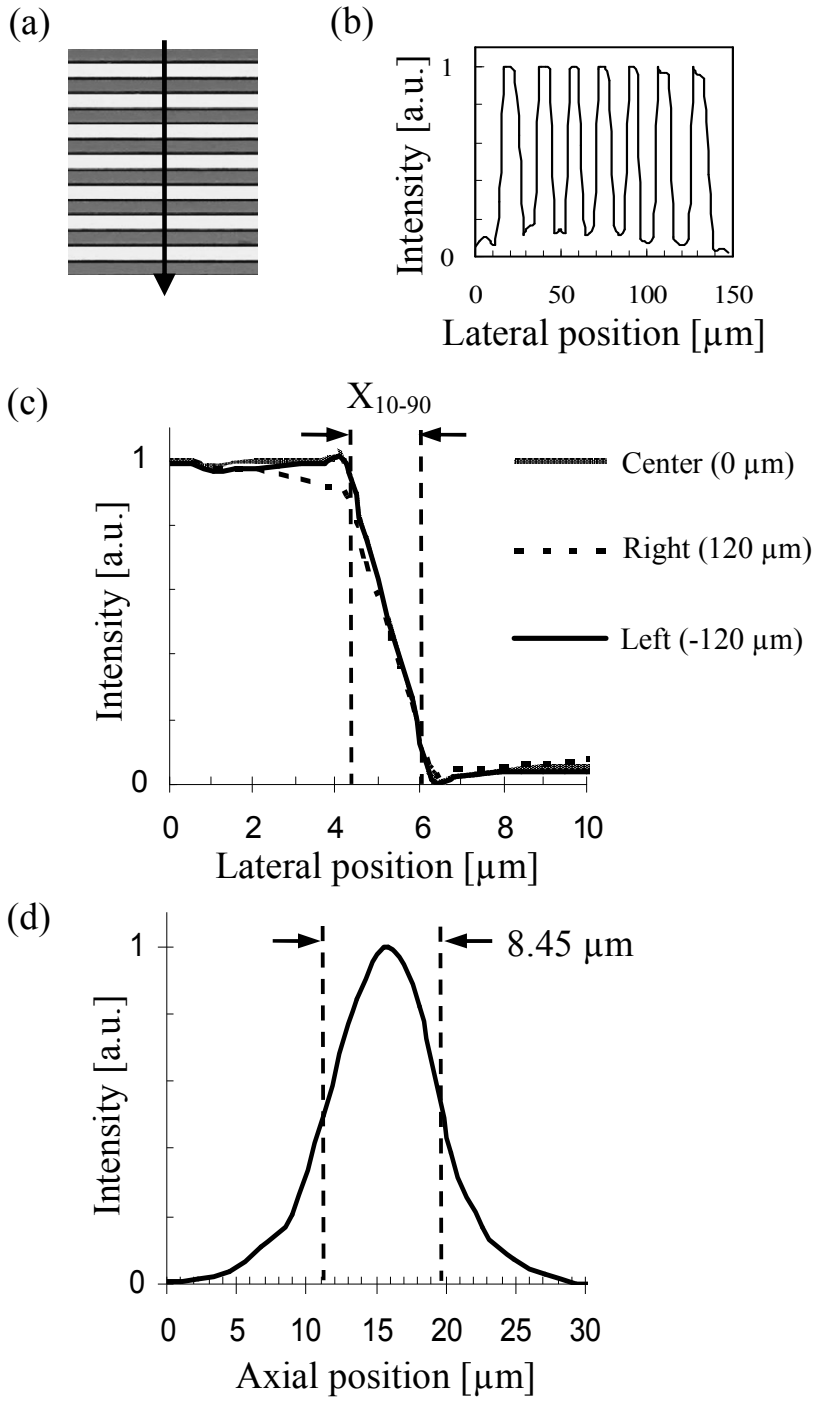

Figure 4.7 (a) Optical image of high precision Ronchi ruling target with 50 lp/mm, (b) intensity profile obtained by scanning across the lines of the target, (c) zoomed-in view of the intensity profiles from scanning at the center, right and left of FOV, and (d) intensity profile from axial scanning of a flat mirror for axial resolution measurement.

The on-axis lateral resolution (at the center of scanning area) was determined to be 1.41 μm. Resolution is lower at the edges of FOV. The overall average lateral resolution of the system is 1.55 μm. Axial resolution can also be experimentally measured from an intensity signal that is obtained from axial scanning of a flat mirror (Figure 4.7(d)). Full width at half maximum of the intensity graph defines the axial resolution. For our system this value was 8.45 μm.

4.4 Imaging Experiments

Raster scanning of the laser beam has been achieved by actuating B2 at its first mode resonant frequency of 648 Hz and B1 at lower frequency of 2 to 3 Hz. Driving signal to coil C2 was a sinusoidal current with root mean square (RMS) value of about 50 mA and DC bias of 80 mA. B1 was actuated by applying a 60 mA AC current with no DC bias to coil C1. The intensity signal from the PMT was collected by the DAQ card and converted to images by MATLAB. Number of pixels in the X direction of the reconstructed image was limited by the frequency ratio of fast and slow scanning directions. Number of pixels in the Y direction was also limited by the speed of the DAQ card used in our system. Imaging was performed on both sides of the slow-axis and as a result, frame rate of the scanner is double the slow-axis frequency.

To show the functionality of our system, we conducted imaging experiments on a fruit fly wing and a fixed human colon tissue sample. For human tissue experiment, approval has been obtained from the University of British Columbia Research Ethics Board (H10-01363). During imaging experiments, the probe was held stationary and the specimens were positioned at the working distance of scanner (2.92 mm from the surface of the objective

lens) using a manual micro-stage. Figure 4.8(a) and Figure 4.8(b) compare images obtained from the fly wing's posterior margin using our confocal scanner and an optical microscope.

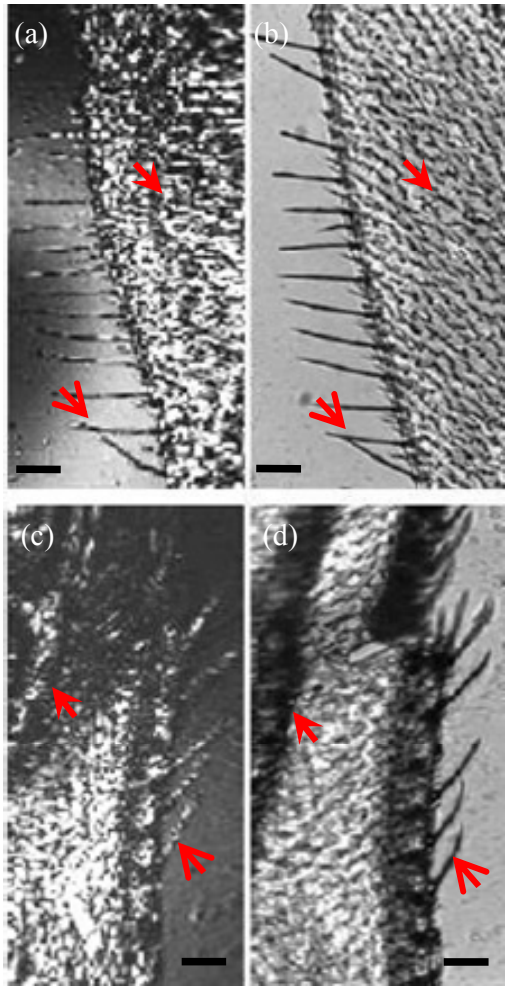

Figure 4.8 (a) Confocal image of posterior margin of a fruit fly wing compared to (b) a photo of same region obtained by an optical microscope; (c) confocal image and (d) optical microscopic photo of wing's costal margin. Confocal images are obtained at speed of 6 frames per second. Image size is 120 µm by 240 µm with 108 by 192 pixels. Scale bars are 20 µm.

In both images small hairs that cover the wing (stealth arrows) and longer hairs along the edge of the wing (open arrows) are visible. Figure 4.8(c) and Figure 4.8(d) are confocal and optical images from the fly wing's costal margin showing longitudinal veins and branches

(stealth arrows) and hairs grown on the veins (open arrows). Figure 4.9(a) and Figure 4.9(b) compare a confocal image and an H&E histology image of a healthy human colon tissue sample. The confocal image shows a good cellular level resolution and contrast. The two images may not come from the same location inside the sample, but showing similar, typical morphology structures of normal human colon mucosa. For example, in normal tissue crypt lumens are shown as larger circular areas (open arrow) and goblet cells are seen as low-scattering smaller areas (stealth arrows).

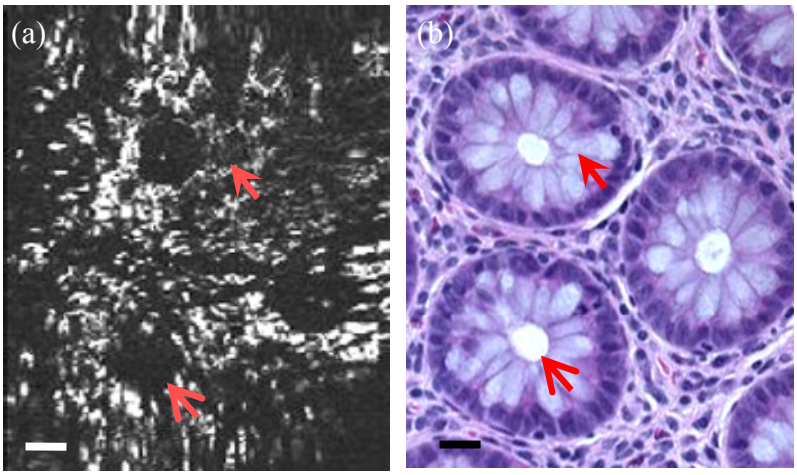

Figure 4.9 (a) Confocal image of an excised normal human colon tissue preserved in a 10% neutral buffered formalin compared to the (b) H&E image of the same tissue sample after standard histology processing. Confocal image is obtained at the speed of 4 frames per second. Image size is 200 µm by 240 µm with 162 and 192 pixels in each direction. Imaging depth is approximately 10-15 µm. Scale bars are 20 µm.

4.5 Summary and Discussion

Table 4-1 summarizes characteristics of some piezoelectric and electromagnetic fiber optic scanners. Electromagnetic actuators require low driving voltages but may consume relatively high electrical power due to requirements for large driving currents. Power consumption in our scanner was estimated to be 168 mW when driving both scanning axes. Disadvantages of magnetic actuators are relatively low force output and significant drop in magnetic forces after miniaturization, which brings challenges in achieving large displacements [123]. Piezoelectric fiber scanners are fabricated by attaching an optical fiber on a cantilever bimorph or tubular piezoelectric actuators. These types of fiber optic actuators can be faster and provide higher scanning rates, but their scanning area is typically limited by smaller displacement of piezoelectric actuation. Operating voltage for these actuators is typically high; however, electrical power consumption is usually lower than electromagnetic actuators due to small driving currents.

The most favorable two dimensional laser scanning pattern is raster; however, generating this pattern in miniaturized scanners is a challenge [124]. Alternatives to the raster are spiral and Lissajous scanning patterns, in which actuation in both axes are performed at mechanical resonant frequencies. Spiral scanners can potentially take full advantage of available clear aperture of lens system, but their sampling density is much lower in the peripheral regions of FOV. The main advantage of Lissajous scanning pattern is that it can be generated using narrow-band actuation signals without exciting unwanted dynamics of the scanner [125]. But Lissajous patterns may have non-uniform sampling distances and tend to oversample on the edges of the FOV, which could potentially reduce dynamic range of imaging signal.

In our current system, confocal images are produced from both scanning sides of the slow axis and only one side of the fast axis. Images with higher pixel resolution can be constructed by using both scanning sides of fast axis; however, artifacts due to zig-zag motion of fiber may be induced to the image that reduces lateral resolution. While imaging on only one side of fast axis, an image artifact in a form of wavy patterns was observed in the preliminary imaging experiments. The cause of this image artifact was investigated and correction methods were proposed (see Appendix B for details).

Actuation mechanism	Actuator shape	Scanning pattern	Mechanical Scanning	Actuator dimension	Scanning rate	Driving signal	Driving power	Reference
Piezoelectric	Piezo tube	Line	~ 2.5 mm	Total length: ~ 15.7 mm Diameter: 1.5 mm	1.4 kHz	60 V	~ 4 mW	[110]
	Cantilever bimorph	Line	~ 2 mm	Total length: 76 mm Width: 6.4 mm	< 100 Hz	300 V	Not specified	[111]
	Piezo tube	Spiral	± 0.4 mm	Total length: 6.3 mm Diameter: 0.45 mm	11 kHz	40 V	5.5 mW	[109]
	Two cantilever bimorphs	Raster	0.65 by 1.0 mm	Total Length: 26 mm Width/thickness: 1 mm	~ 1.1 kHz & 4 Hz	Total ~ 250 V	Total ~ 0.65 mW	[106]
	Square piezo tube	Raster	0.19 by 0.19 mm	Total length: 283 mm Width: ~ 3.5 mm	~ 879 Hz & 3 Hz	Total ~ 175 V	Not specified	[112]
	Cantilever bimorph	Lissajous	1.0 by 0.8 mm	Total length: ~ 75 mm Width/thickness: 2.2 by 0.7 mm	~ 383 Hz & 236 Hz	1.5 V	Not specified	[108]
Electromagnetic	Ferromagnetic coating on fiber	Line	~ 0.89 mm	Fiber length: 52 mm Coating length: ~ 5-7 mm	~ 28 Hz	0.26 A	Not specified	[113]
	Iron bead on fiber	Line	~ 4 mm	Fiber length: 50 mm Iron bead diameter: 1 mm	~ 30 Hz	0.12 A	Not specified	[32]
	Stainless steel tube	Spiral	~ 3.46 mm (resonant)	Length: 40 mm Diameter: 0.5 mm	131 Hz	0.35 A	Not specified	[117]
	Iron bead on fiber	Spiral	~ 3 mm	Fiber length: 50 mm	~ 29 Hz	~ 0.2 A	Not specified	[33]
	Magnet mounted on fiber	Raster	~ 0.5 by 0.5 mm	Total fiber length: 24 mm Magnet length: 2 mm	~ 850 Hz	Not specified	Not specified	[118]
	Fiber on ferromagnetic beam	Raster	~ 0.4 by 0.6 mm	Total length: 22 mm Width/thickness: 4.5 by 2.5 mm	~ 648 Hz & 3 Hz	Total ~ 0.19 A	Total ~ 168 mW	Our system

Table 4-1 Summary of selected piezoelectric and electromagnetic fiber optic scanners

4.6 Concluding Remarks

A hand-held magnetically actuated fiber optic raster scanner for two-dimensional confocal imaging of biological samples has been demonstrated. The scanner is assembled in standard half-inch lens tubes and has rigid length of 57 mm. Scanning speed of device is 6 frames per second with optical resolutions of 8.45 μm and 1.55 μm in the axial and transverse directions. Imaging capability of the system was demonstrated by imaging a fly wing and a human colon tissue sample. The device described in this chapter has several advantages that makes it attractive for further development. Raster scanning pattern of the device provides large scanning area with more uniform sampling compared to spiral and Lissajous scanning patterns. The scanner is driven by electromagnetic forces only, hence provides large scanning range and requires low driving voltages that are desired in clinical applications. Optical configuration and mechanical design of the scanning head provides easy optical alignment and replacement of components. The confocal scanner design can be combined with an out-of-plane lens actuator for three-dimensional imaging. The hand-held device described in this chapter was primarily developed to facilitate non-invasive clinical diagnosis and evaluation of diseases such as skin and oral cancers; however, this device may be further miniaturized to form a catheter for endoscopic applications.

CHAPTER 5

CONCLUSIONS AND FUTURE WORKS

5.1 Summary

This thesis included chapters on optical imaging technologies, MEMS fabrication processes, electromagnetic actuators for lens and optical fiber scanners and development of reflectance confocal imaging devices for thickness measurement and real-time optical sectioning imaging of samples.

In Chapter 1, an overview of common optical microscopy techniques used in biomedical imaging applications was provided. Then, a brief introduction on MEMS fabrication technologies followed by a review of various MEMS actuators developed for optical imaging applications were described. Among optical microscopy techniques, miniaturization of OCT systems is the easiest because only one dimension of laser beam scanning is required. In addition, OCT has the largest imaging depth of about 2 mm. However, its spatial resolution is generally lower (about 10-15 μm) compared to other techniques and also its image contrast is limited due to the speckle effect. MPM has the highest image resolution (≤1 μm) with

penetration depth of about 1 mm. A drawback of MPM systems is requirements for demanding optics and high cost laser sources that results in expensive system development. Confocal microscopy has similar resolution to that of MPM but smaller imaging depth (~ 0.2 mm). However, this limited imaging depth is good enough for certain application such as detection of early epithelial cancers. Confocal microscopy is performed in RCM and FCM modes. FCM images offer higher SNR, but require fluorescence contrast agents to be administrated to the tissue. RCM uses native tissue signals and provides larger penetration depth compared to FCM; which lead us to select RCM method for developing our imaging system. To miniaturize an RCM system, MEMS fabrication technology can be used. This includes, bulk and surface micromachining of Si substrate and deposited layers, and laser micromachining of thin films. All the above techniques were used in fabrication of lens and fiber optic scanners in our systems. Actuation of an optical fiber or a lens can be achieved by electrostatic, piezoelectric, electrothermal or electromagnetic actuation mechanisms. In general, electrostatic actuators have disadvantage of non-linearity and limited actuation range due to snap-in phenomena. Electrothermal actuators are limited by thermal fatigue due to continuous thermal cycling, and piezoelectric actuators require high driving voltages. Electromagnetic actuators typically provide large scanning range and require low driving voltages which make them suitable for clinical applications, and as a result, we use this actuation technique for developing our lens and fiber scanners.

In Chapter 2, we demonstrate fabrication of a lens actuator using MEMS technology. The lens actuator was fabricated using electroplating technique on a Si substrate. The actuator was couples with an optical fiber to develop a catheter for endoscopic applications. The

catheter has outer diameter of 4.75 mm and rigid length of 30 mm. The catheter was used to measure thicknesses of mouse cornea and mouse skin layers, which are useful for studying diseases such as glaucoma and skin cancer. Measured values were close to thickness determined from histology images of cornea and skin tissue. The system was characterized by measuring thicknesses of polymer layers deposited on Si wafers. Five different layers of a negative PR (SU-8) were spin-coated on Si wafers and thicknesses of layers were measured by the confocal system. Results were compared to the thickness values obtained by Wyko optical profiler. Statistical analysis shows uncertainty of measurement of about 11.86 μm with the selected lens and fiber.

In Chapter 3, we used laser micromachining to cut thin nickel foils and form cantilever beams for actuating an optical fiber. The selected laser wavelength was green (532 nm) with energy of 3 mJ. We couple the fiber scanner with a lens actuator to form a 2D imaging system. The fiber scans the tissue in transverse direction while the lens moves in the axial direction. This results in an imaging plane that is perpendicular to the surface of sample (vertical section images). Vertical section images are analogous to histology images and for certain diseases are more useful in diagnosis compared to horizontal section images. The system demonstrated in this chapter is the first magnetically driven confocal scanner that is capable of providing direct and real-time vertical section images of samples. The system was tested by imaging across vertical sections of a polymer channel deposited on a Si wafer and also by imaging cells of an onion epidermal peel layer.

In Chapter 4, we developed another 2D scanner for confocal imaging of biological samples. This scanner obtains horizontal section images of sample and provides two main advantages

compared to other systems. One is that the laser scanning pattern over the sample is a raster pattern. This is favorable because raster scanning offers more uniform sampling and easier image reconstruction compared to other scanning patterns such as spiral and Lissajous. The second advantage is that the scanner is driven by electromagnetic fields only and requires low driving voltages. The scanner is assembled in standard half-inch lens tubes and has length of 57 mm. Optical characterization of the scanner showed resolutions of 1.55 μm and 8.45 μm in lateral and axial directions respectively. We used the system to obtain confocal images of a fruit fly wing and a human colon tissue sample. An image artifact in the form of a wavy pattern was observed in the system. The causes of this image artifact were investigated and correction methods were introduced in appendix B of this thesis.

5.2 Future Work

The work presented in this thesis was a proof-of-principle demonstration of vertical and horizontal optical sectioning imaging of samples in raster scanning patterns using electromagnetic actuation mechanism. The ultimate goal of this research is to develop hand-held systems and endoscopic catheters for *in vivo* imaging of biological tissues. The scanners described in this thesis are developed using off-the-shelf optical components. Large size and mass of these components make miniaturization a challenge and significantly reduces scanning speed of the system. For instance a small custom-made or a polymer lens can be much lighter and allows faster scanning and imaging frame rate. Higher imaging frame rate is desired because it will help to eliminate signal artifacts that are due to external vibrations and involuntary motion of patients. The packaging of the proposed confocal scanners is also important for its use in real applications, particularly for endoscopic imaging of internal

organs. In the design of the device packaging, precise positioning of the scanner with respect to the tissue to control imaging depth needs to be achieved.

Another interesting addition to the current system could be to couple this with a Raman spectroscopy system in order to form a handheld device with dual complementary capabilities: cellular-level resolved confocal imaging combined with accurate and precise Raman spectroscopy of specific subsurface microstructures of tissue *in vivo*. The resulting system will help facilitating precise non-invasive assessment of tissue morphology and biochemistry as well as non-invasive clinical diagnosis and evaluation of diseases such as skin cancer.

BIBLIOGRAPHY

[1] D. Huang, E. Swanson, C. Lin, J. Schuman, W. Stinson, W. Chang, M. Hee, T. Flotte, K. Gregory, C. Puliafito and a. et, "Optical coherence tomography," *Science,* vol. 254, pp. 1178-1181, November 22, 1991.

[2] A. M. Zysk, F. T. Nguyen, A. L. Oldenburg, D. L. Marks and S. A. Boppart, "Optical coherence tomography: a review of clinical development from bench to bedside," *Journal of Biomedical Optics,* vol. 12, pp. 051403-051403, September 1, 2007.

[3] W. Denk, J. Strickler and W. Webb, "Two-photon laser scanning fluorescence microscopy," *Science,* vol. 248, pp. 73-76, April 06, 1990.

[4] K. Koenig and I. Riemann, "High-resolution multiphoton tomography of human skin with subcellular spatial resolution and picosecond time resolution," *Journal of Biomedical Optics,* vol. 8, pp. 432-439, July 1, 2003.

[5] M. Rajadhyaksha, M. Grossman, D. Esterowitz, R. H. Webb and R. R. Anderson, "In Vivo Confocal Scanning Laser Microscopy of Human Skin: Melanin Provides Strong Contrast," *J Investig Dermatol,* vol. 104, pp. 946-952, print, 1995.

[6] K. Nehal S., D. Gareau and M. Rajadhyaksha, "Skin Imaging With Reflectance Confocal Microscopy," *Semin. Cutan. Med. Surg.,* vol. 27, pp. 37-43, 2008.

[7] E. Laemmel, M. Genet, G. Le Goualher, A. Perchant, J. Le Gargasson and E. Vicaut, "Fibered confocal fluorescence microscopy (Cell-viZio) facilitates extended imaging in the

field of microcirculation. A comparison with intravital microscopy," *J. Vasc. Res.,* vol. 41, pp. 400, 2004.

[8] L. Thiberville, S. Moreno-Swirc, T. Vercauteren, E. Peltier, C. CavÃ© and G. Bourg Heckly, "In vivo imaging of the bronchial wall microstructure using fibered confocal fluorescence microscopy," *Am. J. Respir. Crit. Care Med.,* vol. 175, pp. 22, 01, 2007.

[9] J. M. Bustillo, R. T. Howe and R. S. Muller, "Surface micromachining for microelectromechanical systems," *Proc IEEE,* vol. 86, pp. 1552-1574, 1998.

[10] W. J. Fleming, "Overview of automotive sensors," *IEEE Sensors Journal,* vol. 1, pp. 296-308, 2001.

[11] R. Bashir, "BioMEMS: state-of-the-art in detection, opportunities and prospects," *Adv. Drug Deliv. Rev.,* vol. 56, pp. 1565-1586, 2004.

[12] G. M. Rebeiz, *RF MEMS: Theory, Design, and Technology*. Hoboken, New Jersey: John Wiley & Sons, Inc., 2003.

[13] R. A. Conant, P. M. Hagelin, U. Krishnamoorthy, M. Hart, O. Solgaard, K. Y. Lau and R. S. Muller, "A raster-scanning full-motion video display using polysilicon micromachined mirrors," *Sensors & Actuators: A.Physical,* vol. 83, pp. 291-296, 2000.

[14] F. Krogmann, W. Mönch and H. Zappe, "A MEMS-based variable micro-lens system," *Journal of Optics A: Pure and Applied Optics,* vol. 8, pp. S330-S336, 2006.

[15] M. C. Wu, O. Solgaard and J. E. Ford, "Optical MEMS for lightwave communication," *J. Lightwave Technol.,* vol. 24, pp. 4433-4454, 2006.

[16] T. Mitsui, Y. Takahashi and Y. Watanabe, "A 2-axis optical scanner driven nonresonantly by electromagnetic force for OCT imaging," *J Micromech Microengineering,* vol. 16, pp. 2482-2487, 2006.

[17] H. Urey and D. L. Dickensheets, "Display and imaging systems," in *MOEMS: Micro-Opto-Electro-Mechanical Systems*, Bellingham: SPIE Press, 2005, pp. 369.

[18] T. R. Hsu, *MEMS and Microsystems: Design, Manufacture, and Nanoscale Engineering.* Hoboken, New Jersey: John Wiley & Sons, Inc., 2008.

[19] P. R. Miller, R. Aggarwal, A. Doraiswamy, Y. J. Lin, Y. S. Lee and R. J. Narayan, "Laser micromachining for biomedical applications," *JOM Journal of the Minerals, Metals and Materials Society,* vol. 61, pp. 35-40, 2009.

[20] G. D. Valle, R. Osellame and P. Laporta, "Micromachining of photonic devices by femtosecond laser pulses," *Journal of Optics A: Pure and Applied Optics,* vol. 11, pp. 013001, 2009.

[21] W. Hu, Y. C. Shin and G. B. King, "Micromachining of Metals, Alloys, and Ceramics by Picosecond Laser Ablation," *Journal of Manufacturing Science and Engineering,* vol. 132, pp. 011009, 2010.

[22] N. Nguyen and S. H. Chan, "Micromachined polymer electrolyte membrane and direct methanol fuel cells-a review," *J Micromech Microengineering,* vol. 16, pp. 1, 2006.

[23] A. N. Samant and N. B. Dahotre, "Laser machining of structural ceramics—A review," *Journal of the European Ceramic Society,* vol. 29, pp. 969-993, 2009.

[24] B. Pecholt, M. Vendan, Y. Dong and P. Molian, "Ultrafast laser micromachining of 3C-SiC thin films for MEMS device fabrication," *The International Journal of Advanced Manufacturing Technology,* vol. 39, pp. 239-250, 2008.

[25] K. E. Petersen, "Silicon torsional scanning mirror," *IBM J.Res.Develop,* vol. 24, pp. 631–637, 1980.

[26] R. A. Conant, J. T. Nee, K. Y. Lau and R. S. Muller, "A flat high-frequency scanning micromirror," in *Proc. Solid-State Sensor and Actuator Workshop,* 2000, pp. 6–9.

[27] P. R. Patterson, D. Hah, H. Nguyen, H. Toshiyoshi, R. Chao and M. C. Wu, "A scanning micromirror with angular comb drive actuation," in *Proc. IEEE 15th Int. Conf. Micro Electro Mech. Syst,* 2002, pp. 544-547.

[28] S. Kwon and L. Lee, "Stacked two dimensional micro-lens scanner for micro confocal imaging array," in Las Vegas, Nevada, USA, 2002, pp. 483-486.

[29] N. ASADA, "Silicon Micromachined Two-dimensional Galvano Optical Scanner," *IEEE Trans. Magn.,* vol. 30, pp. 4647, 1994.

[30] K. H. Kim, B. H. Park, G. N. Maguluri, T. W. Lee, F. J. Rogomentich, M. G. Bancu, B. E. Bouma, J. F. de Boer and J. J. Bernstein, "Two-axis magnetically-driven MEMS scanning catheter for endoscopic high-speed optical coherence tomography," *Optics Express,* vol. 15, pp. 18130-18140, 2007.

[31] C. P. B. Siu, H. Wang, H. Zeng and M. Chiao, "Dual-axes Confocal Microlens for Raman Spectroscopy," *Micro Electro Mechanical Systems,* pp. 999, 2009.

[32] E. J. Min, J. Na, S. Y. Ryu and B. H. Lee, "Single-body lensed-fiber scanning probe actuated by magnetic force for optical imaging," *Opt. Lett.,* vol. 34, pp. 1897-1899, 06/15, 2009.

[33] E. J. Min, J. G. Shin, Y. Kim and B. H. Lee, "Two-dimensional scanning probe driven by a solenoid-based single actuator for optical coherence tomography," *Opt. Lett.,* vol. 36, pp. 1963-1965, 06/01, 2011.

[34] Y. Pan, H. Xie and G. K. Fedder, "Endoscopic optical coherence tomography based on a microelectromechanical mirror," *Opt. Lett.,* vol. 26, pp. 1966-1968, 2001.

[35] A. Jain, A. Kopa, Y. Pan, G. K. Fedder and H. Xie, "A two-axis electrothermal micromirror for endoscopic optical coherence tomography," *IEEE Journal of Selected Topics in Quantum Electronics,* vol. 10, pp. 636-642, 2004.

[36] H. Xie, J. Sun, S. Guo and L. Wu, "3D endoscopic optical coherence tomography based on rapid-scanning MEMS mirrors (Proceedings Paper)," vol. 7634, pp. 76340X-1, 2009.

[37] H. Goto and K. Imanaka, "Super-compact dual-axis optical scanning unit applying a torsional spring resonator driven by a piezoelectric actuator," in *Proceedings of SPIE,* 1991, pp. 272.

[38] J. Tsaur, Z. J. Wang, L. Zhang, M. Ichiki, J. W. Wan and R. Maeda, "Preparation and application of lead zirconate titanate (PZT) films deposited by hybrid process: sol-gel method and laser ablation," *Jpn.J.Appl.Phys,* vol. 41, pp. 6664-6668, 2002.

[39] M. T. Myaing, D. J. MacDonald and X. Li, "Fiber-optic scanning two-photon fluorescence endoscope," *Opt. Lett.,* vol. 31, pp. 1076-1078, 04/15, 2006.

[40] J. Pei, F. L. Degertekin, B. V. Honein, B. Khuri-Yakub and K. C. Saraswat, "In situ thin film thickness measurement using ultrasonics waves," in 1994, pp. 1237-1240 vol.2.

[41] Lhotka J., Kuzel R., Cappuccio G. and Valvoda V., "Thickness determination of thin polycrystalline film by grazing incidence X-ray diffraction," *Surface and Coatings Technology,* vol. 148, pp. 95-100, 2001.

[42] L. C. KUYPERS, W. F. DECRAEMER, J. J. J. DIRCKX and J. -. TIMMERMANS, "A procedure to determine the correct thickness of an object with confocal microscopy in case of refractive index mismatch," *J. Microsc.,* vol. 218, pp. 68-78, 2005.

[43] J C Manifacier and J Gasiot and,J.P.Fillard, "A simple method for the determination of the optical constants n, k and the thickness of a weakly absorbing thin film," *Journal of Physics E: Scientific Instruments,* vol. 9, pp. 1002, 1976.

[44] N. J. Harrick, "Determination of Refractive Index and Film Thickness from Interference Fringes," *Appl. Opt.,* vol. 10, pp. 2344-2349, 10/01, 1971.

[45] C. Arens, H. Glanz, J. Wönckhaus, K. Hersemeyer and M. Kraft, "Histologic assessment of epithelial thickness in early laryngeal cancer or precursor lesions and its impact on endoscopic imaging," *European Archives of Oto-Rhino-Laryngology,* vol. 264, pp. 645-649, 2007.

[46] N. Ehlers, T. Bramsen and S. Sperling, "Applanation tonometry and central corneal thickness," *Acta Ophthalmol.,* vol. 53, pp. 34, 03, 1975.

[47] M. Black, "A modified radiographic method for measuring skin thickness," *Br. J. Dermatol.,* vol. 81, pp. 661, 09, 1969.

[48] C. Tan, B. Statham, R. Marks and P. Payne, "Skin thickness measurement by pulsed ultrasound: its reproducibility, validation and variability," *Br. J. Dermatol.,* vol. 106, pp. 657, 06, 1982.

[49] C. Schmucker and F. Schaeffel, "In vivo biometry in the mouse eye with low coherence interferometry," *Vision Res.,* vol. 44, pp. 2445, 2004.

[50] X. Zhou, J. Xie, M. Shen, J. Wang, L. Jiang, J. Qu and F. Lu, "Biometric measurement of the mouse eye using optical coherence tomography with focal plane advancement," *Vision Res.,* vol. 48, pp. 1137, 04, 2008.

[51] H. Li, W. Petroll, T. MÃ¸ller-Pedersen, J. Maurer, H. Cavanagh and J. Jester, "Epithelial and corneal thickness measurements by in vivo confocal microscopy through focusing (CMTF)," *Curr. Eye Res.,* vol. 16, pp. 214, 03, 1997.

[52] S. Patel, J. McLaren, D. Hodge and W. Bourne, "Normal human keratocyte density and corneal thickness measurement by using confocal microscopy in vivo," *Invest. Ophthalmol. Vis. Sci.,* vol. 42, pp. 333, 02, 2001.

[53] Cox G. and Sheppard C.J.R., "Measurement of thin coatings in the confocal microscope," *Micron,* vol. 32, pp. 701-705, 2001.

[54] Noel Ziebarth and Fabrice Manns,and Jean, "Fibre-optic focus-detection system for non-contact, high-resolution thickness measurement of transparent tissues," *J. Phys. D,* vol. 38, pp. 2708, 2005.

[55] N. Ziebarth, F. Manns, S. Uhlhorn, A. Venkatraman and J. Parel, "Noncontact optical measurement of lens capsule thickness in human, monkey, and rabbit postmortem eyes," *Invest. Ophthalmol. Vis. Sci.,* vol. 46, pp. 1690, 05, 2005.

[56] S. Kwon, V. Milanovic and L. P. Lee, "Vertical microlens scanner for 3D imaging," in Hilton Head Island, SC, 2002, .

[57] A. Jain and H. Xie, "An electrothermal microlens scanner with low-voltage large-vertical-displacement actuation," *Photonics Technology Letters, IEEE,* vol. 17, pp. 1971-1973, 2005.

[58] H. Toshiyoshi, W. Piyawattanametha, Cheng-Ta Chan and M. C. Wu, "Linearization of electrostatically actuated surface micromachined 2-D optical scanner," *Microelectromechanical Systems, Journal of,* vol. 10, pp. 205-214, 2001.

[59] R. A. Conant and R. S. Muller, "Cyclic fatigue testing of surface-micromachined thermal actuators," in *ASME International Mechanical Engineering Congress and Exposition,* Anaheim, CA, 1998, pp. 273-277.

[60] R. Bakke and P. Q. Olsson, "Biofilm thickness measurements by light microscopy," *J. Microbiol. Methods,* vol. 5, pp. 93-98, 7, 1986.

[61] G. Martin, Thickness of an optical section, Keck Microscopy Facility., Univ. of Washington, 2007, http://depts.washington.edu/keck/leica/pinhole.htm , Accessed 20 Aug., 2010.

[62] G. Rizzoni, "Electrical engineering," in *The CRC Handbook of Mechanical Engineering*, 2nd ed., F. Kreith and D. Y. Goswam, Eds. Boca Raton: CRC Press LLC, 2005, pp. 5-1.

[63] Xinchun Shang and Ernie Pan and,Liping Qin, "Mathematical modeling and numerical computation for the vibration of a magnetostrictive actuator," *Smart Mater Struct,* vol. 17, pp. 045026, 2008.

[64] W. Young and R. Budynas, *Roark's Formulas for Stress and Strain.* New York: McGraw-Hill, 2002.

[65] Hakan Urey and Cihan Kan and Wyatt,O.Davis, "Vibration mode frequency formulae for micromechanical scanners," *J Micromech Microengineering,* vol. 15, pp. 1713, 2005.

[66] S. S. Rao, "Harmonically excited vibration," in *Mechanical Vibrations*, 2nd ed., Addison-Wesley Publishing Company, 1990, pp. 127.

[67] Wyko NT1100 Optical Profiling System, www.veeco.com, Accessed 20 Aug., 2010.

[68] SU-8 3000 Permanent Epoxy Negative Photoresist, http://www.microchem.com/products/pdf/SU-8%203000%20Data%20Sheet.pdf , accessed 20 Aug., 2010.

[69] J. Bland and D. Altman, "Statistical methods for assessing agreement between two methods of clinical measurement," *Lancet,* vol. 1, pp. 307, 02, 1986.

[70] W.S. Rasband, ImageJ, Natl. Inst. of Health, Bethesda, Maryland, USA, http://rsb.info.nih.gov/ij/, 1997-2010.

[71] S. Remtulla and P. E. Hallett, "A schematic eye for the mouse, and comparisons with the rat," *Vision Res.,* vol. 25, pp. 21-31, 1985.

[72] H. Zeng, C. MacAulay, D. I. McLean and B. Palcic, "Reconstruction of in vivo skin autofluorescence spectrum from microscopic properties by Monte Carlo simulation," *Journal of Photochemistry and Photobiology B: Biology,* vol. 38, pp. 234-240, /4, 1997.

[73] C. Fox, F. Johnson, J. Whiting and P. Roller, "Formaldehyde fixation," *J. Histochem. Cytochem.,* vol. 33, pp. 845, 08, 1985.

[74] C. L. Arrasmith, D. L. Dickensheets and A. Mahadevan-Jansen, "MEMS-based handheld confocal microscope for in-vivo skin imaging," *Opt. Express,* vol. 18, pp. 3805-3819, 02/15, 2010.

[75] J. T. C. Liu, M. J. Mandella, H. Ra, L. K. Wong, O. Solgaard, G. S. Kino, W. Piyawattanametha, C. H. Contag and T. D. Wang, "Miniature near-infrared dual-axes confocal microscope utilizing a two-dimensional microelectromechanical systems scanner," *Opt. Lett.,* vol. 32, pp. 256-258, 02/01, 2007.

[76] K. C. Maitland, H. J. Shin, H. Ra, D. Lee, O. Solgaard and R. Richards-Kortum, "Single fiber confocal microscope with a two-axis gimbaled MEMS scanner for cellular imaging," *Opt. Express,* vol. 14, pp. 8604-8612, 09/18, 2006.

[77] K. Kumar, R. Avritscher, Y. Wang, N. Lane, D. Madoff, T. Yu, J. Uhr and X. Zhang, "Handheld histology-equivalent sectioning laser-scanning confocal optical microscope for interventional imaging," *Biomed. Microdevices,* vol. 12, pp. 223, 04, 2010.

[78] N. Dhaubanjar, H. Hu, D. Dave, P. Phuyal, J. Sin, H. Stephanou and J. -. Chiao, "A compact optical fiber scanner for medical imaging," *Smart Structures, Devices, and Systems III. Edited by Al-Sarawi, Said F. . Proceedings of the SPIE,* vol. 6414, pp. 64141Z, 01/2007, 2007.

[79] M. T. Myaing, D. J. MacDonald and X. Li, "Fiber-optic scanning two-photon fluorescence endoscope," *Opt. Lett.,* vol. 31, pp. 1076-1078, 04/15, 2006.

[80] E. J. Min, J. G. Shin, Y. Kim and B. H. Lee, "Two-dimensional scanning probe driven by a solenoid-based single actuator for optical coherence tomography," *Opt. Lett.,* vol. 36, pp. 1963-1965, 06/01, 2011.

[81] H. Ra, W. Piyawattanametha, M. J. Mandella, P. Hsiung, J. Hardy, T. D. Wang, C. H. Contag, G. S. Kino and O. Solgaard, "Three-dimensional in vivo imaging by a handheld dual-axes confocal microscope," *Opt. Express,* vol. 16, pp. 7224-7232, 05/12, 2008.

[82] M. Booth, R. Juškaitis and T. Wilson, "Spectral confocal reflection microscopy using a white light source," *J. Europ. Opt. Soc. Rap. Public.,* vol. 3, pp. 08026, 2008.

[83] T. D. Wang, C. H. Contag, M. J. Mandella, N. Chan and G. S. Kino, "Dual-axes confocal microscopy with post-objective scanning and low-coherence heterodyne detection," *Opt. Lett.,* vol. 28, pp. 1915-1917, 10/15, 2003.

[84] N. Callamaras and I. Parker, "Construction of a confocal microscope for real-time x-y and x-z imaging," *Cell Calcium,* vol. 26, pp. 271-279, 1999.

[85] T. D. Wang, K. Kurabayashi, K. Oldham and Z. Qiu, "Targeted dual-Axes confocal imaging apparatus with vertical scanning capabilities," US Patent 2011/0125029 A1, Oct 29, 2011.

[86] J. E. Shigley, C. R. Mischke and R. G. Budynas, *Mechanical Engineering Design.* New York, USA: McGraw-Hill, 2004.

[87] T. Wilson and A. R. Carlini, "Size of the detector in confocal imaging systems," *Opt. Lett.,* vol. 12, pp. 227-229, 04/01, 1987.

[88] M. Gu, C. J. R. Sheppard and X. Gan, "Image formation in a fiber-optical confocal scanning microscope," *J. Opt. Soc. Am. A,* vol. 8, pp. 1755-1761, 11/01, 1991.

[89] M. Rajadhyaksha, R. R. Anderson and R. H. Webb, "Video-Rate Confocal Scanning Laser Microscope for Imaging Human Tissues In Vivo," *Appl. Opt.,* vol. 38, pp. 2105-2115, 04/01, 1999.

[90] M. D. Sharma and C. J. R. Sheppard, "Effects of system geometry on the axial response of the fibreoptical confocal microscope," *Journal of Modern Optics,* vol. 46, pp. 605-621, 03/01; 2012/09, 1999.

[91] K. Venkateswaran, A. Roorda and F. Romero-Borja, "Theoretical modeling and evaluation of the axial resolution of the adaptive optics scanning laser ophthalmoscope," *Journal of Biomedical Optics,* vol. 9, pp. 132-138, January 1, 2004.

[92] B. A. Flusberg, E. D. Cocker, W. Piyawattanametha, J. C. Jung, E. L. M. Cheung and M. J. Schnitzer, "Fiber-optic fluorescence imaging," *Nature Methods,* vol. 2, pp. 941-950, 2005.

[93] M. Nakao, S. Yoshida, S. Tanaka, Y. Takemura, S. Oka, M. Yoshihara and K. Chayama, "Optical biopsy of early gastroesophageal cancer by catheter-based reflectance-type laser-scanning confocal microscopy," *J. Biomed. Opt.,* vol. 13, pp. 054043-054043-5, 2008.

[94] A. L. Polglase, W. J. McLaren, S. A. Skinner, R. Kiesslich, M. F. Neurath and P. M. Delaney, "A fluorescence confocal endomicroscope for in vivo microscopy of the upper-and the lower-GI tract." *Gastrointest. Endosc.,* vol. 62, pp. 686, 2005.

[95] J. Benschop and G. Van Rosmalen, "Confocal compact scanning optical microscope based on compact disc technology," *Appl. Opt.,* vol. 30, pp. 1179-1184, 1991.

[96] T. D. Wang, M. J. Mandella, C. H. Contag and G. S. Kino, "Dual-axis confocal microscope for high-resolution in vivo imaging," *Opt. Lett.,* vol. 28, pp. 414-416, 2003.

[97] D. L. Dickensheets and G. S. Kino, "Silicon-micromachined scanning confocal optical microscope," *Microelectromechanical Systems, Journal of,* vol. 7, pp. 38-47, 1998.

[98] K. C. Maitland, H. J. Shin, H. Ra, D. Lee, O. Solgaard and R. Richards-Kortum, "Single fiber confocal microscope with a two-axis gimbaled MEMS scanner for cellular imaging," *Optics Express,* vol. 14, pp. 8604-8612, 2006.

[99] J. T. C. Liu, M. J. Mandella, N. O. Loewke, H. Haeberle, H. Ra, W. Piyawattanametha, O. Solgaard, G. S. Kino and C. H. Contag, "Micromirror-scanned dual-axis confocal

microscope utilizing a gradient-index relay lens for image guidance during brain surgery," *J. Biomed. Opt.,* vol. 15, pp. 026029-026029-5, 2010.

[100] P. M. Hagelin and O. Solgaard, "Optical raster-scanning displays based on surface-micromachined polysilicon mirrors," *Selected Topics in Quantum Electronics, IEEE Journal of,* vol. 5, pp. 67-74, 1999.

[101] H. Miyajima, N. Asaoka, T. Isokawa, M. Ogata, Y. Aoki, M. Imai, O. Fujimori, M. Katashiro and K. Matsumoto, "A MEMS electromagnetic optical scanner for a commercial confocal laser scanning microscope," *Microelectromechanical Systems, Journal of,* vol. 12, pp. 243-251, 2003.

[102] H. Ra, W. Piyawattanametha, M. J. Mandella, P. L. Hsiung, J. Hardy, T. D. Wang, C. H. Contag, G. S. Kino and O. Solgaard, "Three-dimensional in vivo imaging by a handheld dual-axes confocal microscope," *Optics Express,* vol. 16, pp. 7224-7232, 2008.

[103] H. Mansoor, H. Zeng and M. Chiao, "A micro-fabricated optical scanner for rapid non-contact thickness measurement of transparent films," *Sensors and Actuators A: Physical,* vol. 167, pp. 91-96, 2011.

[104] H. Mansoor, H. Zeng and M. Chiao, "Real-time thickness measurement of biological tissues using a microfabricated magnetically-driven lens actuator," *Biomed. Microdevices,* vol. 13, pp. 641-649, 2011.

[105] F. Helmchen, M. S. Fee, D. W. Tank and W. Denk, "A miniature head-mounted two-photon microscope: High-resolution brain imaging in freely moving animals," *Neuron,* vol. 31, pp. 903-912, 2001.

[106] D. R. Rivera, C. M. Brown, D. G. Ouzounov, I. Pavlova, D. Kobat, W. W. Webb and C. Xu, "Compact and flexible raster scanning multiphoton endoscope capable of imaging unstained tissue," *Proceedings of the National Academy of Sciences,* vol. 108, pp. 17598-17603, 2011.

[107] E. J. Seibel, C. M. Brown, J. A. Dominitz and M. B. Kimmey, "Scanning single fiber endoscopy: a new platform technology for integrated laser imaging, diagnosis, and future therapies," *Gastrointest. Endosc. Clin. N. Am.,* vol. 18, pp. 467-478, 2008.

[108] T. Wu, Z. Ding, K. Wang, M. Chen and C. Wang, "Two-dimensional scanning realized by an asymmetry fiber cantilever driven by single piezo bender actuator for optical coherence tomography," *Optics Express,* vol. 17, pp. 13819-13829, 2009.

[109] C. M. Lee, C. J. Engelbrecht, T. D. Soper, F. Helmchen and E. J. Seibel, "Scanning fiber endoscopy with highly flexible, 1 mm catheterscopes for wide‐field, full‐color imaging," *Journal of Biophotonics,* vol. 3, pp. 385-407, 2010.

[110] X. Liu, M. J. Cobb, Y. Chen, M. B. Kimmey and X. Li, "Rapid-scanning forward-imaging miniature endoscope for real-time optical coherence tomography," *Opt. Lett.,* vol. 29, pp. 1763-1765, 2004.

[111] S. Boppart, B. E. Bouma, C. Pitris, G. J. Tearney, J. G. Fujimoto and M. Brezinski, "Forward-imaging instruments for optical coherence tomography," *Opt. Lett.,* vol. 22, pp. 1618-1620, 1997.

[112] Z. Li and L. Fu, "Note: A resonant fiber-optic piezoelectric scanner achieves a raster pattern by combining two distinct resonances," *Rev. Sci. Instrum.,* vol. 83, pp. 086102-086102-3, 2012.

[113] P. Pandojirao-Sunkojirao, S. M. N. Rao, P. C. Phuyal, N. Dhaubanjar and J. C. Chiao, "A Magnetic Actuator for Fiber-Optic Applications," *International Journal of Optomechatronics,* vol. 3, pp. 215-232, 2009.

[114] K. Zhang, Y. Huang and J. U. Kang, "Full-range Fourier domain optical coherence tomography imaging probe with a magnetic-driven resonant fiber cantilever," *Optical Engineering,* vol. 50, pp. 119002-119002-6, 2011.

[115] E. J. Min, J. Na, S. Y. Ryu and B. H. Lee, "Single-body lensed-fiber scanning probe actuated by magnetic force for optical imaging," *Opt. Lett.,* vol. 34, pp. 1897-1899, 2009.

[116] H. Mansoor, H. Zeng, K. Chen, Y. Yu, J. Zhao and M. Chiao, "Vertical optical sectioning using a magnetically driven confocal microscanner aimed for in vivo clinical imaging," *Optics Express,* vol. 19, pp. 25161-25172, 2011.

[117] B. H. W. Hendriks, W. C. J. Bierhoff, J. J. L. Horikx, A. E. Desjardins, C. A. Hezemans, G. W‘t Hooft, G. W. Lucassen and N. Mihajlovic, "High-resolution resonant and nonresonant fiber-scanning confocal microscope," *J. Biomed. Opt.,* vol. 16, pp. 026007-026007-8, 2011.

[118] G. E. Rosman, B. C. Jones, R. A. Pattie and C. G. Byrne, *Optical Fiber Scanning Apparatus,* 2011.

[119] J. M. Zavislan, “Imaging System using Polarization Effects to Enhance Image Quality,” US Patent 6134010, Oct 17, 2000.

[120] G. D. Boreman, *Modulation Transfer Function in Optical and Electro-Optical Systems.* SPIE Press Bellingham, WA, 2001.

[121] H. A. Haus, *Waves and Fields in Optoelectronics.* Prentice-Hall New Jersey, 1984.

[122] P. J. Dwyer, C. A. DiMarzio, J. M. Zavislan, W. J. Fox and M. Rajadhyaksha, "Confocal reflectance theta line scanning microscope for imaging human skin in vivo," *Opt. Lett.,* vol. 31, pp. 942-944, 2006.

[123] M. Madou, "Fundamentals of microfabrication. 1997," *CRC Press LLC.Capítulo,* vol. 1, pp. 1-50, .

[124] C. L. Hoy, N. J. Durr and A. Ben-Yakar, "Fast-updating and nonrepeating Lissajous image reconstruction method for capturing increased dynamic information," *Appl. Opt.,* vol. 50, pp. 2376-2382, 2011.

[125] T. Tuma, J. Lygeros, V. Kartik, A. Sebastian and A. Pantazi, "High-speed multiresolution scanning probe microscopy based on Lissajous scan trajectories," *Nanotechnology,* vol. 23, pp. 185501, 2012.

[126] S. Chen, X. Feng, Y. Li, C. Zhou, P. Xi and Q. Ren, "Software controlling algorithms for the system performance optimization of confocal laser scanning microscope," *Biomedical Signal Processing and Control,* vol. 5, pp. 223-228, 2010.

[127] Q. Y. J. Smithwick, J. Vagners, P. G. Reinhall and E. J. Seibel, "54.3: Modeling and control of the resonant fiber scanner for laser scanning display or acquisition," in *SID Symposium Digest of Technical Papers,* 2012, pp. 1455-1457.

[128] Y. Zhao, F. E. H. Tay, F. S. Chau and G. Zhou, "A nonlinearity compensation approach based on Delaunay triangulation to linearize the scanning field of dual-axis micromirror," *J Micromech Microengineering,* vol. 15, pp. 1972, 2005.

APPENDICES

APPENDIX A: LENS ACTUATOR FABRICATION

A.1 Photolithography Steps

Fabrication of nickel flexure for lens actuation involves three masking steps as described in the following sections.

A.1.1 First Masking Step: Patterning of SiO_2

The substrate used for fabrication is a double side polished Si wafer with a 2 μm thick SiO_2 layer thermally grown on both sides. After nickel electroplating, the flexure must be released by etching the Si. The first masking step is used to remove the SiO_2 to define Si etching area. First, wafer cleaning and hexamethyldisilazane (HDMS) priming was performed to promote photoresist adhesion to the wafer. These standard steps are done according to the guidelines provided in any photolithography process document. Then, a thin layer (~5 μm) of SPR 220-7 PR was spin-coated on one side of the Si (spinning at 3000 RPM for 40 s). The PR was baked on a hotplate at 115 ºC for 90 s, allowed to cool, transferred to a mask aligner, and exposed to UV light for 90 s. Exposure was done by a 405 nm UV light (USHIO 250W Hg lamp). The photoresist was then developed in a Megaposit MF-24A developer solution that etches away the exposed area of the SPR 220-7 positive photoresist. The mask used in this step is a dark-field photo mask as illustrated in Figure 0.1. The portions of SPR 220-7 that are underneath the transparent parts of the mask are exposed to the UV light and are etched away when placed in the developer solution.

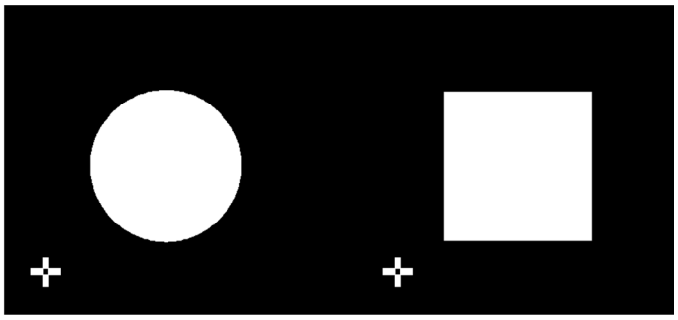

Figure 0.1 First photo mask for etching SiO_2. Cross marks are used as alignment marks.

The other side of Si wafer was covered by a PVC tape with synthetic acrylic adhesive bonded to one side. Exposed SiO_2 was etched in a 7:1 buffered oxide etch (BOE) solution. After etching, PVC tape was peeled and SPR was removed by acetone.

A.1.2 Second Masking Step: Patterning of Electrodes

An electrode area is required for electroplating process. This was created by the second masking process followed by a lift-off process. First 10 μm thick SPR 220-7 PR was spin-coated on the Si wafer (same side as the first masking step). Spinning speed was 1500 RPM for 50 s to uniformly coat the wafer with PR, followed by a 3000 RPM for 1 s for removing the excess PR from the edge of the wafer. This will help to form a better contact between the PR and the mask during the exposure. PR was then baked at 115 ºC for 90 s and transferred to the mask aligner. Second mask was aligned with the features on the wafer from the first masking step using alignment marks. PR was exposed to the UV light for about 180 s and developed for 3 min. Figure 0.2 shows design of the mask used in this step. The two parallel lines on the sides of each feature act as wires to provide electrical connection for electroplating.

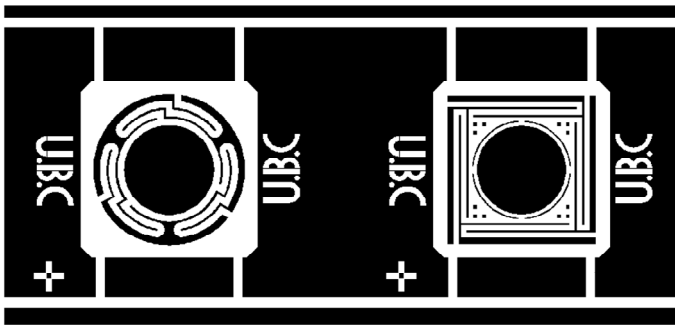

Figure 0.2 Dark-field photo mask used for defining the electrode area and fabricating PR mold for electroplating step.

Then, the wafer was transferred to an electron beam evaporator (Evaporator 2000) for deposition of 50 nm chromium (Cr) and 150 nm gold (Au). After deposition, an ultrasonic lift-off was performed in acetone to remove the PR and excess/unwanted Cr/Au. After the second masking process, a pattern of gold similar to the design of the second mask is formed on the Si wafer.

A.1.3 Third Masking Step: Fabrication of Mold for Electroplating

A mold for electroplating nickel is fabricated on the Si substrate using a thick layer of SPR 220-7 PR. The advantage of using this PR is the ease of removing after electroplating process. To fabricate the mold, first the Si wafer is primed using HMDS. Next, the PR was spin-coated onto the substrate at 150 RPM for 90 s followed by a 3500 RPM spin for 1.5 s to remove the extra PR that was formed around the edge of the substrate. To minimize shrinkage of the high aspect ratio PR, soft baking is started at 40 °C and the temperature is gradually increased to 115 °C in 10 minutes. Finally, using the third mask, the PR is exposed to the UV light for 420 s and is developed for 12 min. Using the described process, molds with thicknesses up to 32 μm in a single process can be fabricated. The third mask used in our fabrication has the exact same design and the second mask shown in Figure 0.2.

A.2 Electroplating Process

The nickel was deposited on the Si substrate from a nickel electroplating solution consisting of nickel sulfate (170 g/l), nickel chloride (25 g/l) and boric acid (15 g/l) (CASWELL Inc.). Thickness and quality of electroplated layer depends on several parameters including the plating solution composition, temperature, electrodes area and distance, and current density. Our plating was done at room temperature (22 °C) with a current density of 3 mA/cm^2 and at electrode distance of 2 cm. Figure 0.3 shows the nickel thickness as a function of electroplating time.

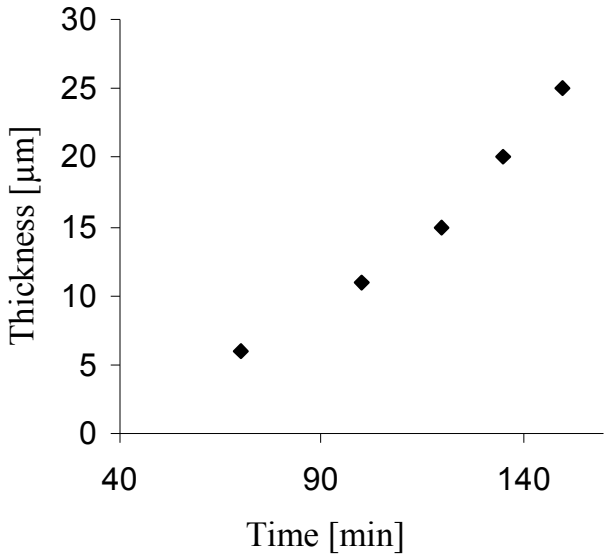

Figure 0.3 The thickness of electroplated nickel as a function of deposition time.

During the electroplating process, hydrogen bubbles may be formed on the cathode surface that cause pitting in the electroplated film. To avoid this issue, sodium lauryl sulfate was added to the solution as a wetting agent. Figure 0.4 shows pitting in the electroplated nickel before addition of wetting agent.

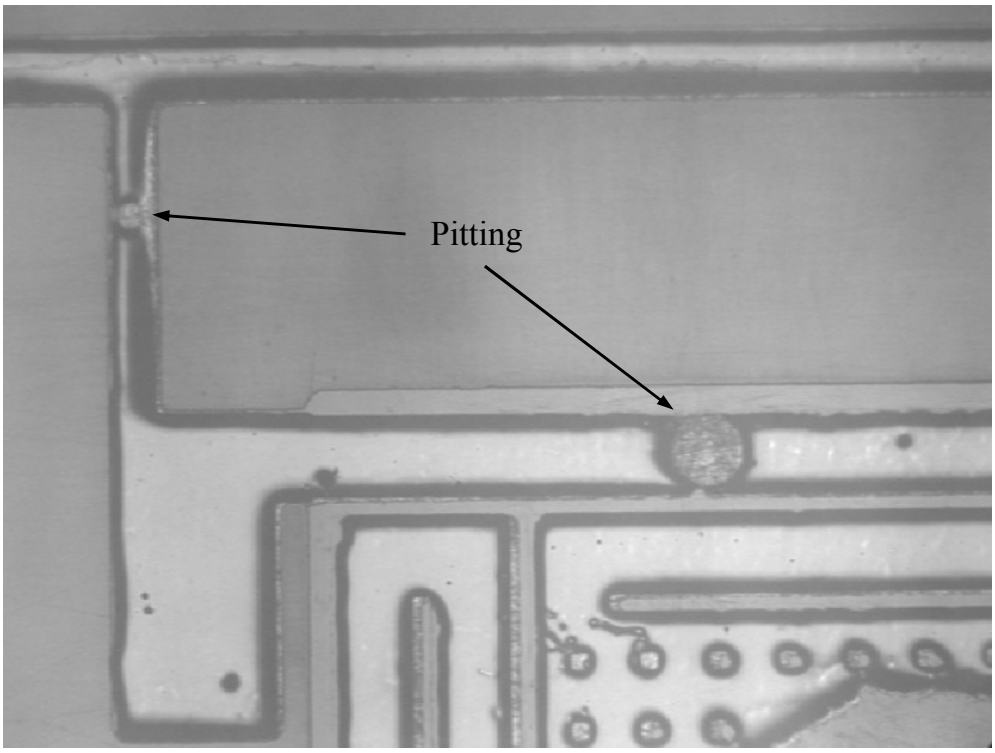

Figure 0.4 electroplated nickel flexure on Si wafer with pitting.

A ~20 μm thick layer of nickel was electroplated on the Si wafer. Figure 0.5 is the thickness profile of nickel flexure measured by Wyko optical profiler. Measurement shows a ~4 μm variation in the thickness of flexure across the entire plated area. This non-uniformity is caused by several factors including geometric factors and non-uniform current densities. This small thickness variation does not have a significant effect on the performance of electromagnetic lens actuators.

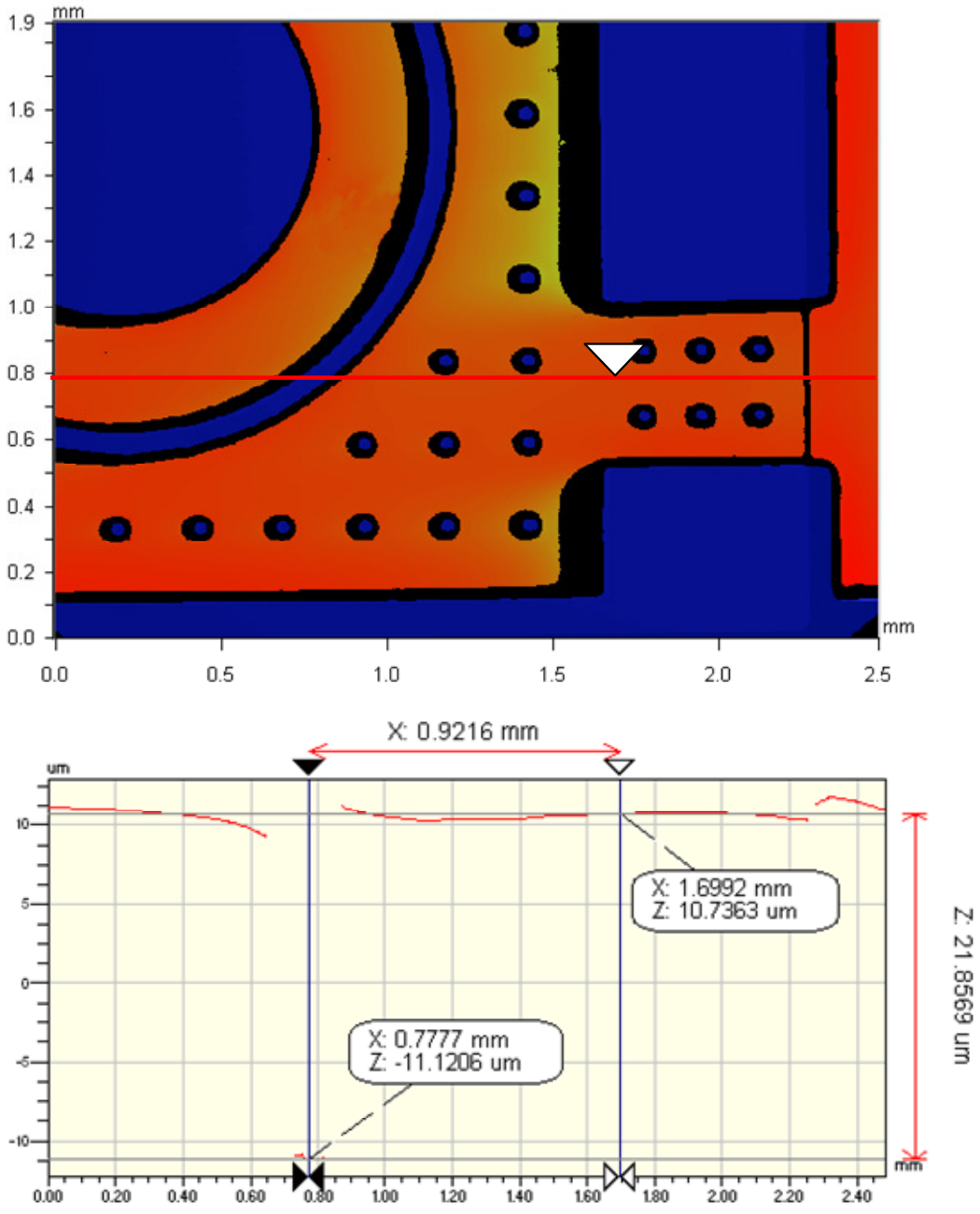

Figure 0.5 thickness profile of electroplated nickel measured by Wyko optical profiler.

Figure 0.6 shows a portion of electroplated nickel flexure on a Si substrate. The small holes in the flexure are etch-holes and are used for reducing the time required for etching the Si underneath the flexure. Etching was done in a 20 wt% KOH at 85 °C and finally a lens was

fixed into the lens holder using a UV-curable adhesive. Figure 0.7 shows photos of four designs of electroplated lens actuators.

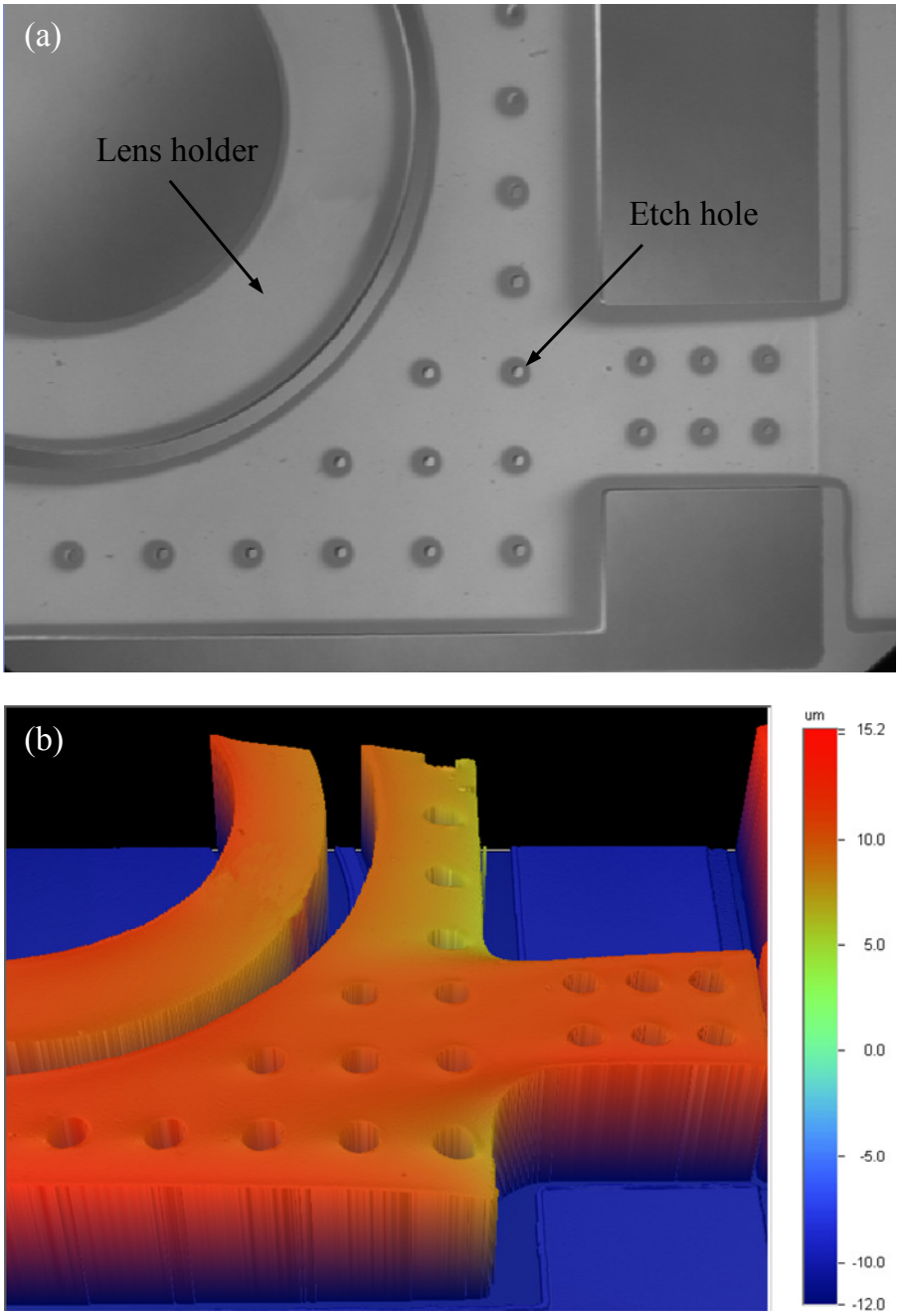

Figure 0.6 (a) Photo and (b) 3D illustration of electroplated nickel flexure obtained by Wyko optical profiler.

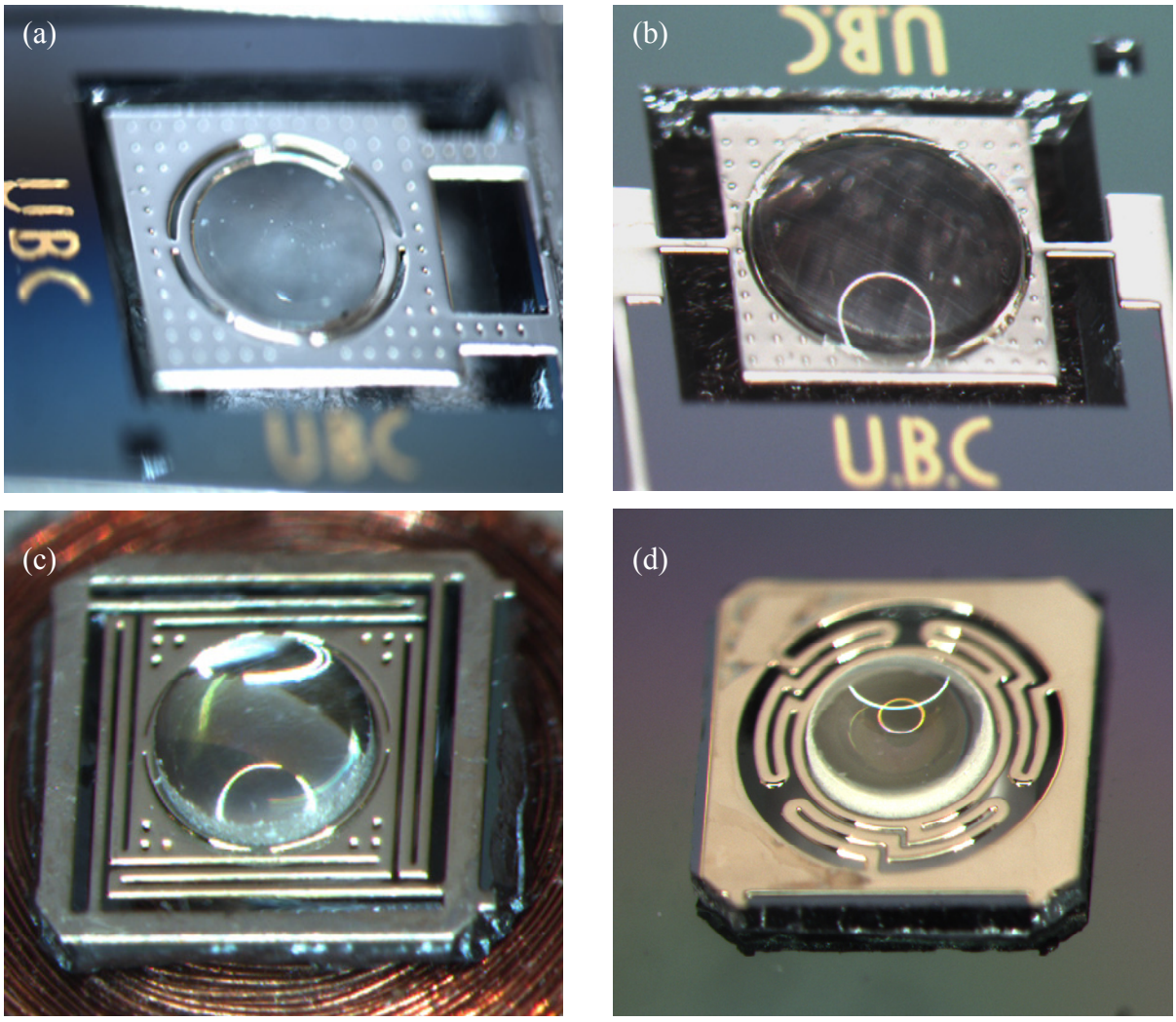

Figure 0.7 Photos of four fabricated nickel flexures for lens actuation showing (a) cantilever beams, (b) torsional beams, (c) rectangular folded beams, and (d) circular folded beams; suspending a nickel platform and a lens in an electromagnetic field. Lenses have diameter of 1.5 mm.

APPENDIX B: CORRECTION OF IMAGE DISTORTION

A.3 Introduction

Images obtained from optical scanners may be distorted due to a variety of factors, including optical distortion, detector distortion, instability of the specimen, and motion artifacts of the laser beam scanning system. Mechanical motion artifacts of actuators may be due to asymmetry in mechanical stiffness of the structure or unevenness of driving forces. Chen et al. in 2010 [126] showed distortion correction of confocal images obtained using galvanometric scanning mirrors. The distortion was in the form of a line shift that originated from asymmetry in the movement of a galvanometric mirror in backward and forward scanning directions. Smithwick et al. [127] developed a fiber optic actuator using a piezo-electric tube to generate spiral scanning patterns of a laser beam. Image distortions due to the dynamics of the system were corrected by implementing a controller that forced the scanner to follow a desired scan pattern. Images from optical systems that use micromirrors developed by MEMS technology may also be distorted due to nonlinearities of the scanner dynamics. Various linearization methods have been developed by researchers to improve image distortions of these system [58][128].

The scanner described in Chapter 4 of this thesis moves an optical fiber in a raster scanning pattern. The system was successfully used for confocal imaging of samples; however, we observed an unwanted distortion in a form of a wavy pattern in the fast scanning axis of the confocal images. We had also observed similar image artifacts in our earlier work that was described in Chapter 3. Initially, we partially improved the image artifacts by post-processing of image data using tools such as ImageJ and MATLAB; however, for clinical applications it

is advantageous to obtain artifact-free images in real-time. After careful analysis of our setup we have concluded that image distortions in our systems are due to motion artifacts of actuators, originating from magnetic driving forces. In this appendix we discuss the cause for this distortion and describe the method implemented to overcome the issue.

A.4 Experimental Results and Discussion

The natural frequency corresponding to the first fundamental vibration mode of beam B2 in our scanner is 648 Hz. We measured this value using the Fast Fourier Transform (FFT) of impulse response of the beam as shown in Figure 0.1.

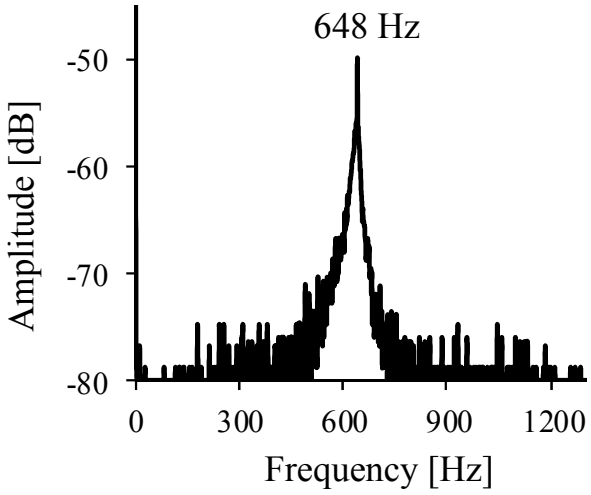

Figure 0.1 FFT of impulse response of B2.

To drive our scanner, initially C2 was driven by a periodic current with a frequency of 324 Hz, half the resonant frequency of B2 and no DC bias. Based on Eq. 2.8, this driving current should result in a magnetic force matching the resonant frequency of B2. However, during system characterizations, it was observed that the peak amplitudes of B2 actuations measured by an LDV were not equal. Figure 0.2 shows the amplitude of the driving current

at frequency of 324 Hz to Coil-2 (Figure 0.2 (a)), measured displacement of B2 and its zoomed-in view (Figure 0.2 (b) and (c)), and FFT response of B2 (Figure 0.2 (d)). This response indicates that actuation of beam at 648 Hz is modulated by another signal at the frequency of driving current (324 Hz).

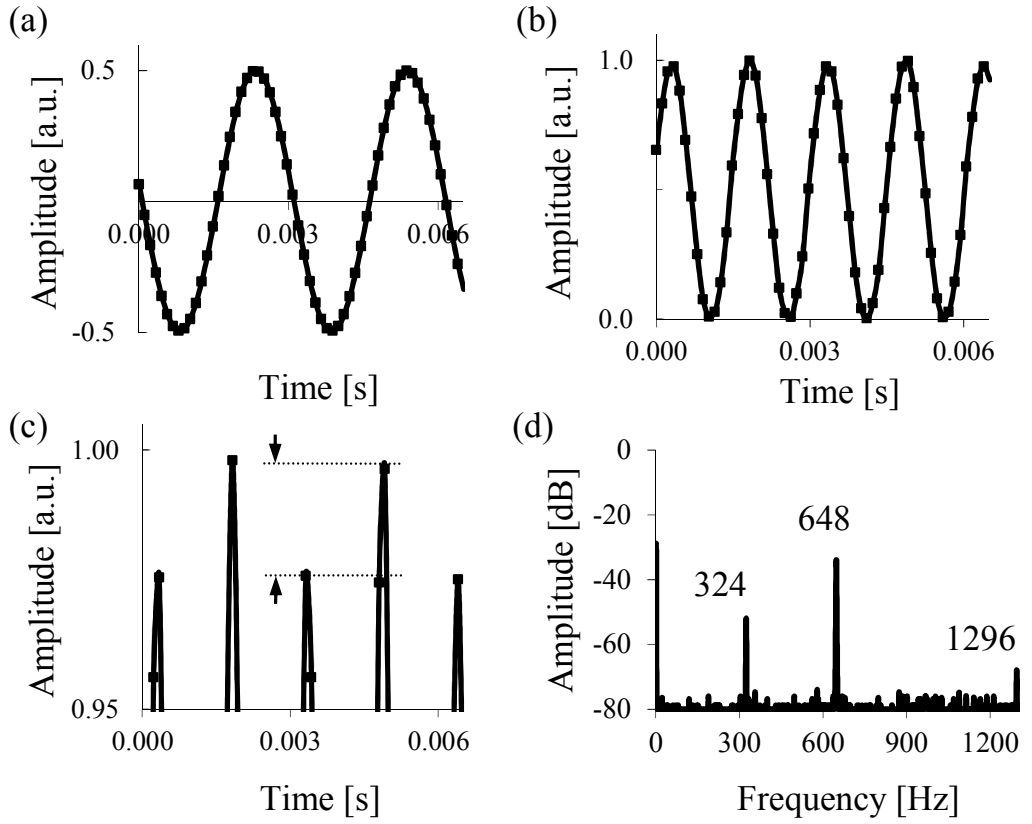

Figure 0.2 Experimental measurement of (a) driving signal at 324 Hz with no DC bias applied to coil C2, (b) beam B2 displacement measured by LDV (displacement frequency is 648 Hz), (c) zoomed-in view of the beam displacement signal, and (d) FFT of response with driving current at 324 Hz frequency and no DC bias.

An effect of this modulated peak amplitude was more visible when the scanner was used for confocal imaging (Figure 0.3). In the confocal images every other line was shifted up in the fast-scan axis, Y, by a few pixels which resulted in an unwanted wavy pattern in the image.

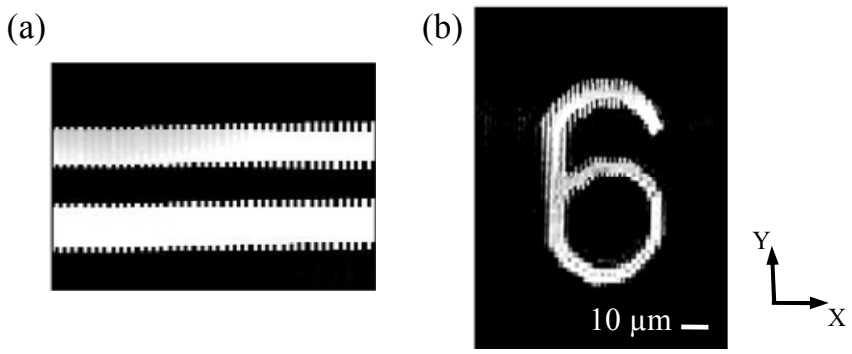

Figure 0.3 Confocal images of deposited chrome patterns on a glass substrate before correction (a) two parallel lines; each has a width of 8.8 µm, and (b) number six. The driving current frequency is 324 Hz in the fast scan axis.

We figured out that the motion artifact in the actuation of B2 and hence the optical fiber can be explained by the fact that C2 has an iron core that retains a static magnetic field when the current is removed. In our system, this residual DC magnetic field was about 0.2 mT, while the AC driving magnetic field is around 12 mT, measured using a Hall Effect Gaussmeter (SYPRIS Industrial Partner). Effects of this residual DC magnetic field in the coil can be modeled as a residual DC current, $i_{res.}$ in the following equation:

$$I = i_{res.} + i(t) = i_{res.} + i_0 \sin(\omega_i t) \tag{B.1}$$

where ω_i is frequency of driving current, t is time and i_0 is the current amplitude. By replacing this equation in the magnetic force equation (Eq. (2.8)), the magnetic force becomes:

$$F_{mag} = -\frac{\mu_0 A N^2}{2g^2}\left({i_{res.}}^2 + 2 i_{res.} i_0 \sin\omega_i t + \frac{{i_0}^2}{2}(1-\cos 2\omega_i t)\right) \tag{B.2}$$

It is observed that the magnetic force has two periodic components with different frequencies, one at the frequency of applied current ω_i and the other at $2\omega_i$. As a result,

while the force component with frequency $2\omega_i$ actuates the beam at its resonant frequency, a component of magnetic force at frequency ω_i equal to the driving current also acts on the beam and causes the observed disturbance and motion artifacts.

The described motion artifacts can be corrected using one of two methods. First, the effect of residual magnetic field can be eliminated by manually adding a DC bias to the driving current while measuring the actuation amplitudes of the beam, until peak amplitudes of actuations are equal. The bias signal has to be carefully selected so that the residual magnetic field of the coil is completely canceled out. It should be noted that, depending on the amplitude of the driving signal, the value of the required DC bias may slightly change every time the scanner is operated and the current is stopped.

Another way to correct this motion artifact is to match the frequency ω_i of driving current with resonant frequency of the beam (648 Hz). In this way, the component of magnetic force with frequency ω_i actuates the beam at its resonant frequency, while the second component of the force with frequency $2\omega_i$ (1296 Hz) is well above the resonant frequency and effectively negligible, resulting in an artifact-free motion of the beam. Figure 0.4 shows the driving current (Figure 0.4 (a)), measured actuation response of beam and its zoomed-in view (Figure 0.4 (b) and (c)), and FFT response of the beam (Figure 0.4 (d)) when a driving current of 648 Hz is applied. Figure 0.5 shows a distortion-free confocal images obtained by the raster fiber scanner.

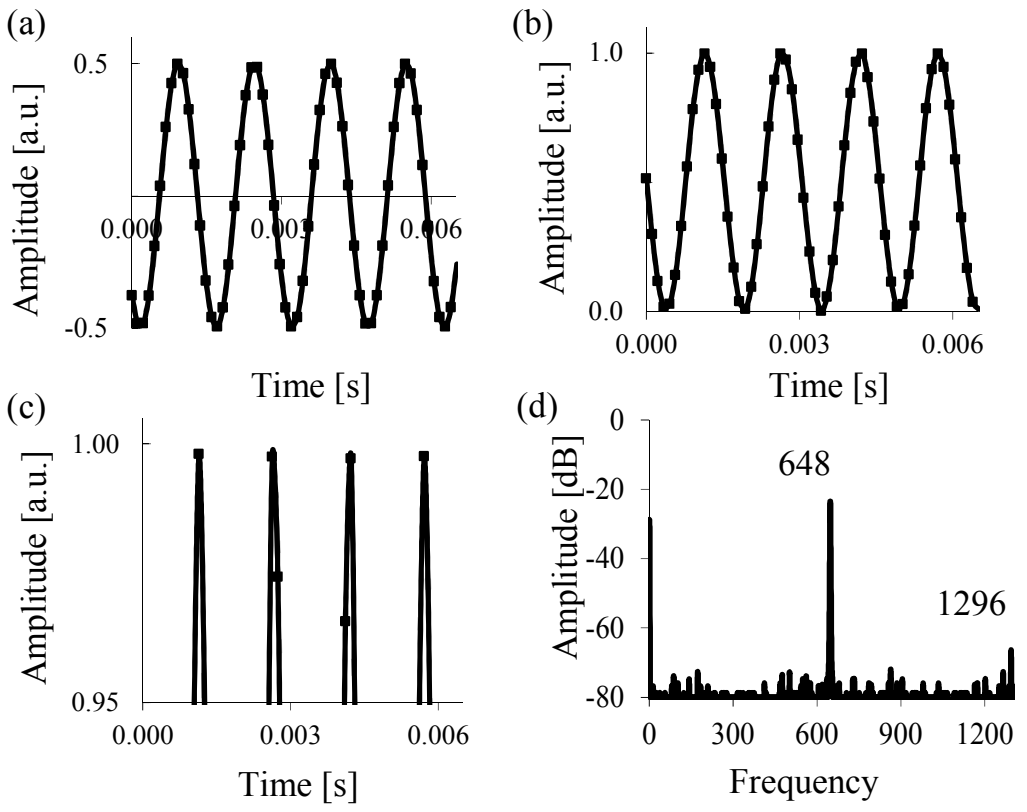

Figure 0.4 Experimental measurement of (a) driving signal with a DC bias applied to coil C2, (b) optical fiber displacement measured by LDV, (c) zoomed-in view of fiber displacement signal, and (d) FFT of response with driving current at 648 Hz frequency and no DC bias.

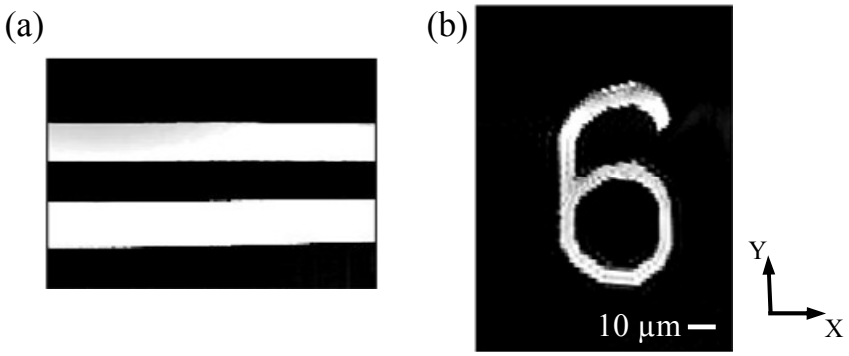

Figure 0.5 Confocal images of deposited chrome patterns on a glass substrate after correction (a) two parallel lines; each has width of 8.8 µm, and (b) number six. The driving current frequency is 648 Hz in the fast scan axis.

A.5 Conclusion

Imaging artifacts in the form of a wavy pattern were observed in a magnetic fiber actuator used for raster scanning of samples for confocal imaging. The image distortion was due to magnetic memory of the electromagnetic coil used to apply magnetic forces on the beam. The motion error can be corrected by operating the coil at a frequency matching the resonant frequency of the beam, or adding a DC bias current. Using this method, artifact-free confocal images of chrome patterns on a glass substrate were demonstrated. This method may also be used by other scanners with magnetic type actuators.